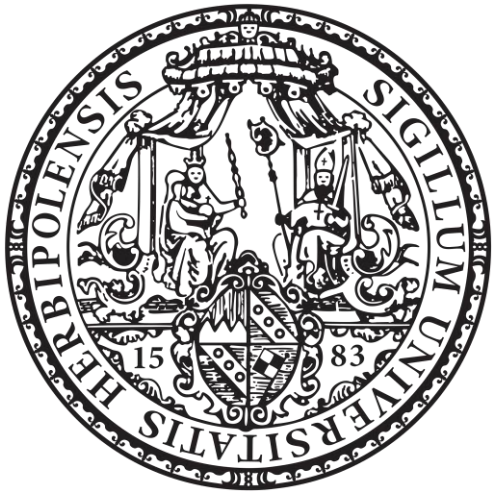

Induction, Imaging, Histo-morphological and Molecular Characterization of Myocarditis in the Rat to Explore Novel Diagnostic Strategies for the Detection of Myocardial Inflammation

Induktion, Bildgebung und, Histo-morphologische sowie Molekulare Charakterisierung der Myokarditis im Rattenmodell zur Entwicklung neuer diagnostischer Strategien zum Nachweis von Herzmuskelentzündungen

Doctoral thesis for a doctoral degree
at the Graduate School of Life Sciences,
Julius-Maximilians-Universität Würzburg,
Section Biomedicine

Submitted by

Priyadarshini Ambresh Panjwani

From

Bhandara, India

Würzburg, 2015

Submitted on: ……..……..

Office stamp

Members of the *Promotionskomitee*:

Chairperson: …Prof. Dr. Michael Sendtner…….....

Primary Supervisor: …Prof. Dr. Roland Jahns……

Supervisor (Second): …Prof. Dr. Martin Lohse…….....

Supervisor (Third): …Prof. Dr. Peter Jakob…….....

Date of Public Defence: ……..……..

Date of Receipt of Certificates: ……...

Affidavit

I hereby confirm that my thesis entitled ‘‘Induction, Imaging, Histo-morphological and Molecular Characterization of Myocarditis in Lewis Rats to Explore Novel Diagnostic Strategies for Detection of Myocardial Inflammation’’ is the result of my own work. I did not receive any help or support from commercial consultants. All sources and / or materials applied are listed and specified in the thesis.

Furthermore, I confirm that this thesis has not yet been submitted as part of another examination process neither in identical nor in similar form.

Würzburg, 21. August. 2015 **Signature**

Eidesstattliche Erklärung

Hiermit erkläre ich an Eides statt, die Dissertation ,,Induction, Imaging, Histo-morphological and Molecular Characterization of Myocarditis in Lewis Rats to Explore Novel Diagnostic Strategies for Detection of Myocardial Inflammation.‘‘ eigenständig, d.h. insbesondere selbständig und ohne Hilfe eines kommerziellen Promotionsberaters, angefertigt und keine anderen als die von mir angegebenen Quellen und Hilfsmittel verwendet zu haben.

Ich erkläre außerdem, dass die Dissertation weder in gleicher noch in ähnlicher Form bereits in einem anderen Prüfungsverfahren vorgelegen hat.

Würzburg, 21. August. 2015 **Unterschrift**

"The value we place on what we've been given
correlates to our depth of gratitude for it."
- Todd Stocker

Acknowledgement

Completing a PhD is truly a marathon event, and I would not have been able to complete this journey without the aid and support of countless people over the past four years. I must first express my gratitude towards my advisors, **Prof. Dr. Roland Jahns and Dr. Valérie Boivin-Jahns** for giving me an opportunity to pursue my doctoral studies in their laboratory. Their supervision, support, hard work, and scholarship have set an example I hope to match someday. I want to thank Prof. Martin Lohse for his unflagging encouragement and advices throughout my PhD thesis.

I am also indebted to Prof. Higuchi for his technical as well as scientific insights into my project. His guidance has served me well and I owe him my heartfelt appreciation.

Special thanks to Prof. Madeleine Cunningham, Prof. Karin Klingel and Prof. Asparouh Iliev for their advice and timely help. I am also very grateful to Prof. Peter Jakob and Dr. Karl-Heinz Hiller for allowing me to carry out my experiments in Department of Experimental Physics 5 (EP5) and also providing meaningful insights during project meetings. Dr. Xavier Helluy and Dr. Yuxiang Ye conducted all the MRI experiments in EP5 and I want to thank them for providing their technical and scientific input.

I am grateful to all the former and current members of AG Jahns, especially Angela, Yuxiang and Sonja for their assistance throughout my studies (and also for reading my manuscript). I also appreciate Cristina, Julia, Cristin and Katja (Angels of AG Jahns) for their technical support as well as creating a delightful atmosphere in our lab. Thank you all, it was a pleasure working with you!

I am thankful to Prof. Helga Stopper for allowing me to use the FACS machine in her laboratory. I appreciate Dr. Henning Hintzsche & Ezgi Eylül Bankoğlu for helping me with the technique as well as interpretation of the data.

I would like to especially thank Dr. Blum-Oehler, Dr. Kober & Dr. Köhne for their timely advice and guidance all through my PhD-program. I appreciate Kilian Keck for helping me

with ‘Zusammenfassung’, Jennifer Heilig & Amod Godbole for proof reading my thesis and providing me helpful feedback.

During my stay in Germany, I met many wonderful people who have influenced my personal and professional development. I am thankful to each and every one of you for your support and kindness. Of course, my friends and the ‘Panjwani Clan’ outside Germany also contributed equally in the process.

At last but not least, I am immensely thankful to my parents Mr. Ambresh Panjwani and Mrs. Madhuri Panjwani for having faith in my capabilities and supporting me during all the ups and downs. My siblings Prateek and Prerana are the best people in the whole world, they always managed to distract me during stressful times, which made everything easy to pass through. Whoever I am and whatever I will achieve in future is only and only because of love and trust of my family!

Summary

Fulminant myocarditis is rare but a potentially life-threatening disease. Acute or mild myocarditis following acute ischemia is generally associated with a profound activation of the host's immune system. On one hand this is mandatory to protect the host's heart by fighting the invading agents (i.e., bacteria, viruses or other microbial agents) and/or to induce healing and repair processes in the damaged myocardium. On other hand, uncontrolled activation of the immune system may result in the generation of auto-reactive (not always beneficial) immune cells.

Myocarditis or inflammatory cardiomyopathy is characterized by focal or diffuse infiltrates, myocyte necrosis and/or apoptosis and subsequent fibrotic replacement of the heart muscle. In humans, about 30% of the myocarditis-patients develop dilated cardiomyopathy. As the clinical picture of myocarditis is multifaceted, it is difficult to diagnose the disease. Therefore, the main goal of the present work was to test and further develop novel non-invasive methods for the detection of myocardial inflammation by employing both contrast enhanced MRI techniques as well as novel nuclear tracers that are suitable for *in vivo* PET/ SPECT imaging.

As a part of this thesis, a pre-clinical animal model was successfully established by immunizing female Lewis rats with whole-porcine cardiac myosin (CM). Induction of Experimental Autoimmune Myocarditis (EAM) is considered successful when anti-myosin antibody titers are increased more than 100-fold over control animals and pericardial effusion develops. In addition, cardiac tissues from EAM-rats versus controls were analyzed for the expression of various pro-inflammatory and fibrosis markers. To further exploit non-invasive MRI techniques for the detection of myocarditis, our EAM-rats were injected either with (1) ultra-small Paramagnetic iron oxide particles (USPIO's; Feraheme®), allowing for *in vivo* imaging , (2) micron sized paramagnetic iron oxide particles (MPIO) for *ex vivo* inflammatory cell-tracking by cMRI, or (3) with different radioactive nuclear tracers (^{67}gallium citrate, ^{68}gallium-labeled somatostatin analogue, and ^{68}gallium-labeled cyclic RGD-peptide) which in the present work have been employed for autoradiographic imaging, but in principle are also suitable for *in vivo* nuclear imaging (PET/SPECT). In order to compare imaging results with histology, consecutive heart sections were stained with hematoxylin & eosin (HE, for cell infiltrates) and Masson Goldner trichrome (MGT, for fibrosis); in addition, immuno-stainings were performed with anti-CD68 (macrophages), anti-SSRT2A (somatostatin receptor type 2A), anti-CD61 (β_3-integrins) and anti-CD31 (platelet endothelial cell adhesion molecule 1).

Sera from immunized rats strongly reacted with cardiac myosin. In immunized rats, echocardiography and subsequent MRI revealed huge amounts of pericardial effusion (days 18-21). Analysis of the kinetics of myocardial infiltrates revealed maximal macrophage invasion between days 14 and 28. Disappearance of macrophages resulted in replacement-fibrosis in formerly cell-infiltrated myocardial areas. This finding was confirmed by the time-dependent differential expression of corresponding cytokines in the myocardium. Immunized animals reacted either with an early or a late pattern of post-inflammation fibrosis. Areas with massive cellular infiltrates were easily detectible in autoradiograms showing a high focal uptake of ^{67}gallium-citrate and ^{68}gallium labeled somatostatin analogues (^{68}Ga DOTA-TATE). Myocardium with a loss of cardiomyocytes presented a high uptake of ^{68}gallium labeled cyclic RGD-peptide (^{68}Ga NOTA-RGD). MRI cell tracking experiments with Feraheme® as the contrast-agent were inconclusive; however, strikingly better results were obtained when MPIOs were used as a contrast-agent: histological findings correlated well with *in vivo* and *ex vivo* MPIO-enhanced MRI images.

Imaging of myocardial inflammatory processes including the kinetics of macrophage invasion after microbial or ischemic damage is still a major challenge in, both animal models and in human patients. By applying a broad panel of biochemical, histological, molecular and imaging methods, we show here that different patterns of reactivity may occur upon induction of myocarditis using one and the same rat strain. In particular, immunized Lewis rats may react either with an early or a late pattern of macrophage invasion and subsequent post-inflammation fibrosis. Imaging results achieved in the acute inflammatory phase of the myocarditis with MPIOs, ^{67}gallium citrate and ^{68}gallium linked to somatostatin will stimulate further development of contrast agents and radioactive-nuclear tracers for the non-invasive detection of acute myocarditis and in the near future perhaps even in human patients.

Zusammenfassung

Eine fulminant verlaufende Myokarditis ist eine seltene aber potentiell lebensbedrohliche Erkrankung. Akute oder chronische Myokarditis gehen generell mit einer starken Aktivierung des Immunsystems der Betroffenen einher. Zum einen ist dies notwendig, um das Herz durch Bekämpfung der Eindringlinge (z.B. Bakterien, Viren oder andere mikrobielle Erreger) zu schützen und/oder Heilungs- und Reparaturprozesse im geschädigten Myokard einzuleiten. Zum anderen kann eine unkontrollierte Aktivierung des Immunsystems aber auch zur Entstehung von (nicht immer vorteilhaften) auto-reaktiven Immunzellen führen.

Eine Myokarditis oder entzündliche Kardiomyopathie ist charakterisiert durch fokale oder diffuse Infiltrate, Nekrose und/oder Apoptose der Myozyten und einen fortschreitenden fibrotischen Ersatz des Herzmuskelgewebes. Beim Menschen entwickeln etwa 30% der Myokarditis-Patienten eine dilatative Kardiomyopathie. Da das klinische Bild der Myokarditis sehr vielfältig sein kann, ist die Diagnosestellung dieser Erkrankung schwierig. Deshalb war es das Kernziel dieser Arbeit, nicht-invasive Methoden zum Nachweis myokardialer Entzündungen zu testen, und dabei neue Bildgebungsverfahren unter Einsatz von neuen MRT-Kontrastmitteln sowie neuen nuklearen Tracern, die auch für PET/SPECT geeignet wären, zu entwickeln. Diese Verfahren wurden von uns zunächst an einem human-analogen Ratten-Modell evaluiert, mit dem Ziel später evtl. auch einmal beim Menschen eingesetzt werden zu können.

Für unser präklinisches Tiermodell wurden weibliche Lewis-Ratten mit kardialem Myosin aus Schweinen immunisiert. Die erfolgreiche Induktion einer „Experimentellen Autoimmunen Myokarditis (EAM)“ wurde durch einen signifikanten Anstieg der Anti-Myosin Antikörpertiter in immunisierten Tieren und die Ausbildung eines Perikardergusses (Echokardiographie) bestätigt. Zusätzlich wurde aus apikalem kardialem Gewebe RNA isoliert und die Expression verschiedener pro-inflammatorischer und pro-fibrotischer molekularer Marker untersucht. Um die Bildgebung mittels kontrast-verstärktem cMRT zu optimieren, wurden den Tieren entweder kleine Eisenoxid-Nanopartikel (Ultra small paramagnetic iron oxide particles, USPIO; Feraheme®), oder sog. „Micronsized paramagnetic iron oxide particles (MPIO)‘‘ für das Tracking inflammatorischer Zellen injiziert. Im daraufolgenden Schritt wurden radioaktive nukleare Tracer (^{67}Gallium-Citrat, ^{68}Gallium-markierte Somatostatin-Analoga und ^{68}Gallium-markierte zyklische RGD-Peptide) injiziert, um dann Autoradiogramme von Herzschnitten zu gewinnen.

Anschließend wurden die Ergebnisse der Bildgebungsmethoden mit denen der Histologie der jeweiligen Herzen verglichen. Dazu wurden sequentielle Herzschnitte mit Hematoxylin-Eosin (HE; für Zellinfiltrate) und Masson-Goldner-Trichrom (MG; für Fibrose) angefärbt. Darüber hinaus wurden immuno-histochemische Färbungen durchgeführt (anti-CD68: Makrophagen; anti-SSRT2A: Somatostatin Rezeptor Subtyp 2A; anti-CD61: β3-Integrine, und anti-CD31: endotheliales Zelladhäsions-Molekül 1).

Seren von immunisierten Ratten reagierten stark mit kardialem Myosin im ELISA und im Western Blot. In erfolgreich immunisierten Ratten zeigten Echokardiographie und darauffolgende MRTs große Mengen an Perikarderguss (Tag 18-21). Die Analyse der Kinetik der myokardialen Infiltration ergab eine maximale Makrophageninvasion zwischen Tag 14 und 28. Das Verschwinden von Makrophagen ging mit einem fibrotischen Gewebeersatz in den vorher betroffenen myokardialen Gebieten einher. Dieses Ergebnis wurde durch die zeitabhängig variierende Expression der korrespondierenden Zytokine im Myokard bestätigt. Immunisierte Tiere reagierten entweder mit einem **frühen** oder einem **späten** Muster der post-inflammatorischen Fibrose. Die histologischen Ergebnisse korrelierten relativ gut mit den in-vivo und ex-vivo MRT-Bildern, aber wesentlich besser mit Autoradiogrammen, bei denen eine hohe fokale Aufnahme von ^{67}Gallium Citrat und ^{68}Gallium-markierten Somatostatin-Analoga (^{68}Ga-DOTA TATE) in stark infiltrierten Myokardarealen nachgewiesen werden konnte. Myokard mit Verlust von Kardiomyozyten (Nekrose/Apoptose) zeigte eine hohe Aufnahme von ^{68}Gallium-markierten zyklischen RGD-Peptiden (^{68}Ga-NOTA RGD).

Die Bildgebung myokardialer Entzündungsprozesse einschließlich der Kinetik der Makrophagen-Invasion nach mikrobieller oder ischämischer Schädigung stellt noch immer eine große Herausforderung dar, sowohl im Tiermodell als auch beim Menschen.

Unter Einsatz einer breiten Palette biochemischer, histologischer, molekularer und bildgebender Methoden sowie unter Verwendung von ein- und demselben Rattenstamm konnten wir deutlich machten, dass im Verlaufe einer akuten Myokarditis verschiedene Reaktivitätsmuster auftreten können. Vor allem Lewis-Ratten mit (induzierter!) akuter Myokarditis reagierten entweder mit einem frühen oder einem späten Verlaufsmuster von Makrophagen-Invasion und post-inflammatorischer Fibrose-Entwicklung. Im Vergleich zum kontrast-verstärkten kardialen MRT waren die Ergebnisse in der akuten inflammatorischen Phase der Myokarditis mit ^{67}Gallium-Citrat und ^{68}Gallium- markierten Somatostatin-Analoga in Bezug auf die tatsächlichen/ histologischen Befunde wesentlich viel versprechender. Die Weiterentwicklung nuklearer Bildgebungs-Strategien zur nicht-invasiven Detektion akuter

inflammatorischer Prozesse am Herzen könnte in naher Zukunft möglicherweise sogar deren diagnostischen Einsatz bei Patienten möglich machen.

Abbreviations

Abbreviation	Defination
Abs	antibodies
AC	adenylyl cyclase
ACE	Angiotensin converting enzyme 1
ADP	adenosine diphosphate
ANP	atrial natriuretic peptide
BNP	B-type natriuretic peptide
cAMP	cyclic adenosine monophosphate
CAP	caprylic acid precipitation
CD68	cluster of differenciation 68
cDNA	complementary deoxyribonucleic acid
DCM	dilated cardiomyopathy
DMSO	dimethyl sulfoxide
DOTA TATE	DOTA-octreotate
DPBS	Dulbecco's phosphate buffered saline
EAM	experimental autoimmune myocarditis
ECG	electrocardiogram
ED	end diasystolic
EF	ejection fraction
ELISA	enzyme linked immunosorbent assay
ES	end systolic
FCS	fetal calf serum
FOV	field of vision
^{67}Ga	Gallium 67
^{68}Ga	Gallium 68
GPCR	G protein-coupled receptors
HC	heavy chain
HE	hematoxilin & eosin
HF	heart failure
i.p.	intra peritoneal
i.v.	intra venous
Ig	immunoglobulin
IL	interleukin
INF	interferon
ir	infra red
LC	light chain
LOX	lysil oxidase
LV	left ventricle
LVEF	left ventricular ejection fraction

MGT	masson goldner trichrome
MMP	matrix metalloproteinases
MPIO	miron-sized iron oxide
MRI	magnetic resonance imaging
Mϕ	Macrophage
NOTA RGD	NOTA- arginine-glycine-aspartic acid
OCT	optimum cutting tempreture
OD	optical density
OPN	osteopontin
PAGE	polyacrylamide gel electrophoresis
PCR	polymerase chain reaction
PFA	paraformaldehyde
PVDF	polyvinylidiene di fluoride
qPCR	quantitative polymerase chain reaction
RF	radiofrequency
RNA	ribonucleic acid
RT	room temperature
RT-PCR	reverse transcriptase- polymerase chain reaction
RV	right ventricle
s.c.	sub cutaneous
SDS	sodium dodecyl sulfate
SERCA	SR-calcium-ATPase
SPIO	super paramagnetic iron oxide
T	tesla
T2*W	T-2-star-weighted
TE	echo time
TEMED	tetramethylethelenediamine
TGF	tumor growth factor
TIMP	tissue inhibitor of metalloproteinases
TNFα	tumor necrosis factor alpha
TR	repetition time
Tris	tris(hydroxymethyl)aminomethane
USPIO	ultra small paramagnetic iron oxide
v/v	volume/volume
w/v	weight/volume
ΔCt	fold change in expression; delta-c-t

Contents

"The real voyage of discovery consists not in seeking
new landscapes, but in having new eyes."
— Marcel Proust

Introduction

Heart failure has become an increasingly prevalent disorder and is associated with considerable morbidity and mortality (1). While many pathophysiological mechanisms such as inherited cardiomyopathies, ischemic cardiomyopathy or hypertensive heart disease are easily recognized in clinical practice, the molecular mechanisms that determine the progression of heart failure or ventricular remodeling are largely unknown. Autoimmune responses and inflammation are involved in the pathogenesis of many cardiovascular diseases (2,3). There is compelling evidence that inflammatory mechanisms may contribute to progressive heart failure. Myocardial infiltration of lymphocytes and of mononuclear cells, increased expression of pro-inflammatory chemokines as well as cytokines and circulating auto-antibodies are frequently observed in myocarditis and dilated cardiomyopathy (4,5). In our work, we give an overview on the development of myocardial inflammation and furnish some clues as of why the diagnosis and treatment of myocarditis in the clinic can be difficult. Our human-analogous animal model of experimental myocarditis describes possible experimental approaches to improve diagnosis of acute cardiac inflammation. Finally, we checked the utility of (novel) molecular targets in order to improve the detection and follow-up of inflammatory lesions making use of our myocarditis model.

1.1. Definition of Myocarditis

Myocarditis is clinically defined as an inflammatory disorder of the heart muscle. In this condition heart muscle is invaded by immune cells majorly consisting of monocytes, macrophages, T-cells and B-cells. The cellular infiltrates cause swelling of the cardiac muscle leading to the inflamed appearance of cardiac tissue as compared to normal cardiac tissue (Scheme 1).

Epidemiological studies suggest that myocarditis is a major cause of sudden death in adults less than 40 years of age (6). Following myocarditis, one third of the patients affected develop cardiomyopathy (7). This is considered as a non-specific response to general or individual cardio-noxious triggers such as viral or bacterial infection, cardio-toxic agents, catecholamines, myocardial infarction or mechanical heart muscle damage.

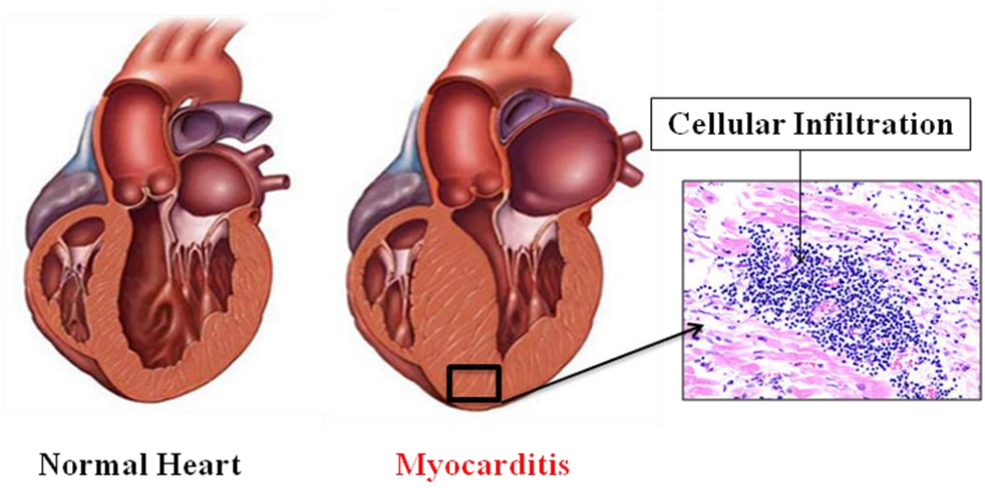

Scheme 1: Illustration depicting a normal and an inflamed heart. Cardiac inflammation is characterized by massive cellular infiltrates within the myocardium. *(Picture courtesy: texashealthcare.org)*

Myocardial processes initially triggered by infectious or non-infectious causes may evolve into a chronic inflammatory myocardial disorder. If the immune system does not eliminate an infectious agent at a very early stage due to insufficient immune activation (which is often genetically determined) a sort of chronic smoldering inflammation may develop, which might then lead to dilated cardiomyopathy (DCM) (8). However, smoldering myocarditis may remain asymptomatic for a long period of time. By contrast, successful elimination of the pathogen should resolve myocardial cellular infiltrates.

1.2. Cause and Mechanism involved in the progression of myocarditis

In Europe and North America, myocarditis most often results from infections with enteroviruses such as Coxsackievirus B3 or Adenoviruses (9); however, cardiotropic bacteria such as Borrelia and Chlamydia can also induce myocarditis and subsequent heart failure. In about one third of cases, smoldering inflammation and subsequent DCM may develop, which is the most common cause of heart failure in younger patients (10).

Notably, many of the affected patients with DCM develop heart-specific autoantibodies suggesting a role for autoimmunity in disease pathophysiology (11). Evidence for autoimmunity in post viral cardiomyopathy is also provided following the observation of an abnormal expression of HLA class II molecules on endothelial cells and from an association of dilated cardiomyopathy with HLA-DR4 (12). Further, our group has shown that the neutralization of antibodies activating the cardiac beta1-adrenergic receptor may prevent

cardiac dilatation and subsequent failure (13). In addition, post-inflammation immunosuppressive therapies may improve the cardiac function in some myocarditis patients, particularly in individuals without evidence for persistence of viral or bacterial genomes in endomyocardial biopsies (14). These observations suggest that post-infection autoimmunity might play an important role in heart failure development.

1.3. Diagnosis of Myocarditis

Despite the simplistic definition, myocarditis is a complex disease with many different pathogenetic mechanisms involved in the initiation and/or course of cardiac inflammation. The diagnosis and treatment of myocarditis is currently a major clinical challenge (15,16). Most of the clinical cases are associated with viral infection and an appropriate treatment depends on whether the disease is primarily infectious, immune-mediated, or both (17). While some of these mechanisms appear to be engaged in a chronological fashion, in the large majority of cases they overlap rendering an accurate diagnosis (and treatment) difficult.

Clinical diagnosis of suspected myocarditis is not always straight-forward; most patients with myocarditis initially have non-specific symptoms that are often categorized in the context of the preceding infection and not as being of cardiac origin. The broad spectrum of clinical manifestations makes the true incidence of myocarditis difficult to determine (18). Myocarditis can manifest similar to a myocardial infarction with sudden-onset angina pectoris, atrial or ventricular arrhythmias, and/or heart failure from systolic or diastolic dysfunction developing within 10-15 days (19). Myocardial inflammation induced by microbial agents is generally associated with a profound activation of the host's immune system. Differences in clinical and histological features between acute and chronic inflammation are thought to be associated with both the initial trigger and the underlying circumstances, that is, the genetically determined immunological background that defining the intensities and the duration of an immune-response. If the immune system does not eliminate the causative agent at a very early stage, chronic inflammation may develop leading to the progressive deterioration of cardiac function and, finally, severe HF in about 30% of the patients. By contrast, successful elimination of the pathogenic agent together with a rapid resolution of cellular infiltrates may result in full recovery of cardiac function in about another 30% of the patients.

Myocarditis has been detected in 1-9% of routine autopsies and in 9-12% of autopsies from patients with sudden cardiac death (20). In some cases fulminant inflammation may occur, including the formation of giant cells, eosinophilic infiltrates (21,22), or even large necrotic areas (23). In the European Study of the Epidemiology and Treatment of Inflammatory Heart Disease (ESETCID), 3055 patients with suspected myocarditis were screened: 72% presented with dyspnea, 32% had chest pain, and 18% had arrhythmias (24). Thus, cardiac involvement in infectious disease is often considered only when cardiac symptoms, such as palpitations, angina, and/or exertional dyspnea persist for a long period of time after the underlying infection has been resolved, or if they develop de novo in the course of the recovery (25). Diagnostic method(s) at this point in time includes:

i. Electrocardiogram (ECG): ECG-alterations compromise nonspecific ST-elevation, heart block and/or low voltage. However, the sensitivity and predictive power of the ECG for myocarditis is low.

ii. Laboratory chemical findings that are characteristic of acute myocarditis (including elevated cardiac enzymes that are typical for acute myocardial involvement) may be present or not. The same is true for Troponin T and I which indicate myocyte damage but are not specific for myocarditis.

iii. Echocardiography, CT and MRI may unravel impaired wall movement and reduced ejection fraction, but imaging results may be highly variable. When using MRI for the detection of myocardial edema a combination of T1-weighted and T2-weighted scans is recommended to increase sensitivity and specificity.

However, a definite diagnosis of myocarditis in humans can currently only be obtained by endomyocardial biopsy (26).

1.4. Endomyocardial Biopsy (EMB)

Endomyocardial biopsy (EMB) is an invasive diagnostic procedure that serves to diagnose the rejection status of the donor heart after cardiac transplantation but also serves to diagnose acute myocarditis (16). Usually, up to ten biopsies are taken from the right ventricle by fluoroscopic guidance. The safety of heart biopsies has improved since the 1960s, with vascular access through the right external or internal jugular vein, sampling of the right inter-ventricular septum, and designation of the heart borders by right heart ventriculography before biopsy(27). The EMB requires insertion of a preformed sheath in either the veins (RV)

or arteries (LV). Arterial sheaths must be maintained under constant pressurized infusion to avoid embolic events. Single-use bioptomes and sheaths allow access through the right and left jugular or sub-clavian veins, right and left femoral veins, and right and left femoral arteries. The right internal jugular vein is the most common per-cutaneous access site for right ventricular EMB in the USA (28). The femoral artery may be used as a per-cutaneous access site for a left ventricular biopsy. Monitoring includes observing the electrocardiographic rhythm, blood pressure and pulse-oximetry. Aspirin or other antiplatelet agents may be used in addition to heparin during left heart biopsy procedures to decrease the risk of systemic embolization (29). No comparative studies exist on which to base a recommendation for left versus right ventricular biopsy; however, left ventricular biopsy has been used in case series to define cardiomyopathic processes limited to the left ventricle.

The risks of EMB may be divided into those that are acute and those that are delayed. Immediate risks of a biopsy include perforation with the pericardial tamponade, ventricular or supraventricular arrhythmias, heart block, pneumothorax, puncture of central arteries, pulmonary embolization, nerve paresis, venous hematoma, damage to the tricuspid valve, and creation of arterial venous fistula within the heart (30). The risks of EMB are likely to vary with the experience of the operator, the clinical status of the patient, the access site, and possibly the bioptome. Delayed complications include access site bleeding, damage to the tricuspid valve, pericardial tamponade, and deep venous thrombosis (31).

Fowles and Mason reported an overall complication rate of 3-6 % in biopsies performed during transplantation and cardiomyopathies. Death associated with EMB results mostly from perforation and subsequent pericardial tamponade. Patients with increased right ventricular systolic pressures, bleeding diathesis, recent recipients of heparin or patients with right ventricular enlargement seem to be at higher risk (32). Moreover the invasive nature of this technique is immensely uncomfortable and usefulness is limited by sampling error.

Despite the invasive nature of EMB and the risks associated with it, it is still considered by many clinicians to be the gold standard for diagnosing myocarditis (33), although its diagnostic accuracy may suffer from sampling errors.

1.5. Classical (histopathological) diagnosis of myocarditis

In 1984, a panel of pathology experts met in Dallas (USA) to set forth certain criteria and guidelines to characterize the morphologic diagnosis of myocarditis by EMB after the

success of EMB in monitoring cardiac transplant patients for rejection had been established (34).

Dallas Criteria (1987): Myocarditis is present only if cellular inflammatory infiltrates are present in direct association with myocyte degeneration or necrosis not typical of ischemic necrosis. Borderline myocarditis requires less intense inflammatory infiltrates and no light microscopic evidence of myocyte destruction. These criteria are highly specific but have only a 10% to 22% sensitivity for myocarditis. This lack of precision of the Dallas criteria arise from sampling errors caused by distribution of the infiltrates within myocardium and a high inter-observer variability regarding interpretation (35). Chow *et al.* and Hauck *et al.* demonstrated by postmortem cardiac biopsies of patients who had died from fulminant myocarditis that, from a single endomyocardial biopsy, histological myocarditis could be ascertained in only 25% of the cases. With 18 biopsies myocarditis could be diagnosed in approximately two thirds of subjects by using 'The Dallas Criteria'(36). Currently, EMB is considered the gold standard for the diagnosis of myocarditis (16), but because of its invasive nature is often not performed. Due to risk of sampling errors (patchy distribution of inflammatory lesions) up to 17 EMBs are required to diagnose myocarditis with sufficiently high sensitivity (36). Nevertheless, the sensitivity for the histological detection of myocarditis by EMB is only in a range of 50-60%, unless combined with immuno-histo-chemistry and/or PCR for virus detection, which may fail in the advanced inflammatory phase (37). In addition, pilot studies using cMRI-guided EMB have shown that histologically confirmed infiltrates are mostly located in the lateral left ventricular wall rather than the septum which is routinely used for EMB (38).

Thus, the high risks and low sensitivity of EMB limit its current use in acute unexplained dilated cardiomyopathy (DCM) to a research tool or to exclude giant cell myocarditis (39). More and more experts have called for abandoning the use of the Dallas criteria. In chronic DCM, however, EMB remains the only way to confirm the presence of viral genomes and to guide treatment for persistent viral infection. Other pathological diagnostic criteria for myocarditis, including the expression of class I and II human lymphocyte antigens on cardiac myocytes, may indicate a subset of patients with chronic myocarditis (40).

1.6. Lewis rat model of Experimental Autoimmune Myocarditis (EAM)

The idea that autoimmunity may trigger the development of myocarditis and vice versa is supported by findings from experimental animal models (41). In addition, such

animal-models may serve for the pre-clinical testing of novel non-invasive detection modalities for myocardial inflammation. Experimental Autoimmune Myocarditis (EAM) is a model for inflammatory heart disease generated by immunization with cardiac myosin in susceptible rats. The EAM model can also be generated by using antigenic epitope(s) of cardiac myosin without using the whole protein (42,43).

Since the aim of our project was to develop autoimmune myocarditis in an animal model suitable for imaging purposes, the Lewis rat was our animal of choice. Immunization of Lewis rats with porcine cardiac myosin (CM) almost reproducibly induces severe myocarditis (42). Thus it has been employed as a model for many years since it combines the advantages of a reasonably sized heart, (compatible with the diagnostic appliances) and a relatively well characterized immunological and immuno-genetical background (44). Furthermore rats and, in particular the Lewis strain, are susceptible to a large variety of antigens that may induce development of myocarditis (45). The reason for this high susceptibility of the Lewis strain for autoimmune myocarditis (and autoimmunity in general) is unknown, but several possibilities have been proposed, including a low thymic presentation of numerous cardiac antigens, which would impede deletion of antigen-specific effector cells in the thymus.

In previous reports, Lewis rats immunized with cardiac myosin showed severe myocarditis characterized by pericardial effusion, cardiac enlargement, discoloration of the heart, and appearance of multinucleated giant cells in the lesions (46). In many reports it has been described that the clinical condition and pathology largely resembles human giant cell myocarditis (47). In the Lewis model, complement and anti-myosin antibody production together with a release of T- and B-cell mediators amplify the local immune response by the continuous recruitment of inflammatory cells from the peripheral blood, including granulocytes, lymphocytes, and monocytes (48). Hence EAM generated in the Lewis rat was considered a suitable model to investigate in detail the spatial and time-depended spread of myocardial inflammation by employing various methods comprising histology, immuno-histology, gene expression, and different imaging-modalities.

1.7. Cytokines involved in Myocarditis

Cytokines and Chemokines involved in cardiac Inflammation:

In humans, autoimmune myocarditis arises after ischemic, toxic or microbial damage to the heart muscle (49). Patients with a history of myocarditis or cardiomyopathy often show evidence of autoimmunity against cardiac tissue proteins (11,50). In Lewis rats, this condition can be mimicked by immunization with cardiac myosin together with complete Freund's adjuvant (CFA). As a result of the immune trigger, a number of specific cytokines and chemokines are released.

Cytokines are mainly, but not exclusively, secreted by antigen-presenting cells and lymphocytes. The local expression of certain cytokines regulates the inflammatory response dependent on antigen recognition, homing and has a major impact on migration and activation of distinct cell populations including endothelial cells, lymphocytes, and even resident cardiomyocytes (51).

Pro-Inflammatory cytokines expressed by inflamed cardiac tissue

Interleukin-6: This cytokine is known to play a very critical role in the development of systemic inflammation (52). It is involved in the process of antigen presentation, early activation of immune responses, and attenuation of viral replication in case of viral myocarditis (53).The precise pathological role of IL-6 is controversial as it can act as both a pro-inflammatory and an anti-inflammatory cytokine (54). With respect to myocarditis, several groups have suggested that an elevated level of IL-6 is necessary for the progression of autoimmune myocarditis to DCM (55). Other groups reported that high levels of IL-6 might be protective during the progression of the disease (56). However, when high levels of IL6 are accompanied by high levels of IL-1β, TNF- α, IFN-γ a progression of the disease is expected (57).

Interleukin-1 (IL 1): Interleukins from the IL1 family are characterized as both pro- and anti-inflammatory cytokines. In addition, administration of exogenous IL-1 has been shown to increase the pathogenetic potential of Coxsackievirus B3 infection in mice resulting in acute myocarditis (58). IL1 is produced by activated macrophages as a pro-protein, which is proteolytically processed to its active form by caspase 1 (CASP1/ICE) (59). It is an important mediator of the inflammatory response, and is involved in a variety of cellular activities, including cell proliferation, differentiation, and apoptosis. As reported by Erickson U *et al*,

IL- 1 triggering is required for efficient activation of dendritic cells, which in turn is a prerequisite for induction of auto-reactive CD4+ T cells and autoimmunity(60).

Interleukin-18: Interleukin-18 (IL-18) is previously known as interferon γ-inducing factor, a recently added member of the IL-1 family, and now recognized as an important regulator of innate and acquired immune responses (61). IL-18 is expressed at sites of chronic inflammation, in autoimmune diseases, in a variety of cancers, and in the context of numerous infectious diseases (62). In recent studies, consistent functional effects on the lymphoid system, that is stimulation of Th1-responses through IL-18, have emerged. Thus; IL-18 enhances T and NK cell maturation, cytokine production, and cellular cyto-toxicity. IL-18 also increases the expression of FasL on NK cells and as a consequence Fas-FasL-mediated cyto-toxicity. IL-18 not only acts through lymphocyte activation but also has direct effects on macrophages (63). IL-18 expression is in turn up-regulated in fibroblast-like synoviocytes by IL- 1β and TNF- α, suggesting the existence of positive feedback loops linking monokine predominance in inflammation with innate cytokine production and an activation of the Th1 pathway (64).

Tumor Necrosis Factor-Alpha: first evidence for a critical role of TNF- α came from the notion that patients suffering from chronic heart failure had elevated serum levels of this cytokine, whereas some cachectic patients did not (65). TNF-α has been reported to depress myocardial contractility, alter muscle membrane potential, lower blood pressure, and to be associated with the occurrence of pulmonary edema and acute myocardial infarction (66,67). TNF-α is a key regulator of immune cells. TNF, being an endogenous pyrogen, is able to induce fever, apoptotic cell death, sepsis (through IL1 & IL6 production), cachexia, inflammation, and is also able to inhibit tumor-genesis as well as viral replication (68). Dysregulation of TNF production has been reported to be involved in a variety of human diseases, including Alzheimer's disease, cancer, major depression, and inflammatory bowel disease (69). High levels of TNF-α are an indicator of systemic inflammation. It is produced mainly by activated macrophages (M1), although it can also be produced by other cell types, such as CD4+ lymphocytes and/or NK cells (70).

Interferon-Gamma (IFN-γ): In addition to having antiviral activity, IFN- γ has important immunoregulatory functions. It is a potent activator of macrophages, and its expression is associated with a number of inflammatory and autoimmune diseases (71). IFN-γ is produced predominantly by natural killer (NK) and natural killer T (NKT) cells as a part of the innate immune response, but also by CD4 (Th1) and CD8 (Cytotoxic T lymphocyte; CTL) effector T cells once antigen-specific immunity develops (72).

CD4+ T-cells can be characterized on the basis of secretion of interferon gamma. TH1 cells typically produce a higher amount of IFN-γ as compared to TH2 cells. TH2 cells prefer to secrete more IL4, whilst a higher level of interferon gamma is suggestive of the TH1 mediated adaptive immune response, where it is responsible for expansion and the auto-reactive properties of CD4+ T-cells (73). A pro inflammatory role of IFN- γ in myocarditis was underscored by the fact that mice lacking the SOCS-1 (suppression of cytokine signaling-1) gene develop spontaneous myocarditis and necrosis only in the presence of IFN-γ (74). However, in the context of autoimmune myocarditis, recent data have shown that IFN- γ is not required for disease development. Mice deficient in the ligand binding domain of the IFN-γ receptor are not only highly susceptible, but also develop a kind of chronic myocardial inflammation with high mortality (75). In animal (rodent) experiments performed by Rose and coworkers, cardiac myosin-immunized wild-type mice were treated with anti-IFN-γ antibodies. They observed enhanced disease scores three weeks after immunization (76). Suggesting that, IFN-γ is not only dispensable but may even offer protection against murine autoimmune myocarditis.

Interleukin 17 (IL17A): Numerous immune regulatory functions have been reported for the IL-17 family of cytokines, presumably due to their induction of many immune signaling molecules. The most notable role of IL17 is its involvement in inducing and mediating pro-inflammatory responses. IL17 is a cytokine that acts as a potent mediator in delayed-type reactions by increasing the production of chemokines in various tissues that recruit monocytes and neutrophils to the site of inflammation (77). IL17 as a family functions as a pro-inflammatory cytokine that responds to the invasion by extracellular pathogens and induces destruction of the pathogen's cellular matrix. IL17 is produced by T-helper cells and is induced by IL23 which results in destructive tissue damage in delayed-type immune reactions. Interleukin 17 acts synergistically with TNF-α and IL1. IL17 function is also essential to activate a subset of CD4+ T-Cells called T helper 17 (Th17) cells (78). Many recent studies suggest that the IL17 signaling complex may be clinically relevant for mitigating inflammatory the pathology of inflammation (79).

Interleukin-23 subunit alpha (IL 23α): This cytokine is predominantly produced by dendritic cells and macrophages. IL-23 importantly contributes to the inflammatory response against infections. It promotes up-regulation of the matrix metalloprotease MMP9, increases angiogenesis, and reduces CD8+ T-cell infiltration (80). In conjunction with IL-6 and TGF-β1, IL-23 stimulates naive CD4+ T cells to differentiate into a novel subset of cells called Th17 cells, which are distinct from the classical Th1 and Th2 cells. Th17 cells produce IL-17,

a pro-inflammatory cytokine that enhances T cell priming and stimulates the production of other pro-inflammatory molecules, such as IL-1, IL-6, TNF-alpha, NOS-2, and chemokines resulting in Inflammation. Thus IL23 alpha acts as a key regulator of the pro-inflammatory signaling cascade (81).

Transforming growth factor beta 1(TGFβ1): It is a multifunctional cytokine that controls proliferation and differentiation along with several other functions in diverse cell types. It acts synergistically with TGF-α to induce transformation of immune cells. It also acts as a negative autocrine growth factor (82). Dysregulation of TGFβ1 activation and signaling may result in apoptosis (83). A wide range of immune cells (or leukocytes) release TGF-β1. The main effect of TGF-β1 on macrophages and monocytes is predominantly suppressive. It inhibits the proliferation of these inflammatory cells and prevents them from producing reactive oxygen and nitrogen (super oxide and nitrous oxide) intermediates. However TGF-β1 also acts as a chemo-attractant, directing the immune response towards the pathogens during infection. Macrophages and monocytes respond to low levels of TGF-β1 in a chemotactic manner (84). TGF-β1 has been shown to increase expression of IL-1β and TNF-α, which in turn contribute to enhance inflammation.

Osteopontin (OPN): OPN is an extracellular structural protein produced by various immune cells upon exposure to pro-inflammatory cytokines. Studies suggest that classical mediators of inflammation such as TNF-α, IL-1β, angiotensin II, and TGF-β are responsible for the up-regulation of OPN in inflamed tissues (85). Macrophages challenged by hypoxia have also been shown to express high levels of OPN. Activated T-cells are promoted by IL-12 to differentiate towards the Th1 phenotype, producing cytokines including IL-12 and IFN-γ (86). OPN inhibits production of the Th2 cytokine IL-10, which leads to enhanced Th1 responses. OPN influences cell-mediated immunity and has Th1 cytokine functions. It also enhances antibody production and B-cell proliferation (87).

Pro-fibrotic cytokines expressed by inflamed cardiac tissue

Fibrosis is fundamental to pathological remodeling of the myocardium in the diseased heart. Excessive deposition of extra cellular matrix (ECM) in previously inflamed regions of cardiac tissue results in myocardial fibrosis which may result in DCM (88). Cardiac collagen, the major component of the ECM, is mainly composed of type I and III collagen (85% and 11% of total cardiac collagen, respectively). Differential increases in type I to type III collagen ratios have been reported in dilated cardiomyopathy. Interfibrillar crosslinking, which is mediated by Cu^{2+} dependent lysyl oxidases during fibrillogenesis, furnishes the necessary

tensile strength to the scarred tissue (89). However, excessive collagen deposition in tissue causes chamber stiffness, which is evident during diastole and occurs both in humans and experimental chronic heart failure models. Many experimental studies have also demonstrated an association between TGF-β activity and collagen 1 up-regulation, indicating that TGF-β impacts on collagen deposition in order to control inflammation**.**

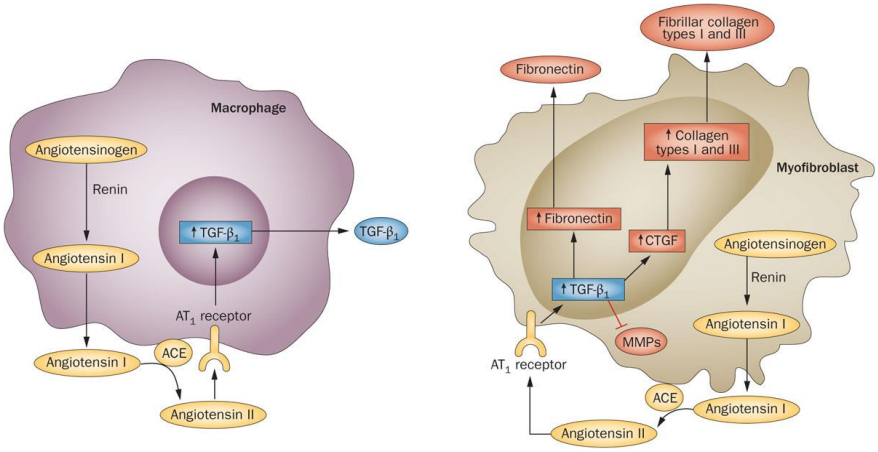

Scheme 2: Adapted from Weber et al, Nature reviews, 2013. The figure represents signaling between macrophage and myofibroblastic cells at the site of healing. Autocrine action of angiotensin II in the macrophages via binding to the AT_1 receptor- results in expression of TGF-β by these cells. TGF-β stimulates the myofibroblasts to initially produce fibronectin, which forms the basis of a provisional scaffold, and then produce type I and Type III collagen, which are assembled to form a scar and thus preserve the structural integrity of the myocardium.

Collagen Type I, Alpha 1: Enhancement of fibrosis content in the myocardium is a result of collagen type I synthesis, which significantly contributes to the development of heart failure in patients (90). Type I collagen in the heart is mainly synthesized by cardiac fibroblasts, and is subject to slow metabolism with a half-life of about 100 days (91). Type I collagen represents 90% of total collagen at the site of scarring. Inter-fibrillary cross linking, which is mediated by Cu2+ dependent lysyl oxidase during fibrillogenesis, leads to composite collagen fibers providing the necessary tensile strength to circumvent myocardial deformation and to protect sarcomeres from overstretching beyond lengths required for force generation and shortening. Collagen is degraded via specific collagenases (matrix metalloproteinase; MMP), which are activated by extracellular serine proteases. Tissue inhibitors of MMP (so called TIMP's) form a complex with MMP in the extracellular space, thereby inhibiting collagen degradation (92).

Collagen Type III, Alpha 1: After myocardial injury, the remodeling process is characterized by collagen fiber degradation, edematous inter-muscular spaces and increased formation of type III collagen (93). Fibrosis may occupy as much as 30% of the myocardium. The high

level of fibrosis significantly alters the mechanical performance of the myocardium: myocardial stiffness increases resulting in impaired diastolic filling and cardiac function (94,95). However, severe fibrosis is not seen in animal models of hypertension/LVH, suggesting that excess fibrosis is regulated by other factors besides left ventricular load. For instance, infra-renal aortic banding induces an important increase in blood pressure and LVH without fibrosis (96). LVH provoked by exercise training is not associated with severe fibrosis. Accordingly, a major role for Angiotensin II and also aldosterone in fibrosis and collagen I accumulation has been assumed (97).

1.8. Non Invasive Magnetic Resonance Imaging (MRI)

In the last few decades, non-invasive imaging methods have been developed that are able to overcome the shortcomings of histological methods at least to some extent, Magnetic Resonance Imaging (MRI) provides excellent soft tissue contrast with a high resolution. Due to multiple MRI strategies (e.g. pulse sequences) to enhance image contrast, several anatomical, physiological and also some metabolic parameters can be measured almost simultaneously and under physiological conditions (98). Endogenous tissue properties as well as exogenous agents can be utilized to enhance or modulate image contrast, as e.g. the tissue proton content, viscosity, perfusion, and particular chemical composition. Particularly, in neurobiological research, high-resolution MRI provides not only information on brain morphology but also on hemodynamic changes (blood flow and tissue perfusion), metabolic changes (MR spectroscopy), and even functional changes (functional MRI, fMRI) and neuronal connectivity (diffusion tensor imaging (DTI)) and manganese-enhanced MRI, MEMRI) (99).

MRI has developed into one of the most powerful imaging tools in radiology and biomedical sciences. Due to its high resolution, MRI is currently exploited for the visualization of single cells against a homogeneous background. The availability of targeted contrast agents might extend applications of MRI from the visualization of cell location to the characterization of molecular and cellular signaling pathways. MR methods can provide the information required for *in vivo* cell visualization: High resolution with sufficient high sensitivity and specificity (100).

Cellular imaging using iron oxides was first introduced for hepatic imaging. Following intravenous injection, cellular imaging of monocytes /macrophage activity has found further applications in several other disease models. In the brains of rats and mice with experimental autoimmune encephalomyelitis (EAE) macrophages are present in multiple inflammatory foci

around blood vessels with a disrupted blood–brain barrier (101). These foci can be visualized by MRI following intravenous injection of iron oxide. The magnetic compounds may either be phagocytized by circulating monocytes or leak through the disrupted blood–brain barrier and are subsequently phagocytosed by the resident brain microglia. In brain ischemia, following iron uptake macrophages first migrate into the outer margin of the lesion, and then move into the inner core of the lesion at later time points (102).

1.8.1. MRI contrast agents

Iron oxide-based contrast agents that have been used for cell labeling can be classified according to their size in (a) ultra-small superparamagnetic iron oxide particles (USPIO); (b) superparamagnetic iron oxide particles (SPIO), and (c) micron-sized paramagnetic iron oxide particles (MPIO). Many of the iron oxide particles used for cell labeling and tracking has magnetic momentum up to three orders of magnitude larger than those of clinically used contrast agents. However, the uptake of the different particles varies largely between different cell types (103).

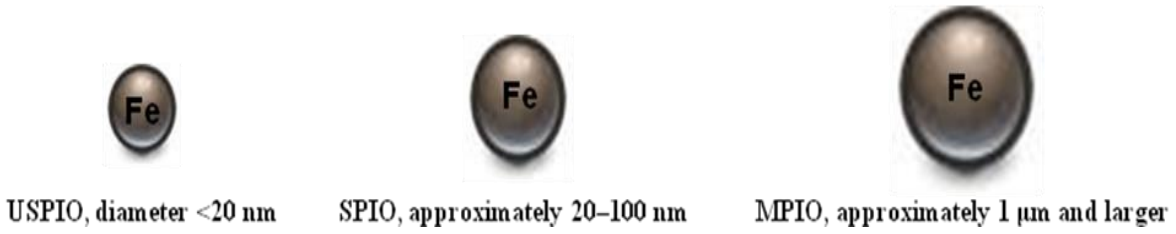

Scheme 6: Three different types of contrast agent are shown, classified according to the size; USPIO (Ultrasmall Superparamagnetic Iron Oxide, left), SPIO (Superparamagnetic Iron Oxide, middle), and MPIO (Micron sized Paramagnetic Iron Oxide, right). These particles have a predominant T2 effect (magnetic susceptibility) and produce a drop in signal namely in T2* weighted images.

1.8.2. USPIO (Feraheme®)

Ferumoxytol (Feraheme®, AMAG Pharmaceuticals Inc.) is a USPIO nanoparticle used for the intravenous treatment of iron deficiency in patients with impaired renal function (104). Ferumoxytol has a carboxydextran-coated iron oxide core and has a mean hydrodynamic diameter of 30 nm. It is an attractive MRI contrast agent because it appears to be safe even in patients with chronic kidney disease in advanced stages (105). Ferumoxytol accumulation occurs in areas of blood–brain barrier (BBB) dysfunction that is related to inflammation from

any cause. The iron present in Feraheme® is in the form of a superparamagnetic iron oxide that causes T1, T2, and T2* shortening on magnetic resonance imaging (MRI). Furthermore, the drug has a long intravascular half-life of 14–15 hours, meaning that once injected it can remain in the system for days to month (106).

1.8.3. SPIO

Superparamagnetic iron oxide particles (SPIO) consist of ferric ($Fe3^{+}$) and ferrous ($Fe2^{+}$) ions. These large magnetic signal/forces result in strong disruptions of the local magnetic field and yield artifacts. As a consequence, the signal is quenched and the presence of SPIOs is detected as a dark contrast (hypointensity). The large magnetic signal/force of SPIOs impacts on the magnetic field beyond the actual size of the particles. Therefore, even small numbers of SPIO-loaded cells are detectible by in vivo MRI (107).

1.8.4. MPIO

Micrometer-sized iron oxide particles (MPIOs, size range 0.76-1.63μm), are commercially available, efficiently endocytosed by a variety of cells, and can also be used for cellular imaging by MRI (108). For cellular imaging, the size of these particles prevents delivery to the specific target. For the imaging of inflammation, however, MPIO possess several positive attributes. First, MPIOs convey an amount of iron that is orders of magnitude greater than that conveyed previously by USPIOs used as MRI contrast agents. Second, the effects of MPIOs on the local magnetic field homogeneity and, therefore, on detectable contrast extend for a distance roughly 50 times the physical diameter of the MPIO. Third, the size of MPIOs infers that MPIOs compared to USPIOs are less susceptible to extravasation or nonspecific uptake by endothelial cells and, therefore, are considered to retain specificity for macrophages and monocytes (109). The MPIO particle used in our study was procured from Bangs Laboratory (for details see method section). The particle size is 0.9 μm with a dragon green florescent core (Ex 480, Em 520). The fluorescent core allows cell tracking using methods other than MRI and also facilitates the final confirmation by fluorescent microscopy.

1.9. Non-invasive imaging by Radioactive Nuclear Tracers

Clinical imaging techniques such as angiography, intra-vascular coronary ultrasound and angioscopy provide valuable information on various cardiac abnormalities. However, all these techniques are invasive. Since decades different non-invasive imaging strategies have emerged and were introduced in the routing diagnostics of cardiac inflammation, this includes multi-slice CT, magnetic resonance imaging and echocardiography. In addition, nuclear imaging offers the possibility to visualize inflammatory processes in a non-invasive manner by whole-body scanning enabling the determination, the localization and the quantification of inflammatory foci. Nuclear imaging modalities, such as single photon emission computed tomography (SPECT) and positron emission tomography (PET) allow quantitative image-analysis in a clinical setting. Thus, PET imaging of cardiac inflammation might be helpful to diagnose and monitor myocarditis in human patients (110). In order to detect inflammatory activity in vulnerable arteriosclerotic plaques, recently a pilot study using PET/CT has been conducted both in human and in rodent models. However, broad clinical applications of this method are currently hampered by the lack of target-nuclear tracers.

Peptides labeled with radioactive compounds have a fast clearance, rapid tissue penetration, and low antigenicity, and can therefore be produced easily and cost-efficiently (111). In the last few years, there has been a significant increase in the development of labeled peptides for diagnostic applications, especially due to simplified methods of purification. An inherent added advantage to this diagnostic approach is the potential therapeutic implication, since - if the diagnostic scan is positive - the peptides can be labeled with therapeutic radio-nuclides to perform peptide receptor radionuclide therapy (PRRT) (112). This kind of therapy is for example suitable for patients with widespread metastatic disease that is no more amenable to surgery, or for patients receiving focused radiation therapy.

Even though there are several nuclear tracers used for the imaging of inflammation by scintigraphy, none of them are specific for inflammation of cells (113). Targeted imaging of inflammatory processes is still a major challenge. Nuclear tracers employed are mostly injected intravenously and then accumulate in inflammatory lesions due to the locally changed physiological conditions. These changes comprise enhanced blood flow, enhanced vascular permeability, and accumulation of leukocytes/immune cells. Radiopharmaceuticals can be primarily divided into two classes: those nonspecifically accumulating in inflammatory lesions and those specifically accumulating within the inflammatory cells (114). Macrophages appear to represent the most useful targets in order to noninvasively detect acute inflammatory lesions (115).

In the following section, non-specific tracers like ^{67}Gallium-citrate, ^{99m}Technetium-Tetrofosmin (TF) and radio labeled peptides for the specific targeting of inflammatory cells are discussed further.

1.9.1. ^{67}Gallium-citrate and ^{99m}Technicium-TF

A.

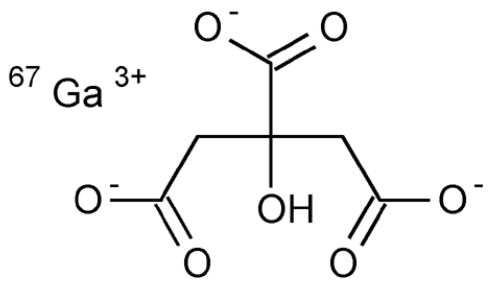

B.

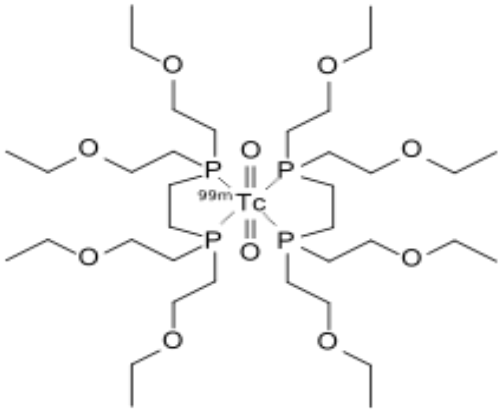

Chemical Structure 3: (A) 1,2,3-Propanetricarboxylic acid,2-hydroxy-,^{67}Ga(1:1)salt.(B) 1,2-bis[di-(2 ethoxyethyl)phosphino]ethane

Some feature characteristic for inflammation, such as increased blood flow and enhanced vascular permeability, can also be exploited for imaging of inflammation. Such features can be imaged by using ^{67}Gallium-citrate (116). A radioisotope routinely used to detect chronic inflammatory with a reported sensitivity of 90% (117). In the past, ^{67}Gallium imaging routinely used for cancer diagnosis and staging until it was replaced by fludeoxyglucose (FDG)-PET. ^{67}Gallium imaging is still employed for imaging of inflammation and/or chronic infections, and sometimes it still detects unsuspected tumors, as it is taken up by many kinds of cancer cells in amounts that exceed those of normal tissues (118). Thus, an increased uptake of ^{67}Gallium may indicate a new or old infection, an inflammatory lesion from any cause or a malignant tumor (119).

^{67}Ga acts as an iron analogue, labelling any protein that are able to bind iron. Initially ^{67}Ga binds to transferrin. The body generally handles $Ga3^{+}$ as ferric iron (Fe-III), and thus the free isotope is bound (and concentrates) in acute and chronically inflamed tissues but also areas exhibiting rapid cell division. Assuming regular laminar blood flow, the ^{67}Ga-transferrin complex diffuses through loose endothelial junctions of capillaries in the inflamed

tissue/organs and enters into the extracellular space, where it accumulates is then detected by scintigraphic techniques (120).

Another nonspecific tracer for imaging of inflammation is Technetium (^{99m}Tc) tetrofosmin (TF). ^{99m}Tc-TF is characterized by a rapid heart uptake and stable retention in the target organ (121). The washout is slow at the level of the heart but rapid from the blood, liver and lungs. The cellular uptake of ^{99m}Tc-TF is predominantly in the mitochondria, driven by its membrane potential (122).Intravenous ^{99m}Tc tetrofosmin injection generally serves to scintigraphically delineate regions of reversible myocardial ischemia in the presence or absence of infarcted myocardium, and also for the scintigraphic evaluation of left and/or right ventricular function under stress and rest conditions (123). The tracer is commercially available and FDA approved.

1.9.2. ^{68}Gallium DOTA-TATE

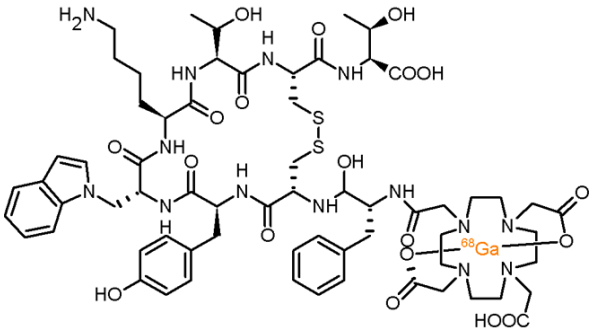

Chemical Structure 4: ^{68}Ga-[1, 4, 7, 10-tetraazacyclododecane-N, N′, N″, N‴-tetraacetic acid]-d-Phe1, Tyr3-octreotate

Labeled ^{68}Ga-[1,4,7,10-tetraazacyclododecane-N,N′,N″,N‴-tetraacetic acid]-d-Phe1,Tyr3 octreotate (DOTATATE) is clinically utilized for the visualization of somatostatin receptor (SSTR)-positive neuroendocrine tumors (NET) by (PET) (124,125) . The five different somatostatin receptor subtypes (SSTR1-5) that have been characterized are encoded by five genes, which are localized on separate chromosomes. SSTR1-5 exhibits high binding affinity to the natural ligands SS-14 and SS-28. Only receptor subtypes SSTR2 (which can be further divided into SSTR2A and SSTR2B), SSTR5 and to a lesser extent subtype SSTR3 have a

high affinity for commercially available synthetic analogues and even these differ in their affinity for the various analogues (126). ^{68}Ga-DOTATATE has selective affinity towards somatostatin receptor type2 (SSTR-2). According to Elliot et al, SSTR2A represents the dominant somatostatin receptor subtype specifically expressed by inflammatory cells. Thus it seems conceivable , that macrophages which represent the major fraction of early cellular infiltrates can also be detected by ^{68}Ga-DOTATATE PET imaging (127). So far, ^{68}Ga-DOTATATE has been used most widely in the clinical diagnostics of neuroendocrine tumors, but has also been shown to detect inflamed vessels due to uptake in macrophages or monocytes (128). An association with plaque calcification and risk factors of cardiovascular disease has already been demonstrated (129).

1.9.3. ^{68}Gallium NOTA-RGD

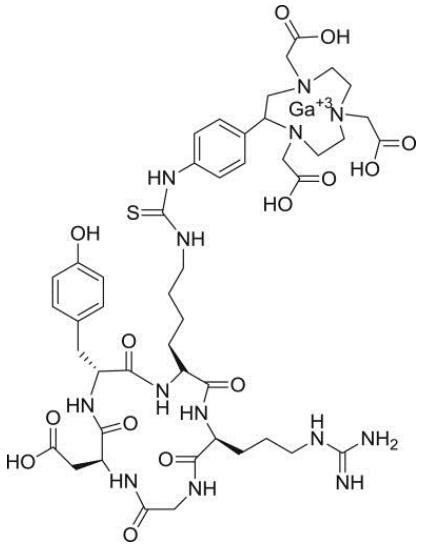

Scheme 5: Ga-[1, 4, 7, 10-tetraazacyclododecane-N, N′, N″, N‴-tetraacetic acid]-d-Phe1, Tyr3-octreotate

The ^{68}Gallium labelled cyclic peptide Arginine-Glycine-Aspartic acid (RGD) is a nuclear tracer utilized for the imaging of integrin receptors, e.g. after myocardial infarction (130). Integrins are a large group of adhesion molecules. The most extensively studied member of the integrin-family is integrin αvβ3. Integrin αvβ3 is a molecule which mediates the migration of endothelial cells through the basement membrane during blood vessel formation (131). It is significantly up-regulated in proliferating endothelial cells during angiogenesis, but not in inactive endothelial cells. Thus, integrin serves also as a molecular marker for tumor angiogenesis and the imaging of metastases. (132). In addition to cancer angiogenesis, integrin αvβ3 also plays an important role in wound healing, RA, psoriatic

plaque formation, and restenosis in blood vessels. It is one of the most successful imaging agents for PET and SPECT (133).

Imaging of αvβ3 integrin has the potential to serve equally as a new biomarker for disease activity in inflammatory processes (134). Integrin αvβ3 is upregulated in many inflammatory conditions, such as rheumatoid arthritis, cystic fibrosis, and endometriosis. So far, only preclinical imaging studies have been performed. The radio-labeled RGD peptide accumulates in chronically inflamed vessels in mice due to αvβ3-specific binding, and this process can be monitored noninvasively with PET (135). In addition to such induced inflammation-models, radio-labeled RGD peptides do also accumulate specifically in atherosclerotic plaques from genetically modified mice that spontaneously develop atherosclerotic lesions (136).

"A goal without a plan is just a wish."
-Antoine de Saint-Exupéry

Aim of work

Our aim was to establish a novel method for the detection of myocardial inflammation using contrast enhanced magnetic resonance imaging (MRI) as well as in vivo testing of novel nuclear tracers suitable for positron emission tomography (PET) and/or single photon emission computed tomography (SPECT).

Our strategy comprised of:

a) Immunization of Lewis rats with an emulsion of antigen (cardiac myosin) and adjuvant (complete freunds adjuvant (CFA)) along with heat-killed *B.Pertussis*.

b) Conventional echocardiography and cMRI to follow cardiac function, texture, and the development of pericardial effusion.

c) Step-by-step histological monitoring the course of immunization to determine the peak of inflammation and the time-course of fibrosis development

d) Administration of contrast enhancing agents (USPIO and MPIO) and nuclear tracers (^{67}Ga-citrate, ^{99} Technetium, ^{68}Ga-Linked to somatostatin-analogue and ^{68}Ga-linked to RGD peptide) at defined time points in the course of inflammation

e) Imaging hearts from immunized and control animals by *in vivo* MRI and *in vitro* microscopy and autoradiography.

f) Determination of expressed cytokines and receptors at the peak of inflammation

g) Histomorphological analysis and comparison of the results with MR-images and autoradiograms.

In this project, we attempted to induce, characterize and detect myocardial inflammation in the Lewis rat in order to gain deeper insight into molecular targets suitable for the detection of myocardial inflammation and establish novel strategies to diagnose myocarditis that later on may be translated to clinical practice.

"What we observe is not nature itself,
But nature exposed to our method of questioning. "
- Werner Heisenberg

Materials and Methods

3.1. Materials

Chemicals, primer sequences and instruments used in this study are given in Appendix A-C.

3.2. Induction of EAM in the Lewis rat

The animal-experiments were conducted under an institutional animal care and use committee approved protocol (52/08 Government of Unterfranken, Würzburg, DE). To induce EAM, in total n=106/133 female Lewis rats were s.c.-injected with 500µg of pig cardiac myosin (CM, Sigma Aldrich, DE) emulsified in complete Freund's adjuvant (CFA) (location of injections shown in figure) and boosted on d7, d14, and d28. On d0, d3, and d7 after immunization, the rats were i.p.-injected with $1x10^{10}$ heat killed Bordetella pertussis as described in (42). In total n=27 rats were control-injected with 0.9%NaCl in CFA. For histological analysis of inflammation and fibrosis n=20/106 immunized vs. n=5/27 control rats (sacrificed at d7, d14, d21, d28, and d35 post immunization) served to monitor the acute inflammatory phase; n=24/106 immunized vs. n=6/27 control rats served to monitor the early (d42, d45, d75, and d100 post immunization) and the late chronic post-inflammatory phase (d155 and d250 [e.g., ~5 and 8.5 months] post immunization). N= 39 or 13/106 EAM-rats (vs. 10 or 3/27 control-rats) were subjected to either ferumoxytol enhanced cMRI (d17-d29 post immunization) or to radionuclide imaging (d21 post immunization). N=10/106 EAM-rats and 3/27 control rats were subjected to MPIO enhanced cMRI (d17-d29 post immunization).

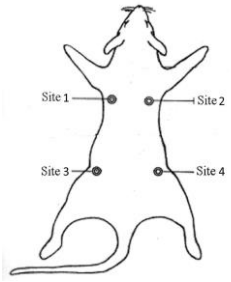

Scheme 7: Schemes depicting location of subcutaneous injections

3.3. Monitoring of the immune response

3.3.1. Enzyme-linked immunosorbent assay

Development of anti-myosin antibodies (abs) was followed by ELISA in all our immunised and control animals. 3 µg/ml of porcine cardiac myosin (Sigma, Steinheim, DE) were coated onto 96-well micro-titer plates at a final concentration of 50 µl /well in 0.1 M carbonate-bicarbonate coating buffer (pH 9.6) followed by an overnight incubation at 4 °C. Plates were washed three times with PBS containing 0.05 % Tween-20, then blocked with 3 % milk in PBS Tween-20 for 1 h at 37 °C, and washed with PBS Tween-20. Diluted rat serum samples (50 µl, 1/1000 dilution) in PBS with 3 % milk were added to the wells in duplicates and incubated overnight at 4 °C. Plates were washed with PBS Tween-20, and (50 µl vol, 1/7000 dilution) of biotin conjugated affinity pure $F(ab)_2$ fragment goat anti-rat IgG whole molecule (Dianova GMBH, Hamburg, DE) was added and incubated at 37 °C for 1h. Plates were washed and (50 µl, 1/4000 dilution) peroxidase conjugated streptavidin (Dianova GMBH, Hamburg, DE) was added. Plates were washed and 50 µl of ortho-pheno-diamine (Sigma, Steinheim, DE) in 0.1 M diethanolamine buffer (pH 9.8) were added. After 30 min the reaction was stopped using 3 M sulfuric acid; optical density (OD) was measured at 490 nm in an ELISA plate reader (Spectramax, Molecular Devices Corporation, Sunnyvale, USA). Sera from non-immunized animals served as a control, and rat IgG whole molecules served as internal standard for quantification (137).

3.3.2. Caprylic acid precipitation (CAP)

To isolate the IgG fraction of the sera, stripes of 14000 molecular weight cut off dialysis hose (Visking by carl Roth, Karlsruhe, DE) were pre-boiled in 500ml dialysis hose buffer for 10 min, rinsed three times with PBS buffer and then stored in PBS at 4^0 C for further use. Sodium acetate buffer was freshly prepared and kept at RT before use. Serum was thawed and kept on ice until further use. One volume of serum was added to two volumes of sodium acetate buffer while stirring constantly. 7.5% caprylic acid was added to the serum. After stirring for 30 min at RT the solution turns cloudy as components precipitate. This suspension was centrifuged at 5000 g for 15 min at 4^0C). If suspension remained cloudy then centrifugation step was repeated. The cleared supernatant was carefully pipetted into a dialysis hose, clamped at both ends and dialyzed against 1000-fold volume of pre-cooled PBS buffer for 12-16 hours at 4^0 C. After dialysis the samples were stored in non-binding reaction tubes until further use.

3.3.3. Western blot analysis

Immunized animals were sacrificed by cervical dislocation after peritoneal anesthesia. Rat hearts were harvested and immediately frozen in liquid nitrogen. Heart lysates were obtained by homogenization in lysis buffer (0.32 M sucrose, 20mM Tris-HCl, pH 7.4, 10mM MgCl2, 1g/ml aprotinin, 1 g/ml leupeptin, 0.1mM benzamidin, 0.2mM PMSF, and 1mM EDTA) in an ice cold condition, using Tissuelyser II (Qiagen, Hilden, DE). The lysates were kept on ice for 15 min and centrifuged at 15,000 *g* for 20 min at 4°C. Protein concentration in the re-suspended pellet was determined from a standard curve of BSA. Cardiac tissue lysates were subjected to sodium dodecyl sulfate-polyacrylamide gel electrophoresis (SDS-PAGE), and proteins were transferred onto polyvinylidene difluoride (PVDF) membranes (Immobilon-P; Millipore, DE). To analyse the specificity of the immune response, the blots were probed with caprylic acid precipitated serum from immunized animals (1:1,000) followed by horseradish peroxidase conjugated anti-rat immunoglobulin G (IgG; 1:10,000) (Jackson Immunoresearch, Dianova, DE). For analysis the probed proteins were visualized by enhanced chemiluminescence (Amersham Biosciences, Freiburg, DE).

3.4. Visualization of pericardial effusion

3.4.1. Echocardiography

Echocardiography was performed on days 0, 7, 14, and 21 in all immunized EAM-rats and in non-immunized control rats under light anesthesia (10 mg of ketamine/0.2 mg of xylazine). Echocardiograms were obtained by a commercially available echocardiography system (Visual sonics, Vevo 700, California, USA) equipped with a 17.5-MHz phased array transducer (Visual sonics, RMV 716-013) (138). M-mode tracings were recorded in the parasternal long and short-axis views through the aortic valve at the base of the aortic leaflets and through the anterior and posterior LV wall at the level of the papillary muscles. Wall thickness and LV internal dimensions were measured directly on the screen (online) according to the guidelines of the American Society of Echocardiography (139).

3.4.2. Cardiac MRI (*In vivo*)

N= 49/106 EAM-rats (vs. 13/27 control-rats) were subjected to either ferumoxytol enhanced cMRI or MPIO enhanced cMRI (d17-d29 post immunization). Imaging was performed with a 7 Tesla MRI-system (BioSpec 70/30 US; Bruker, Ettlingen, DE). Prospectively triggered cine-imaging and multiple gradient echo-measurements were acquired aided by a pressure-

sensitive balloon measuring thoracic motion during breathing and heart beats; the trigger-signal was post-processed with an amplification unit (Rapid Biomedical, Rimpar, DE). For in vivo MR-images, the animals were anesthetized with 1.5% isoflurane in pure oxygen and placed on a MRI-compatible 37°C heating pad. A quadrate birdcage RF resonator (Bruker; inner diameter 72mm) was used for signal transmission and reception. Cine scout images were taken for slice orientation (140).

3.5. Characterization of cellular infiltrates

3.5.1. Histology and stainings

N=20/106 immunized vs. n=5/27 control rats (sacrificed at d7, d14, d21, d28, and d35 post immunization) served to monitor the acute inflammatory phase; n=24/106 immunized vs. n=6/27 control rats served to monitor the early (d42, d45, d75, and d100 post immunization) and the late chronic post-inflammatory phase (d155 and d250 [e.g., ~5 and 8.5 months] post immunization) respectively. Cardiac tissue from EAM-animals and control animals was analyzed for the degree of inflammation on d21. After the imaging studies, selected animals were sacrificed and the respective hearts were extracted. The upper one third of the ventricles was embedded in OCT compound tissue medium (Sakura Fine technical co, Ltd, Tokyo, JP), snap frozen, and stored at -80 ^{o} C. Tissues were transversely cut into 3 µm-thick sections using a cryostat (Leica CM3050 S, Leica Biosystems, DE). Sections were fixed with 4 % PFA and subjected to haematoxylin and eosin (HE) or Masson Goldner trichrome (MGT) staining. The extent of inflammatory cell infiltration and of myocardial necrosis was derived from HE stainings. The degree of fibrosis was assessed from MGT stainings. In order to detect iron-oxides deposits *ex vivo* the respective tissues/blood smears were subjected to Pearl's Prussian blue staining. Both parameters (inflammation and fibrosis) were semi-quantitatively assessed by computer-aided image analysis of HE (red)- and MGT (green)-stained mid-ventricular 3µm-sections respectively.

3.5.2. Immunofluorescence

For Immunofluorescent Microscopy (IFM), frozen tissue samples were cut into 5 µm sections with a cryotome (LeicaCM 3050 S, Biberach, DE). The sections were fixed with 4 % PFA (10 min) and blocked with 2 % bovine serum albumin (BSA), 2% normal goat serum (NGS) and 0.1 % Tween-20. Sections were then incubated overnight at 4 ^{o} C with either mouse anti-rat CD68 (ABD Serotec, Oxford, UK), rabbit anti-rat somatostatin receptor type 2 (SSTRA 2) (Alomone Labs, ISR), rabbit anti-rat β3 integrin (CD31, BD Pharmingen, USA)

or mouse anti-rat CD31 (PEKAM, BD Pharmingen, USA) antibodies. Goat-anti-mouse Dylight 549 and goat-anti-rabbit CY2 (Jackson Laboratories, USA) were used as secondary antibodies. Incubations with secondary antibodies were carried out at room temperature for 30 min. Mowiol (2.4 g of Mowiol 4-88, 6 g of glycerol, 0.2 M Tris-Cl (pH 8.5)) was used as a mounting medium. The slides were dried for 12 h at 4^{o} C before IFM.

3.5.3. Cardiac gene expression

Apical cardiac segments were homogenized in RNAlater (Qiagen Inc., Chatsworth, USA). Real-time (RT) PCR was performed cardiac tissues to assess the expression of selected (pro)-inflammatory, (pro)-fibrotic and/or fibrotic markers 21 days after successful EAM-induction. Pro-inflammatory markers comprised tumor necrosis factor alpha (TNFα), interferon gamma (IFNγ), interleukin 23 a(IL23a), tumor growth factor beta1 (TGF β1), interleukin 1 beta (IL1β), interleukin (IL6), interleukin 17A(IL17A), and osteopontin (OPN); (pro-)fibrotic markers comprised : matrix metalloprotease 14 (MMP14), collagen type 1 α1, collagen type 3 α1, matrix metalloprotease 9 (MMP9) and lysyl oxidase (LOX). Endogenous glyceraldehyde-phosphate-dehydrogenase (GAPDH) served as internal reference. Total RNA was extracted from the myocardium using an RNeasy kit (Qiagen, Inc., Chatsworth, CA). According to the manufacturer's instructions mRNA was reverse transcribed in cDNA using a High Capacity cDNA Archive Kit (Applied Biosystems, Foster City, USA) and stored at -20 ^{0} C. Random hexamers were used as primers for the RT reaction. The cycling parameters were as follows: 2 min at 94 °C, 38 times (20 sec at 94 °C , 20 sec at 59 °C , 40 sec at 65 °C) and 5 min at 95 °C. Reactions were analyzed in triplicate and the relative expression levels were calculated according to the standard curve method. Expression data was normalized to GAPDH. The logarithm of the RNA concentration was calculated from standard curves using the delta Ct method. Expression of the markers selected was determined as the ratio of RNA target/RNA GAPDH.

3.6. Visualization of cellular infiltrates by MRI cell tracking

3.6.1. MRI cell tracking with USPIO's (Feraheme®)

N= 39/106 EAM-rats (vs. 13/27 control-rats) were subjected to ferumoxytol-enhanced cMRI (d17-d29 post immunization). For the detection of super-paramagnetic ferumoxytol, T2*-weighted (T2*w) axial images were obtained 48, 96, 120, 168, or 312h after the injection of

15 or 20mg/kg BW Feraheme® (AMAG Pharmaceuticals, Inc., Lexington, MA, USA) (corresponding to d17, 19, 20, 23 or 29 after EAM-induction) using a single or multiple slice/multiple spoiled gradient-echo (MGE) sequence (with parameters set at: FOV= 4x4 cm, matrix size= 256×256, slice thickness= 1.06 mm, number of slices= 3 in multi-slice mode). Single-slice mode MGE was carried out to improve blood/tissue contrast at 1-3 selected positions (with TR adjusted to heart rate [~170 ms]; TE= [2.5, 6.3, 10.0, 13.8, 17.5, 21.2, 24.9, 28.7ms], flip angle 28-45°, number of averages 8-12, total scan time ~11min per MGE-experiment).

3.6.2. MRI cell tracking with MPIO

3.6.2.1. In Vivo labeling of cellular infiltrates and MRI

N= 10/106 EAM-rats (vs. 3/27 control-rats) were subjected to MPIO-enhanced cMRI (d17-d29 post immunization). The MPIO particles (0.9µm magnetic microspheres, Bangs Laboratories, Fishers, IN, catalog No: ME03F) were prepared by washing and resuspension in PBS at 5 mg/ml. Animals were injected with MPIO (5 mg/kg body weight) 24 h before the scans. For MRI, rats were monitored as described above. End-diastolic and end-systolic myocardial volumes were derived from steady-state free precision ion gradient-echo cine images of the short-axis of the left and right ventricle respectively. Cine MRI parameters were as follows: FOV 40 x 40 mm2, acquisition matrix 50 x 40, slice thickness 1 mm, TR= 55 ms, TE= 8 ms, bandwidth per pixel= 80 Hz, k-space lines per segment = 1, breath-hold duration 2 sec/slice. Short-axis cine images (4–6 slices) were acquired compromising 2/3 of the ventricle, omitting the base and apex. For the monitoring of injected MPIOs, multi-slice ECG- and respiratory-gated T^*_2 –weighted gradient–echo images were acquired using the following parameters: FOV= 3-4 cm, TR= 55, TE= 7 ms, respiration cycle (~ 1 sec), slice thickness = 15 mm, in-plane resolution = 156 µm.

3.6.2.2. *Ex Vivo* MRI (MR-Microscopy)

After in vivo MRI, the rats were euthanized. The hearts were harvested, overnight fixed in 4% paraformaldehyde, and then stored in PBS. The fixed hearts were then imaged ex vivo by using a 17T/88mm system with a Micro 2.5 gradient insert (BioSpec 70/30 US; Bruker, Ettlingen, DE). High resolution three dimensional images were acquired using the following parameters: TR= 500 ms, TE= 8 ms and isotropic resolution = 50 µm.

3.6.2.3. Flow Cytometry

After MPIO-enhanced cMRI parallel to the excision of the hearts from all n= 10/106 EAM-rats (vs. 3/27 control-rats) white blood cells were harvested from blood, spleen and the peritoneal cavity and contained macrophages were enriched by plating them overnight on cell culture dishes. After 24h the cells were trypsinized and washed with PBS. Anti-CD68 (ABD Serotec, DE) was used as primary and anti-rat Dylight 549 (Jackson Laboratories, USA) as secondary antibody for the immunostaining of macrophages. MPIO particles already possess a dragon green fluorophore which can be detected by flow cytometry using FL1-H filter. After washing twice, cells were resuspended in 0.5 ml FACS medium. Flow cytometry was performed at Institute of Toxicology, University of Wuerzburg, using FACScalibur (Becton Dickinson, MA, USA). Acquired data was processed using CellQuest (Becton Dickinson, USA) software.

3.7. Visualization of cellular infiltrates by nuclear tracers.

Ex-vivo imaging with multiple radionuclide tracers study was conducted on d21 post immunization with ^{99m}Tc--tetrofosmin (electric potential of mitochondria), ^{67}Ga-citrate (transferrin/lactoferrin), ^{68}Ga DOTA-TATE (somatostatin receptors) and ^{68}Ga-NOTARGD ($\alpha_v\beta_3$ integrin receptors). 37MBq of ^{67}Ga-citrate, ^{68}Ga DOTA-TATE /^{68}Ga NOTA-RGD were injected intravenously in immunized and control animals (n=4/106 immunized; n=1/27 0.9%NaCl control). 45 min after the administration of the respective tracers the hearts were harvested, frozen, embedded in cryo-protectant, cut into 20 µm short-axis sections and exposed on a phosphor imaging plate for 24 hours. After exposure, photostimulated luminescence pixels (pixel size 50 x 50 µm) of the imaging plate were detected to visualize tracer distribution using a digital autoradiography imaging system (CR 35 Bio, Raytest, Straubenhardt, GR). Finally, results of the histological and immunohistological analyses were compared with the autoradiographs.

"Science progresses best when observations
force us to alter our preconceptions"
- Vera Rubin

Results

4.1. Induction of EAM in the Lewis rat.

Successfully immunized female rats (6-8 weeks old) rapidly developed both high titers of anti-cardiac myosin-abs and acute myocardial inflammation, whereas 0.9% NaCl-injected control rats did neither develop anti-myosin-abs nor myocardial inflammation (**Fig. 1A**). Antigen-boosts at d7, d14, and d28 lead to a further increase in antibody-titers (~40 and ~300 µg/ml, respectively; **Fig. 1A**) up to a maximum of ~9200 µg/ml and d57 after immunization (**Fig. 1B**). In the chronic phase anti-myosin ab-titers slowly decreased and remained almost stable at ~1000-2000µg/ml between d200-d250 (e.g., 6.5-8.5 months) *post* immunizations (**Fig. 1B**). Western blotting with mouse heart lysates revealed that the generated anti-myosin-abs recognized both the heavy (MW 200kDa) and the light chains of cardiac myosin (monomers: MW 15kDa; dimers: MW 34kDa; **Fig. 1C**).

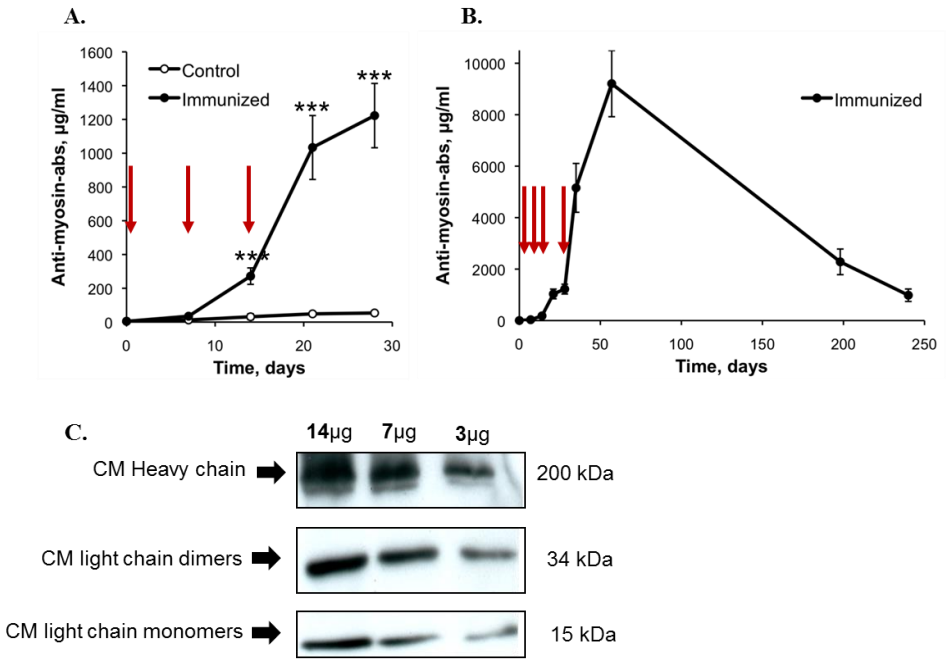

Figure 1: Titer-course of antibodies directed against cardiac myosin
(A) Anti-cardiac myosin antibody-titers determined in the early (0, 7, 14, 21, and 28d) and **(B)** late phase (35, 57, 200, and 250d) after EAM-induction. Error bars indicate mean ab-titers ± s.e.m. of n=52 selected immunized (black circles) or n=20 control rats (white circles). Arrows indicate antigen-boosts; ***p<0.001.
(C) Western blots with mouse cardiac tissue homogenates (3, 7, and 14 µg/lane) to check the specificity of IgG-fractions prepared from the sera of immunized rats (1:1000).

4.2. *In Vivo* screening for indirect markers of cardiac inflammation.

The cardiac phenotypes induced by immunization were surveyed by different *in vivo* imaging modalities. On d14 after myosin-injection the large majority of immunized rats developed pericardial effusion (PE) as demonstrated by echocardiography (**Figs. 2A and B**). Within the following days, PE even progressed. On d19 the same animals underwent cMRI for a more detailed analysis of myocardial function and texture. Occurrence of significant PE was confirmed by cMRI (**Fig. 2C**) and was consistently observed in all successfully immunized rats (peaking at d20-d22 (**Fig. 2E**)), whereas control animals did not develop PE (**Figs. 2D and F**).

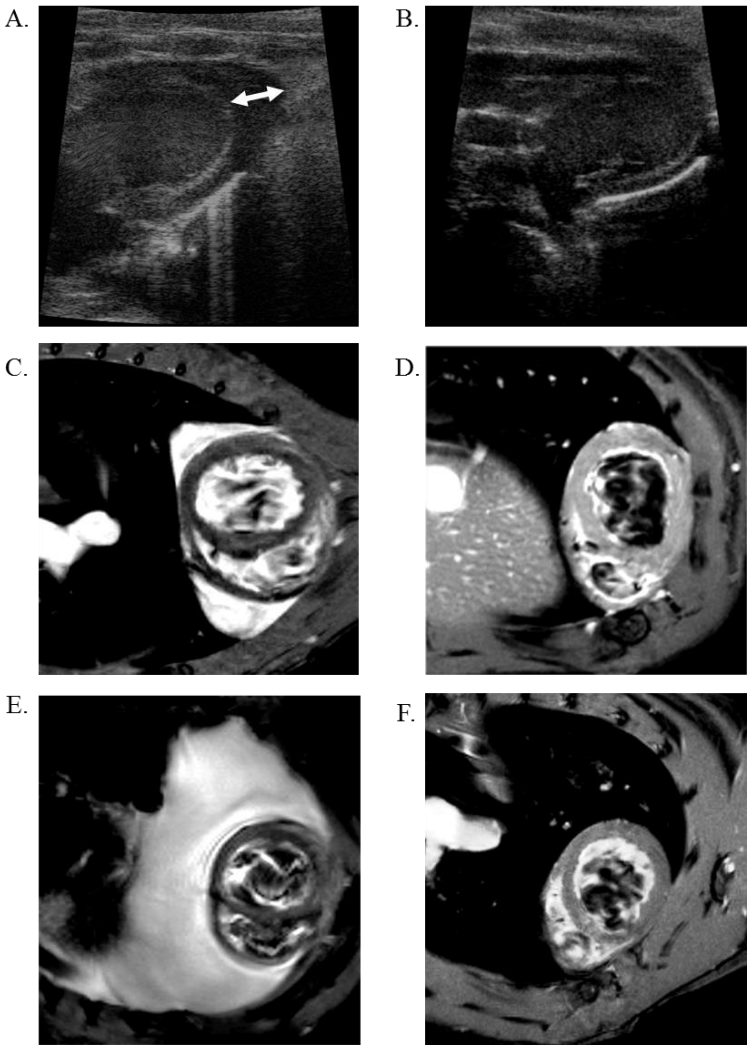

Figure 2: Visualization of pericardial effusion
A and **B**: Detection of pericardial effusion (PE) by echocardiography (d14 after immunization); long axis view representative for (A) an immunized rat with significant PE (arrow), and (B) a control rat without PE.
C to **F**: Visualization of PE by cMRI (ECG triggered gradient echo image, TE=6.5ms, transverse axis) in same rats 19d (C: immunized; D: control) and 21d after immunization (E: immunized; F: control). PE shown in (E) amounted to ~2.5ml when the rat was sacrificed.

4.3. Myocarditis Phenotypes in EAM Lewis rat.

4.3.1. Histomorphologic and molecular characterization of EAM in the Lewis rat.

In order to characterize the kinetics of EAM-development, our immunized rats were sequentially sacrificed at predefined time points after immunization. The hearts from in total n=44/106 immunized and in total n=11/27 control rats served for these analyses (acute phase: d7, 14, 21, 28, and d35; early post-inflammatory phase (n= 16 EAM/4 control): d42, 45, 75, and d100; late (n= 20 EAM/5 control) (=chronic) post-inflammatory phase: d155 and d250; n=8 EAM-rats vs 2 control/time-point). Hearts were removed at the indicated time points and cardiac tissue sections were stained with HE and MGT to assess the development of cellular infiltrates and fibrosis, respectively. N=5/20 or 1/16 from our EAM-rats died in the acute or early post-inflammatory phase, respectively, whereas 0/8 EAM-rats died in the late phase. Anti-CD68-immunostaining served to analyze the amount of monocytes and macrophages within the cellular infiltrates and anti-cleaved caspase 3 -immunostaining served to follow the kinetics/time-course of collagen deposition.

4.3.2 Acute Inflammatory Phase

Cardiac tissue sections representative for the acute inflammatory phase (d21) are shown in **Figs. 3A and B**. HE-stains of the hearts of EAM-rats generally showed massive myocardial infiltrates in the left (sometimes times also right) ventricles predominantly localized in sub-epicardial regions and only few infiltrates in the septum. Anti-CD68-immunostaining revealed that monocytes and macrophages represented the predominant cell-populations in such infiltrates (**Figs. 3C, F and G**). In contrast, MGT stains at 21d did not show any relevant fibrosis.

4.3.3 Chronic (post-inflammatory) fibrotic phase

In the chronic phase, HE-stains showed some residual myocardial lesions, disappearance of cell-infiltrates, and numerous scars (**d250: Figs. 3 H and K**). MGT staining underscored that these lesions were fibrotic (**Fig 3I, 3L**) and anti-cleaved caspase-staining (**Figs. 3J; magnification 3N**) revealed abundant collagen depositions (=fibrosis) with only few intact myocytes and almost no macrophages in such areas, as shown by anti-CD68 staining (**Fig. 3M**).

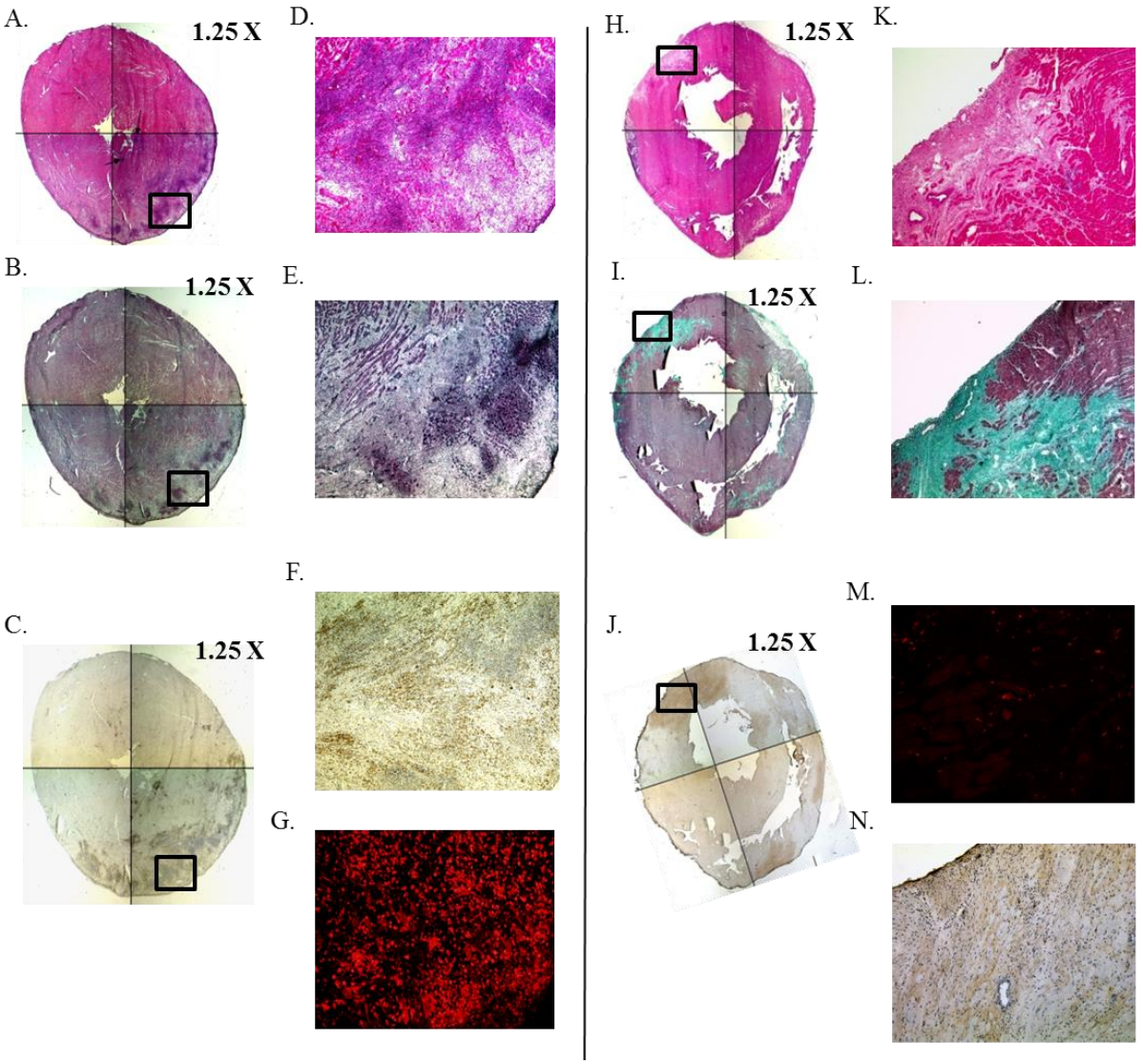

Figure 3: Myocarditis-phenotypes in the Lewis rat

A to G: Histologic assessment of the early inflammatory phase: (A) Hematoxylin & Eosin (HE)- or (B) Masson-Goldner Trichrome (MGT)-stained mid-ventricular sections of a representative rat heart 21d after EAM-induction. (D and E): Magnifications revealing sub-epicardial lesions in the lateral wall with cell-infiltrates (arrows). (C) Biotinylated anti-CD68-staining reveals a large number of infiltrating macrophages in midventricular sections. (F) Magnification revealing subepicardial macrophage infiltration (arrows). (G) Magnification revealing subepicardial macrophage infiltration (immuno-fluorescence) (arrows).

H to N: Histologic assessment of the late (chronic) post-inflammatory phase: (H) HE- or (I) MGT-stained mid-ventricular sections of a representative rat heart 155d after EAM-induction. (K and L): Magnification demonstrating displacement fibrosis (arrows). (J) Biotinylated anti-cleaved caspase 3 antibodies revealing collagen deposition in the left ventricular lateral wall. (N) Magnification of healed myocardial tissue. (M) Anti-CD68-staining reveals some single (physiologic) macrophages.

4.3.4. Kinetics of macrophage infiltration

Inflammatory activity in heart sections of immunized versus control rats was analyzed by anti-CD68 immuno-staining. Representative images of myocardial sections from immunized EAM-rats sacrificed at pre-defined time points (i.e. days 7, 14, 21, 28, 35, 38 and 40) are shown in **Figure.4**. Semi-quantitative analyses indicate a peak in cellular infiltration around d21 after immunization (**Fig. 4C**); in the following, the number of anti-CD68 positive cells declines gradually over time (day 35-45). ~ 23% of our EAM-rats died in the acute or early inflammatory phase (i.e., d7-d35) due to fulminant heart failure or sudden cardiac death. None of the animals died in the chronic phase (i.e., d101-250). No cellular infiltrates were noted in control rats injected with 0.9% NaCl (**Fig. 4H**).

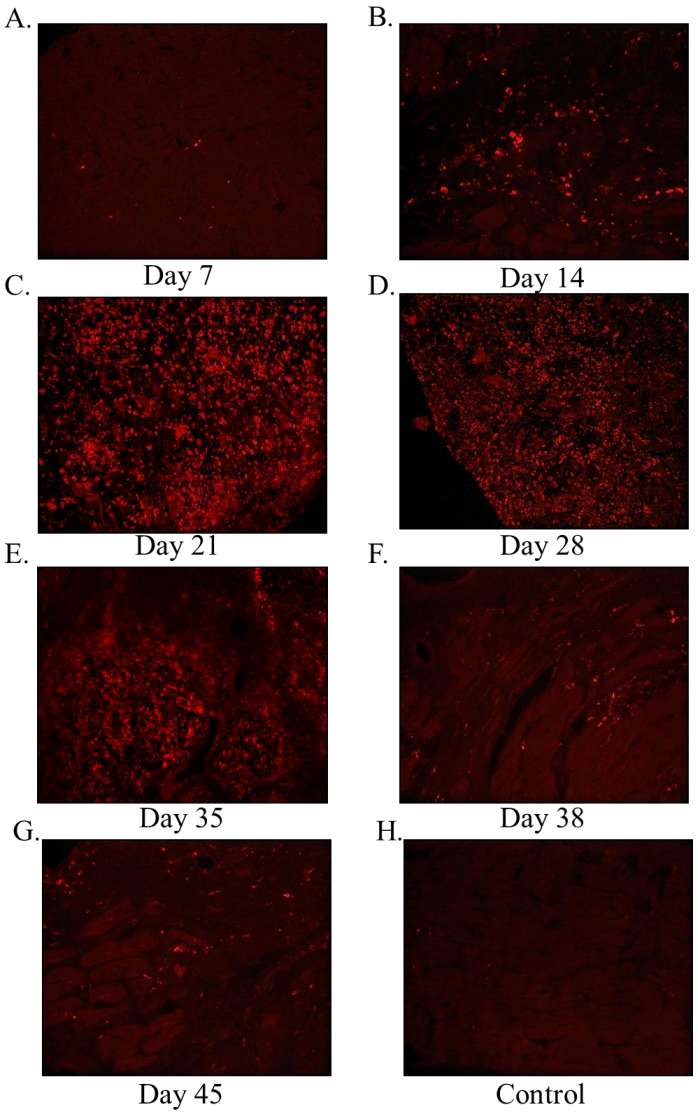

Figure 4: Kinetics of macrophage infiltration.
A to H: Macrophage-infiltration was determined by anti-CD68 immuno-staining at various time points (d0, d7, d14, d21, d28, d35, d38 & d45). Semi-quantitative computer-aided image analysis revealed that the maximal cellular infiltration was achieved on d21 post immunization. Thereafter, the number of monocytes and macrophages slowly but continuously decreased until d 45.

4.3.5. Kinetics of fibrosis development

Development of fibrosis in the acute phase, post-inflammatory phase and, most important, chronic phase was followed by MGT staining of cardiac tissue sections from immunized versus control rats (**Fig. 5**). The animals were sacrificed at predefined time points (**see Figure 4**) and excised hearts were MGT stained. The amount of fibrosis was semi-quantitively assessed by computer-aided image analysis by calculating % green coloured pixels/section of

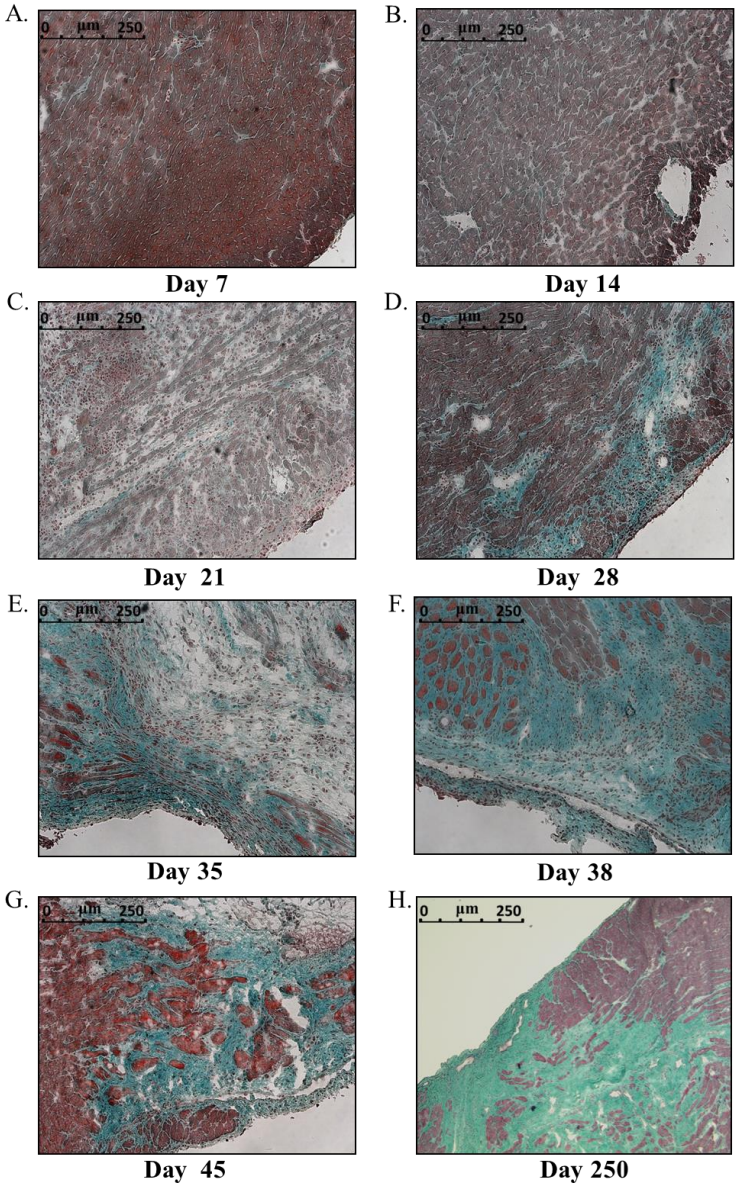

Figure 5: Kinetics of fibrosis development.
A to H: Fibrosis development (collagen deposition) was assessed by Masson Goldener Trichrome (MGT) staining suited for distinguishing cells (brick red) from surrounding connective tissue (green). Mid-ventricular 3µm-sections from EAM-hearts obtained at different time points after immunization (d0, d7, d14, d21, d28, d35, d38, d45 and also d196) were analyzed for their collagen content. Semi-quantitative computer-aided image analysis of these successively obtained cardiac sections revealed that fibrosis development starts as soon as d21 and then continuously increases until d 45, and then remains almost unchanged for a long time (e.g. d 250)

mid ventricular heart sections. Collagen deposition starts as soon as day 14 (**Fig. 5d**) in the previously inflamed myocardial areas but becomes clearly visible only from d28 (**Fig. 5D**). The development of fibrosis is due to a deposition of collagen fibers in necrotic cardiac tissue, thus contributes to myocardial 'scar' formation. Scars, once installed, remain constant for life time (**Fig 5H- d250 post- immunization**).

In contrast to the acute and early inflammatory phase, none of our EAM-rats died during choric phase, even though extensive fibrotic lesions were noted post-mortem. Our findings demonstrate that development of fibrosis parallels the disappearance of macrophages. No relevant fibrosis or any functional / structural defects were observed in control animals during 250 days of follow up.

Figure 6 illustrates the time-course of macrophage infiltration and fibrosis-development in n=44 EAM-rats (n=4/time-point). Macrophage infiltration (as determined by anti-CD68-staining) was detectable as soon as ~7d and peaked ~21d after immunization. Thereafter, cellular infiltrates declined constantly with a negligible number of macrophages present in myocardial lesions ~100d after EAM-induction (red line in **Fig. 6**, N=36 rats; n=4/time-point). Collagen-depositions were noted from d14 on (**fig. 5**) and the continuously increased until d40. In the late inflammatory phase, the amount of collagen remained almost constant during follow up. (green line in **Fig. 6**). Although animals were not the same between (longitudinal) time-points, our data strongly suggest that in the Lewis-model disappearance of macrophages is accompanied by replacement-fibrosis in previously cell-infiltrated areas, which -once installed- remains constant from d42 to d250 after EAM-induction (**Fig. 6**).

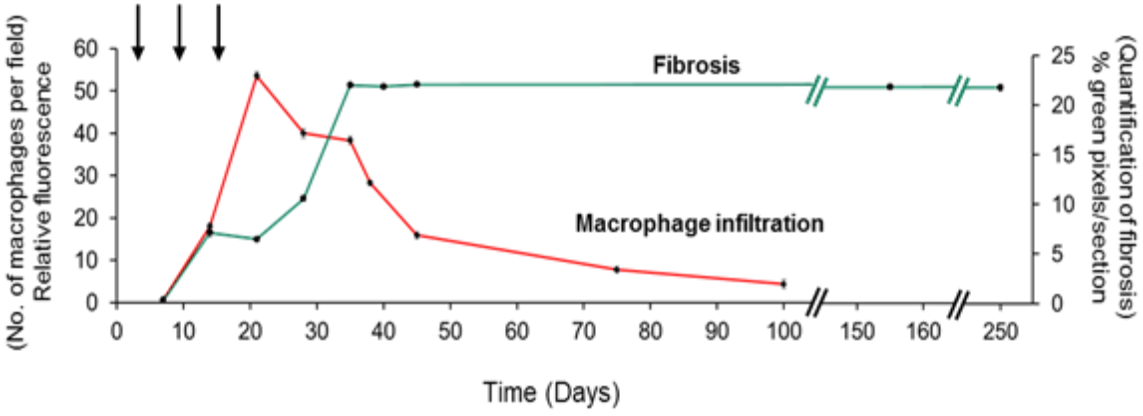

Figure 6: Time course of cellular infiltration and subsequent fibrosis development.
Time-course of macrophage-invasion (red) and fibrosis-development (green) in the early and late (chronic post-) inflammatory phase in n=44 EAM-rats (4/time-point). Macrophage-infiltration peaks on d21 after EAM-induction; from d28 on fibroblasts invade previously cell-infiltrated areas. Arrows indicate antigen-boosts.

4.3.6. Expression of pro-inflammatory, pro-fibrotic and fibrotic markers.

In addition to a comprehensive histo-morphologic assessment, the cardiac expression of pro-inflammatory/pro-fibrotic and fibrosis markers was analyzed by RT-PCR using cardiac tissues harvested 21d after immunization (n=5-11 immunized *vs.* 4-5 control rats per marker, comprising hearts from EAM-rats subjected to histological analysis or to ferumoxytol-enhanced cMRI). Based on the mRNA-expression profiles our rats could be divided into two groups; one group (***reaction pattern 1***) with animals still exhibiting a high expression of pro-inflammatory/ pro-fibrotic markers such as IL6, IL17a, OPN, ILbeta1, TNFα, IL23α, and MMP 9 (**Figs. 7A and B, grey columns**), and another group (***reaction pattern 2***) with animals already presenting a high expression of fibrosis markers such as collagen I and III, as well as LOX2, and MMP14 (**Figs. 7A and B, black columns**). This observation of two reaction-patterns after immunization was confirmed by histology: Heart-sections of rats with ***reaction pattern 1*** on d21 still presented large cellular infiltrates and only few collagen-deposits; hence, in this group development of fibrosis appeared to be delayed. In contrast, in animals with ***reaction pattern 2*** fulminant inflammation was already resolved; apparently, this animal-group underwent a rather short inflammatory phase and developed fibrosis as soon as 21d after EAM-induction. In fact, in this group fibrosis markers were already significantly up-regulated at d21.

Taken together, our results strongly suggest that, albeit using a same immunization-procedure, the individual genetic and/or immune background of an animal determines the intensity, duration, and pattern of an immune-response to inflammatory cardiac injury.

A.

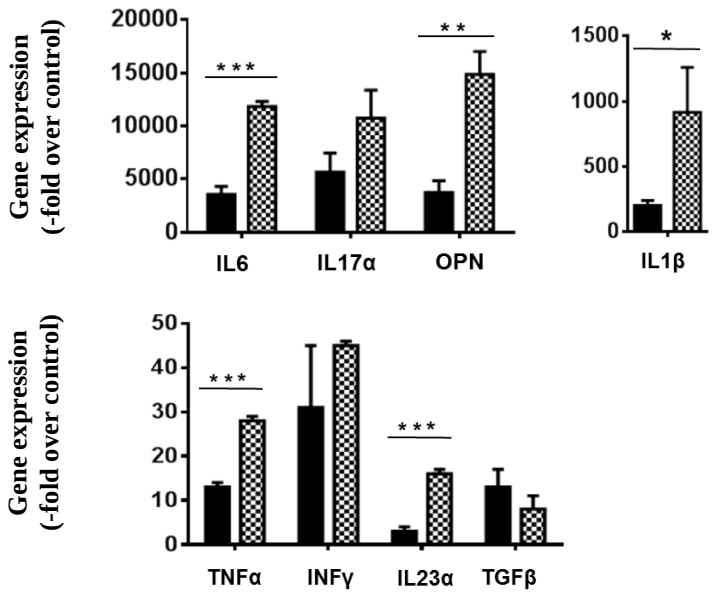

Figure 7 A: Molecular markers of inflammation
Heart-specific expression of the pro-inflammatory marker genes IL6, IL17a, OPN, IL beta1, TGFβ , TNFα MMP9 and TIMP1 in n=5-11 immunized Lewis rats as revealed by real-time PCR at d21 after induction of myocarditis (grey), compared to n=4 age- and sex-matched control animals (black). Error bars correspond to the respective mean values ± s.e.m; *p<0.05, **p<0.01, ***p<0.001. Pro-inflammatory markers revealed up-regulation of INFγ, along with IL18 and IL12 (data not shown) indicating activation of the TH1-pathway in immunized rather than in control rats.

B.

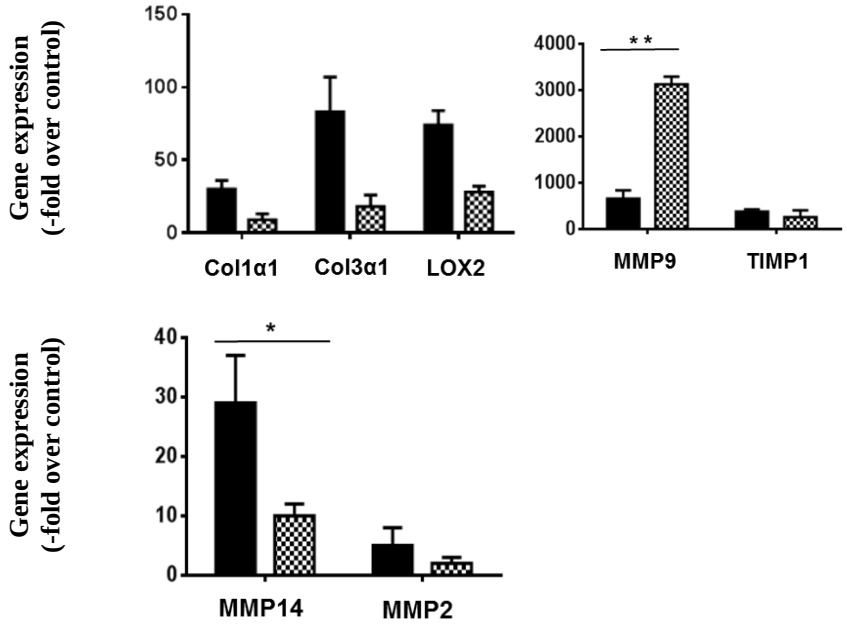

Figure 7 B: Molecular markers of early fibrotic replacement
Heart-specific expression of the pro-fibrotic markers collagen I, collagen III, LOX2, MMP2, and MMP14 in n=5Lewis rats at d21 after induction of myocarditis (grey) as detected by real-time PCR, compared to n= 4 age- and sex-matched control animals (black). Error bars correspond to the respective mean values ± s.e.m., *p<0.05, **p<0.01.

4.4. Visualization of cellular infiltrates by contrast-enhanced cardiac MRI

In order to visualize cellular infiltrates, highly biocompatible ultra-small sized iron oxide particles 'Feraheme®' were used for our experiments. We sought to determine the capability of this iron particle to detect myocardial inflammation. Animals were routinely scanned by cMRI on d21 post-immunization. After injection, Feraheme® (ferumoxytol) is cleared from the circulation within 48 hours; therefore a minimum gap of 48 hrs was kept between injection and cMRI. Feraheme® injections were carried out on different time points (48 hrs, 72 hrs, 96 hrs and 120 hrs). Two different doses of Feraheme® (15mg/kg body, 20mg/kg body) were tested in immunized versus control animals. As shown before, cMRI of the hearts of successfully immunized animals always revealed massive pericardial effusion surrounding the heart. However, at the same time the myocardium appeared to be homogenous without any focal or diffuse MRI-signals after clearing of Feraheme® from the blood. After total clearance of Feraheme® from the blood, we expected specific 'late' signals arising from iron-oxide engulfed macrophages within in the inflamed myocardium (against the homogenous background). Data from experiments with different doses and clearance times are presented in the following section.

4.4.1. *In vivo* cell tracking by MRI using USPIO's (Feraheme®)

4.4.1.1. *In vivo* application

Figure 8 (A) shows a representative cMRI image from an immunized animal (injected i.v.15mg/kg body on day 19; image acquired **2** days post contrast agent injection). No clear hypointense contrast due to cellular infiltrates is seen in USPIO-enhanced cMRI scans (**d21; Fig. 8A**). The homogenous dark endocardium does not qualify as a specific signal .The hypo-intensity in the endocardial region is a motion artifact due to rapid breathing (arrows). MGT staining (**d21; Fig. 8B**) of the same heart revealed cellular infiltrates in the lateral left ventricular wall and fibrosis of the right ventricular wall. Histological findings do not correlate with the MR-images. Control animals injected with 15mg/kg body weight of Feraheme® scanned in parallel do not show any hypointense MR-signals (**d21; Fig. 8C**) and no cellular infiltrates in histology (**d21; Fig. 8D**).

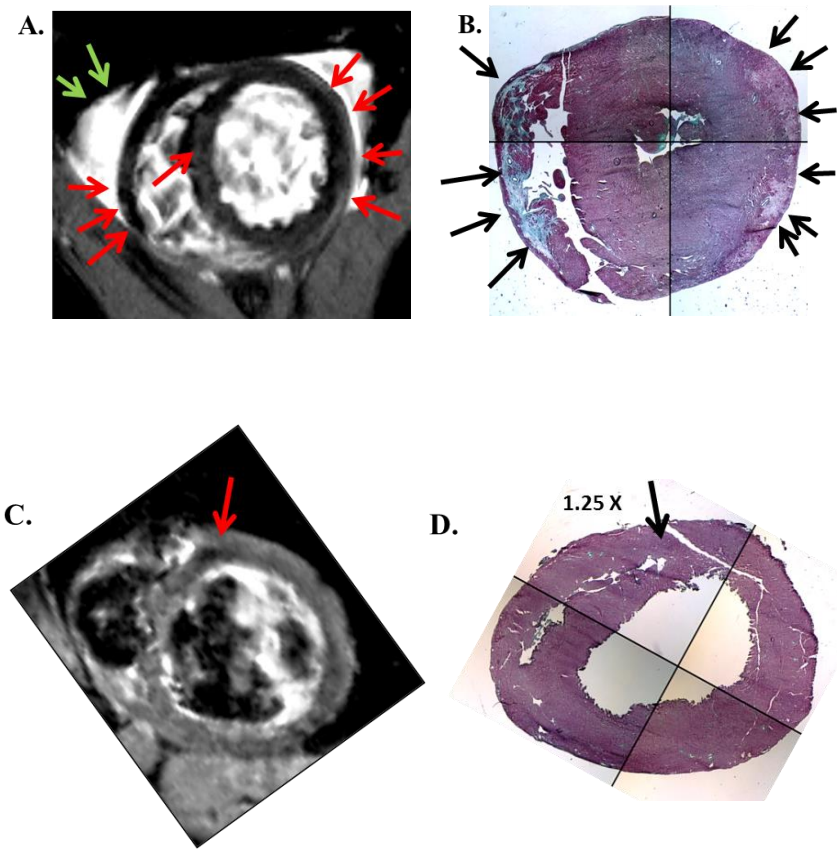

Figure 8: Detection of cellular infiltrates by using Feraheme® (USPIO) and comparison with histology.
A, B: (A) Representative MR-image from a myosin-immunized rat (d19), measured 2 days post contrast agent; Feraheme® concentration 15mg/kg body weight. Pericardial effusion can be seen surrounding the heart (green arrows). Hypointensity can be seen in the RV region, lateral inferior wall and part of the septum (red arrows). (B) Histologic section from the same heart, depicting areas of collagen deposition in the RV wall and focal cellular infiltrates in the epicardium (lateral free wall; arrows). The low signal intensity in the ventricular wall does not correlate with the region(s) of cellular infiltration or fibrosis in the histological sections.
C, D: (C) Representative MRI image from a 0.9% NaCl- injected control rat (d19), (measured 2 days post contrast agent, Feraheme® concentration 15mg/kg body weight). MRI signals in the myocardium appear very homogenous except for a focal signal loss in the inferior septal region (arrow) (D) Histological analysis of the same heart did not show any cellular infiltrates in the inferior septal region.

Fig. 8E and F represent images of mid ventricular heart sections from immunized animals injected with **20mg/kg body** weight of Feraheme®. The contrast agent was injected 72 hrs prior to the cMRI scans; images were acquired **3** days post-contrast agent application. In the cMRI image (**d21; fig. 8E**) hypointense dispersed MR-signals can be seen in the left lateral posterior wall and the right ventricular wall of the immunized animal. When compared

with histology (**d21; fig. 8F**), no cellular infiltrates could be observed in these regions. The control animal did not show any specific MRI-signals and no cellular infiltrates (**Fig. 8G and Fig. 8H**).

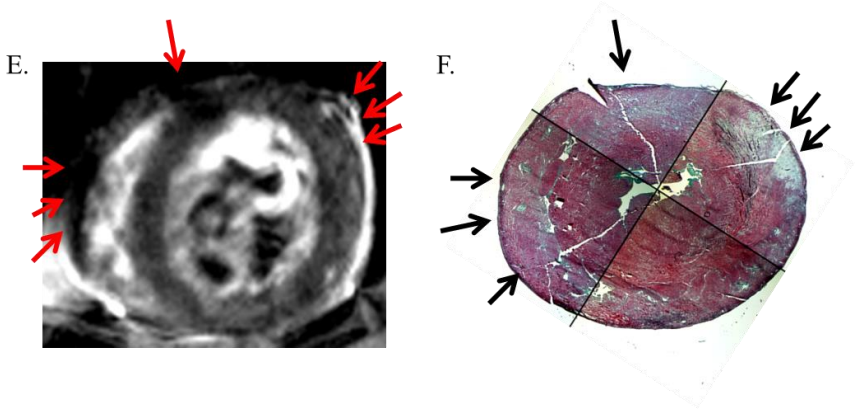

E, F: (E) Representative MR-image from a myosin-immunized rat (d21), measured 3 days post, Feraheme® injection (20mg/kg body weight). A small amount of pericardial effusion can be seen surrounding the myocardium. Loss of signal can be seen in the RV-wall, LV-inferior wall and septal region. (F) HE-stained section from the same heart showing areas of huge cellular infiltrates in left ventricle and sparse infiltration of the inferior wall. The MRI findings do not correlate with the distribution of cellular infiltrates in the histologic section.

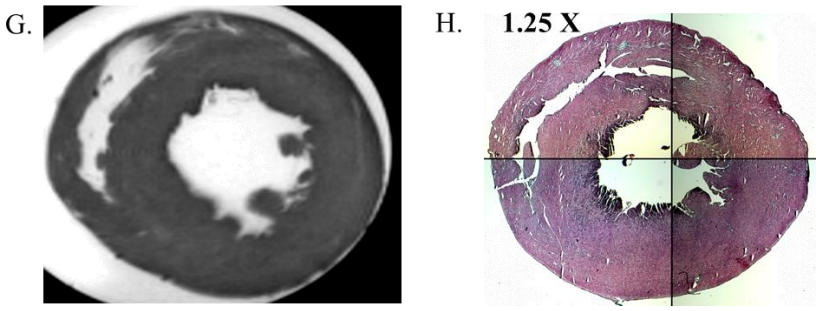

G, H: (G) Representative cMRI ex vivo image from a 0.9% NaCl-injected control rat (d19), (measured 3 days post, Feraheme® injection (20mg/kg body weight). The cMRI image appears very homogenous without any loss of signal. (H) Histological analysis from the same heart did not show any cellular infiltrates.

Figure 8I represents a scan of the heart of a cMRI immunized animal injected with 20mg/kg body weight of Feraheme®; images were acquired **96hrs** post-contrast agent application. In **Figure 8I,** hypointense focal signals can be detected in the right ventricular wall (arrows) and breathing artifacts in left ventricular and septal region. Histology did not reveal any cellular infiltrates in the RV wall whereas many infiltrates were present in the

lateral wall of the left ventricle (**Fig.8J**). Control animals showed a mild loss of signal intensity in the right ventricular border but no focal cellular infiltrates were seen in histology (**Fig. 8K and Fig. 8L**).

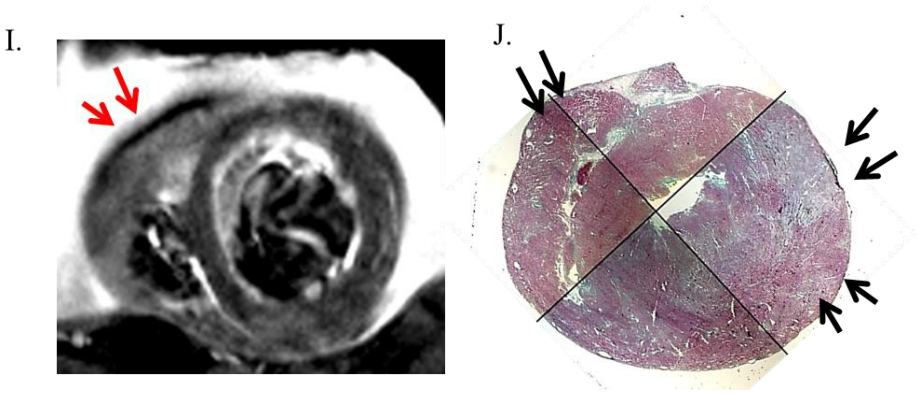

I, J: (I) Representative MR-image from a myosin-immunized rat (d21), measured 4 days post contrast agent, Feraheme® injection (20mg/kg body weight). A small amount of pericardial effusion can be seen surrounding the myocardium. Loss of signal can be seen in RV border (arrows). (J) HE-stained section from the same heart depicting areas of huge cellular infiltrates in the left ventricle and sparse infiltrates in the inferior wall. Myocardium of non-immunized control rats injected with 0.9% NaCl appeared homogenous and histology revealed no cellular infiltrates in the myocardium (data not shown)

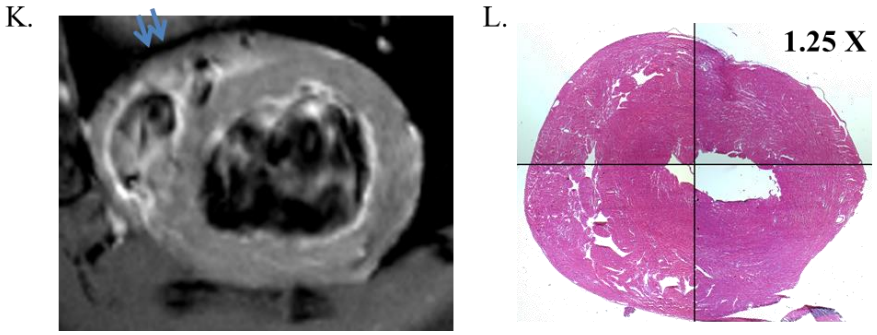

K, L: (K) Representative MRI image from a 0.9% NaCl- injected control rat (d19), measured 2 days post Feraheme® injection (15mg/kg body weight). MRI scans of the myocardium appear very homogenous except a signal loss in the RV border (shown by arrows) (L) Histological analysis from the same heart did not show any cellular infiltrates.

Fig. 8M shows the cMRI image of mid-ventricular heart section from an immunized animal (d21 of immunization) which was highly reactive to cardiac myosin, showing a huge amount of pericardial effusion (~ 2.5ml) and massive cellular infiltrates in the left ventricular region. The scan was performed **120 hrs** post contrast agent injection (Feraheme® 20mg/kg

body weight). The cMRI image shows LV-thickening along with low intensity signal loss. Histology revealed severe inflammation (**d21; Fig. 8N**) but not intense Feraheme® signal from the can be seen. Control animals (**Fig. O and P**) did not show any signal voids due to Feraheme® uptake and no cellular infiltrates was seen in histology.

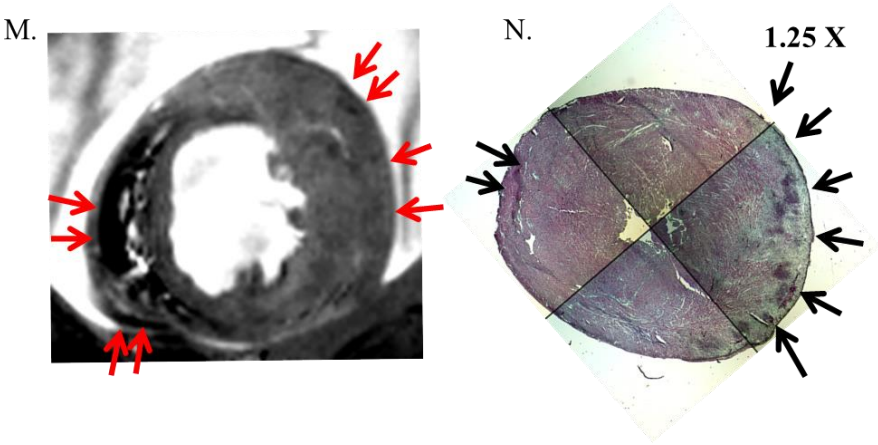

M, N: (M) Representative MR-image from a myosin-immunized rat (d22), measured 5 days post Feraheme® injections (20mg/kg body weight). A massive amount of pericardial effusion accompanied by myocardial edema can be seen surrounding the heart. Some focal signal loss can be seen in the thickened LV wall. (N) Histological findings of the same section indicate massive cellular infiltrates in the left ventricular region. MRI findings mildly correlate with the histological findings.

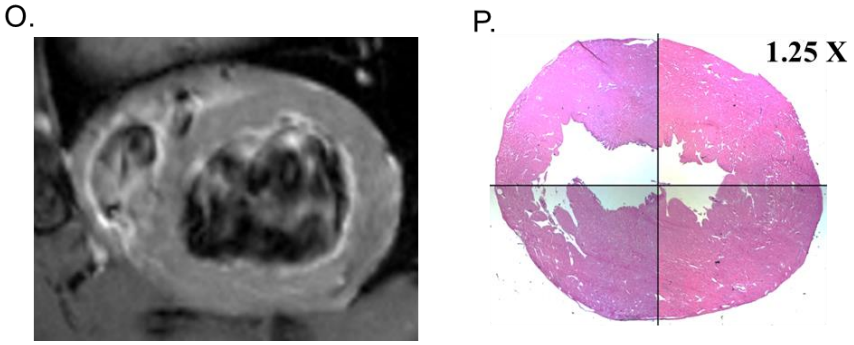

O, P: (O) Representative MRI image from a 0.9% NaCl- injected control rat (d19), measured 5 days after Feraheme® injection (20mg/kg body weight). The MRI signal in the myocardium appears to be homogenous and no signal loss can be seen in any region. (P) Histological analysis from the same heart did not show cellular infiltrates.

4.4.1.2 USPIO (Feraheme®)-uptake in macrophages and monocytes

To confirm the initial hypothesis that, iron oxide might be engulfed by invading macrophages, we analyzed mid-ventricular heart sections by Pearl's Prussian blue staining for iron deposits. In **Figure 9A-C**, heart tissues with fibrosis and inflammatory lesions show some slight blue colored single or grouped cells, supposed to represent iron oxide particles engulfed by macrophages. The ratio between iron oxide-containing cells as compared to the total number of infiltrating cells was rather low. Hence Feraheme® uptake by inflammatory

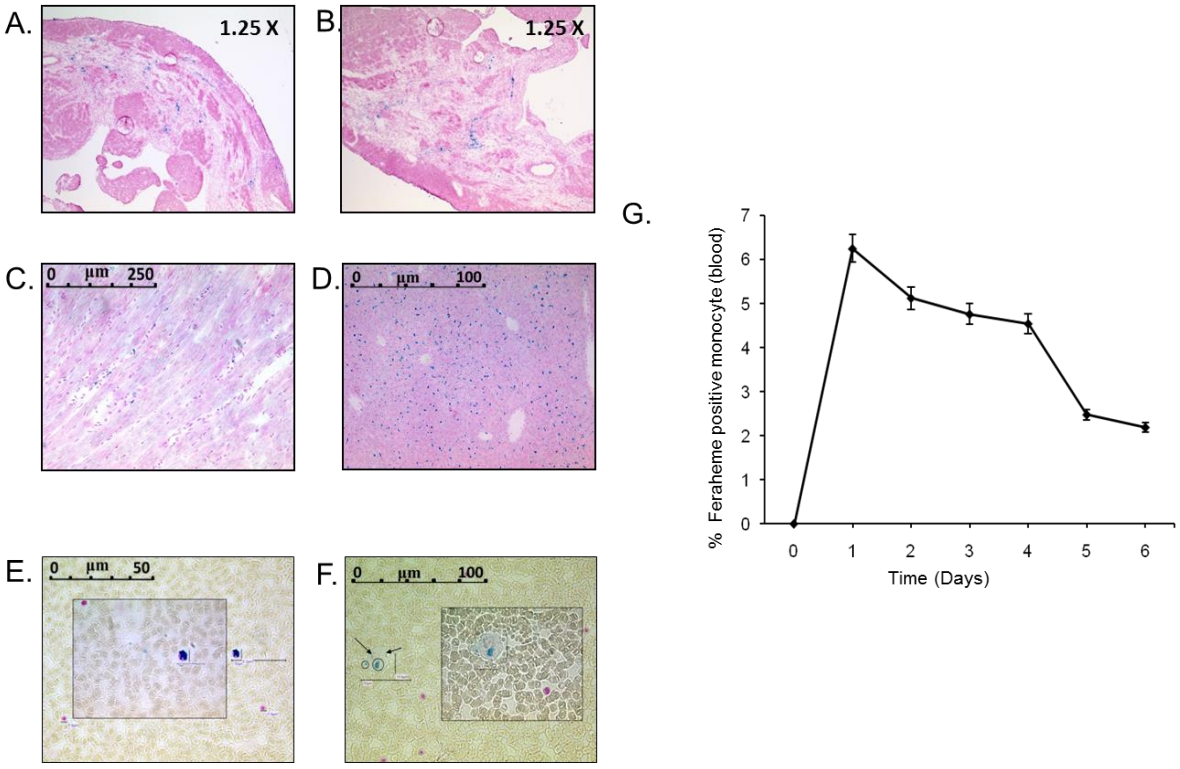

Figure 9: Feraheme®-uptake in macrophages and monocytes.

(**A-C**) Feraheme® particles (iron oxide) appear blue, whereas nuclear infiltrates appear dark pink (arrows). Less than 2% of the infiltrating inflammatory cells were found positive for iron uptake. **D:** Liver section revealing a huge amount of Feraheme® (iron oxide) deposition in the organ. **(E)** Iron-labeled macrophage or (**F**) monocyte in a blood sample taken 48h after one single Feraheme®-injection (15 mg/kg BW), assessed by Perl's Prussian blue-staining (arrows).

(G) Time-course of iron-labeled macrophages in the circulating blood after one single Feraheme®-injection (20mg/kg body weight).The graph depicts the percentage of monocytes tested positive for Feraheme® from the whole population of circulating monocytes (which in immunized animals comprises 4-6% of the phagocytes). The majority of cells were found to be positive one day post-iron injection. The number of iron-positive cells in the circulating blood decreases with time.

cells was negligible (less than 20% of total cells). **Fig.9D** shows representative liver tissue from the same animal, serving as a **positive staining-control**, because majority of iron particles are engulfed by kupffer cells and filtered by the liver.

Monocytes and macrophages labeled with iron-oxide after one single Feraheme® -injection (20mg/kg body weight) were detected by Perl's Prussian blue staining (**Fig. 9E and F**-monocyte and/or macrophage containing an iron particle). The graph in **Fig. 9G** shows the percentage of monocytes positive for Feraheme® compared to the total number of circulating monocytes (which in immunized animals comprise 4-6% of the immune cells). The graph shows that maximum circulatory cells are found 24 hours after Feraheme® injection.

4.4.2 *In vivo* Cell tracking using 'Micron Sized Iron Oxide Particle (MPIO)'

4.4.2.1 *In vivo* application

For MPIO-enhanced cMRI 0.9-μm MPIOs (5 mg/ kg body weight) emulsified in 0.9% NaCl were intravenously injected into immunized and control animals 24 hours before the scans. Still frames of cine series 21 days after immunization at end diastole **(Fig. 10 A-B**) and end systole **(Fig. 10 C-D)** clearly indicate septal hypokinesis, signifying impairment of cardiac function at that time point. Representative T_2*-weighted in *vivo* images are shown in **Fig. 10E** (**immunized heart**) and **10F** (**control heart**).

In EAM-rats a large number of hypointense signals were observed in the LV-myocardium, indicating cellular infiltrates. In contrast, only negligible areas of hypo-intensity could be detected in control animals (**Fig.10F**).

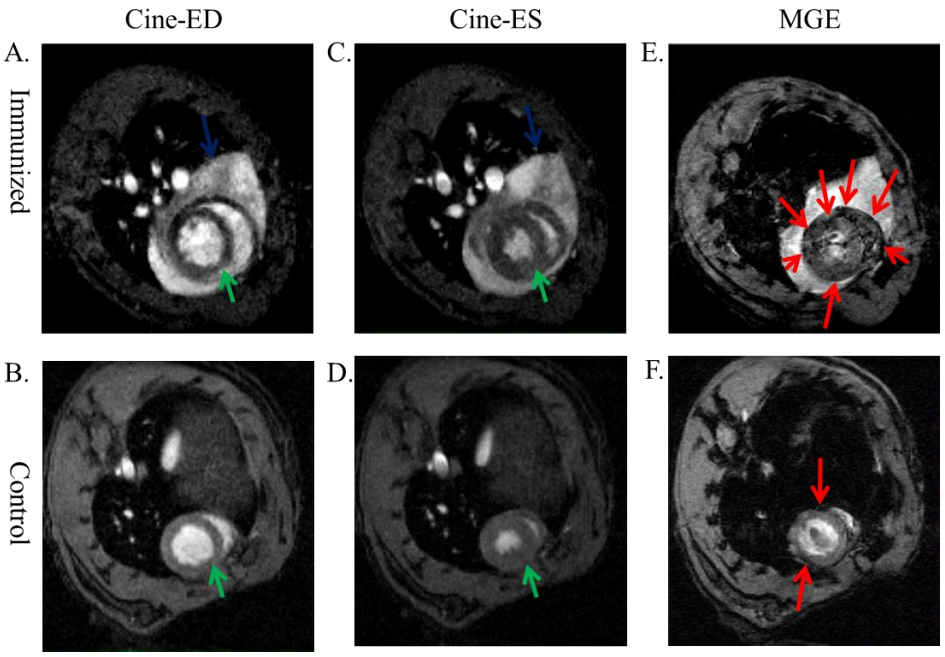

Figure 10: In Vivo cell tracking using MPIO (Bang laboratories -ME03F).
Still frames from a cine series at end diastole (ED) of an immunized **(A)** and a control animal **(B)** compared to an end systole (ES) series of the immunized **(C)** and control animal **(D)**. The images clearly indicate septal hypokinesis (green arrow) suggesting impaired cardiac function. A huge amount of surrounding pericardial effusion is present (blue arrow). T_2* weighted multi gradient-echo (MGE) image of the immunized animal **(E)** 1 day after administration of MPIO shows a large number of hypointense signals (red arrows) due to iron accumulation within the cellular infiltrates, whereas the control heart **(F)** appears homogenous.

4.4.2.2. *Ex vivo* application (*Ex vivo* MR Microscopy)

High-resolution MR microscopy on fixed tissue is more sensitive for the detection of MPIO-labeled cells in inflamed organs. **Fig. 11** shows MR microscopy images of an EAM rat 21 days after immunization with cellular infiltrates as confirmed by histology. **Fig.11 A-B** shows representative images of an **immunized and a control heart** obtained by RARE sequences. Multi gradient echo (MGE) T2*(T 2 star)-weighted images show punctate hypointense signals (**Fig. 11 E-immunized**), and each spot of hypo-intensity is discrete and circular when seen in high resolution, most likely resulting from individually labeled macrophages. Very sparse hypo-intense spots are seen in the control heart (**Fig. 11 F-control**).

Fig. 11G-11I represents MR-images of another **EAM-hearts** showing a different pattern of cellular infiltration in the myocardium. MGE-T2* weighted images reveal differences between a focal versus a patchy distribution of hypointense signals (**Fig. 11E**

versus 11I).These results are consistent with the disease pattern found in humans; in some case, the cellular infiltrates are focused at one point, whereas in some cases the cellular infiltrates are distributed in the entire myocardium.

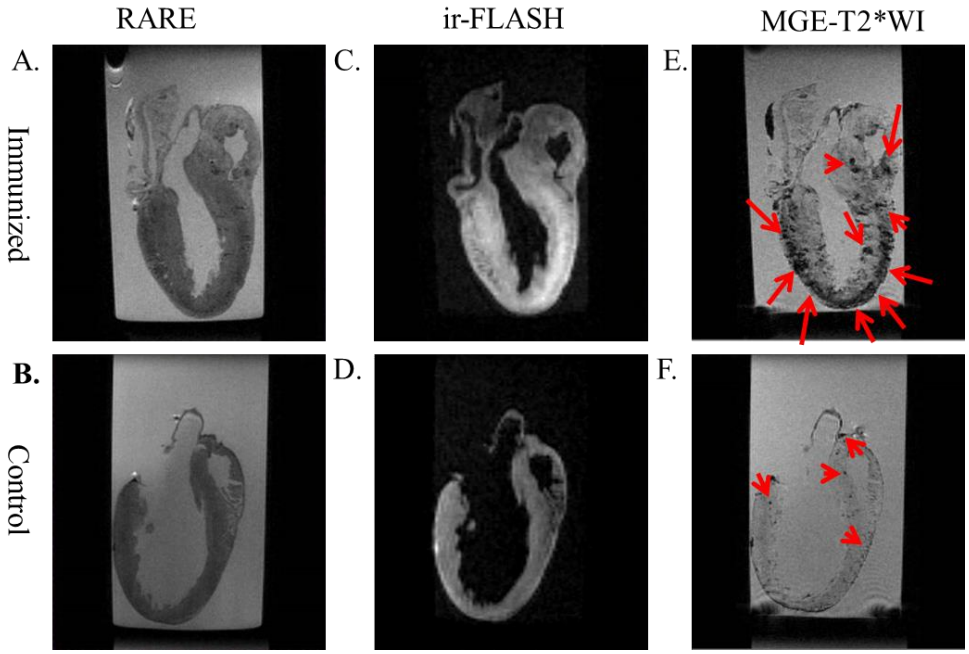

Figure 11: Ex VIVO Detection of cellular infiltrates by using MPIO and comparison of signal distribution in EAM-rats.
A, B: Representative MRI image from a myosin-immunized and a 0.9% NaCl-injected control animal 21 days after immunization, (measured 1 day post contrast agent application, MPIO concentration 5mg/kg body weight), demonstrating that the EAM-rat has a thickened myocardium compared to the control animal.
C, D: Immunized versus control rat using ir-Flash sequences confirm that the immunized animal has a thickened myocardium compared to control rat.
E, F: T2*-weighted ex vivo MRI with in-plane resolution of *156 um* after *in vivo* MPIO labeling. Hypointense signals can be seen in the EAM-heart (indicated by **red arrows**, which represent MPIO-labeled immune cells/macrophages), whereas, the control heart only shows few signals. Hypointensities in the EAM-hearts are mostly located in the sub-epicardial region of the heart. The sparse signals in the control animal are generally caused by small occluded vessels.

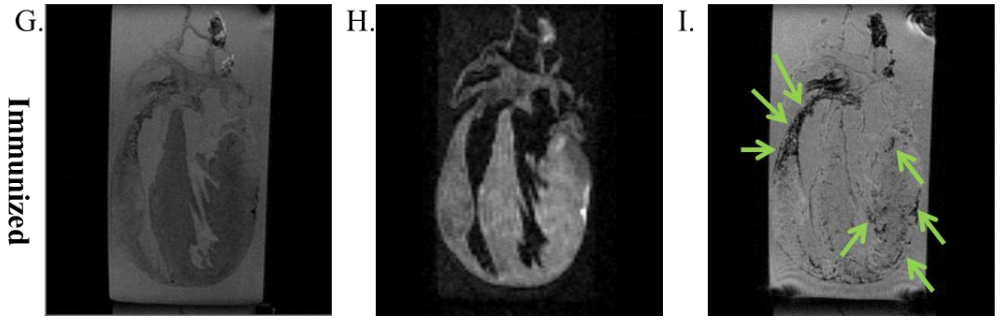

E, I: Comparison shows multiple hypointense signals (indicated by red and green arrows) which represent MPIO-labeled immune cells (mainly macrophages). On day 21 post immunization, myocardium from two different immunized EAM-hearts show distinct pattern of signal distribution. (E) Shows an intense (distributed) signal loss in the sub-epicardial left ventricular region, (I) show focal infiltration located in the right atrium and adjacent to the right ventricle.

4.4.2.3 MPIO -uptake in macrophages and monocytes

When T2*-weighted images are analyzed using a higher magnification, areas with an extensive loss of MR-signals correlate exactly with areas showing massive cellular infiltrates in histological HE-stains (**Fig 12 A-B**). The majority of these HE-stained cells were confirmed to be CD68- positive by immunostaining (**Fig. 12 C-F**). Further, when subjected to Perl's Prussian blue staining, myocardial areas with large cellular infiltrates were found to be positive for iron particles.

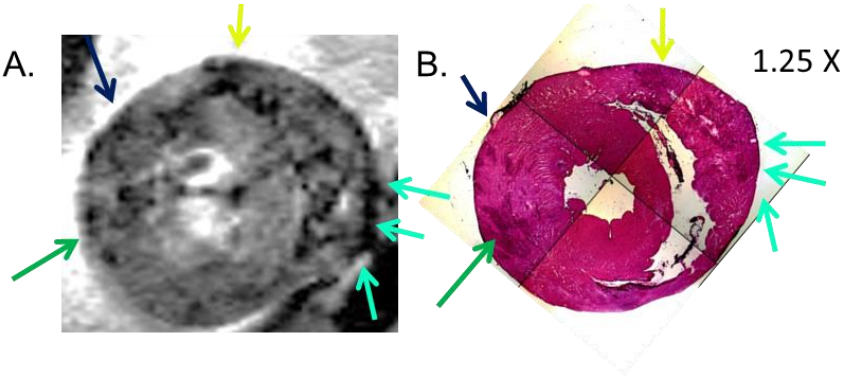

Figure 12: Ex Vivo histological analysis post MPIO cell tracking by MRI.
A, B: Representative T_2* - weighted *in vivo* MRI image compared to a HE-stained section from an EAM-heart 21 days after immunization. HE stained sections showing inflammation in the right and left ventricular sub-epicardial regions (arrows). The regions with massive cellular infiltrates correspond to the distribution of hypointense cMRI signals.

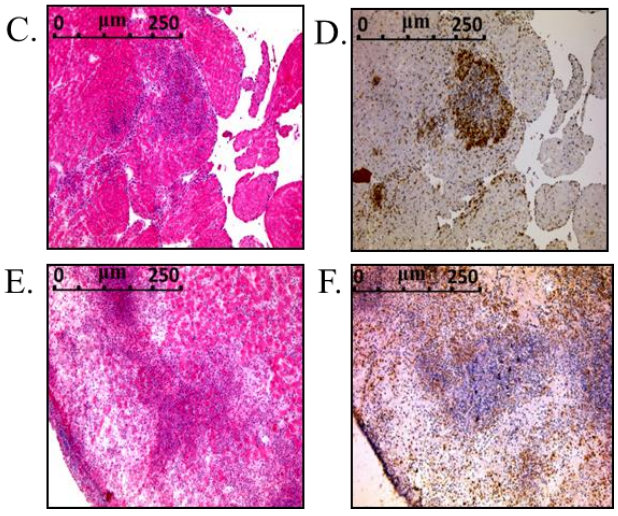

C-F: Correlation of HE stainings with anti-CD68-immunostainings of cellular infiltrates within the myocardium. The distribution pattern of anti-CD68-positive signals (dark brown colour) in the inflamed area clearly indicates that the majority of the cellular infiltrates consist of monocytes and macrophages.

Figures 12G-I, illustrate areas with cellular infiltrates consisting of many CD68-positive cells (brown- HRP immunostaining) that also contain iron oxide particles (blue- as derived from Perl's Prussian blue counter-staining).

G. H. I.

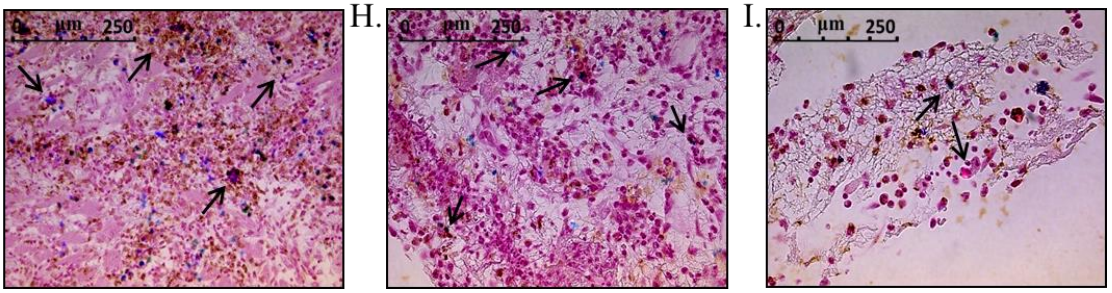

Correlation between Perl's Prussian blue and anti -CD68-positive cell staining.
G-I: Representative light microscopy images of myocardium infiltrated with immune-cell. Correlation of anti-CD68-immunostaining with Perl's Prussian blue reveals presence of iron particles (arrows) in a same region with monocytes and macrophages (brown color; avidin-biotin immunohistology). The distribution of iron particles in the inflamed region indicate uptake of MPIO's by circulating monocytes/macrophages.

4.4.2.4 Analysis of MPIO by iron-uptake by CD68 positive macrophages by Flowcytometry.

To analyze MPIO-uptake by macrophages, the MPIO particles were washed and resuspended in 0.9 % NaCl. Then macrophages and monocytes were isolated from the blood and labeled with anti-CD68 antibody, which were counter-stained with Dy-light 405 conjugated secondary antibodies. The prepared MPIOs were incubated with isolated anti-CD68 macrophages and monocytes for 24hrs at 37^{o} C and subjected to flow cytometry. Results show that the cell cluster without any MPIO-uptake was located near the red filter (**Fig. 13 A- Cells without MPIO; control cells immunostained with anti-CD68 antibody**). MPIOs were much smaller in size and found to be located at the extreme end of the green filter (**Fig. 13 B – MPIO particles without cells; MPIO particles have an in-built dragon green fluorescent core**). Macrophages and monocytes containing iron-oxide particles anti-CD68 positive are located in the 'R1 region' in **figure 13 C**. Further analysis (**Fig. 13 D**) of the Dot Plot (FL1-H Vs FL2-H) revealed that 25.16 % of the CD68 positive macrophages engulfed MPIO particles. 35.86% of the CD68 positive cells were did not contain any MPIO particles and 38.97% cells were negative for both CD68 staining as well as iron uptake.

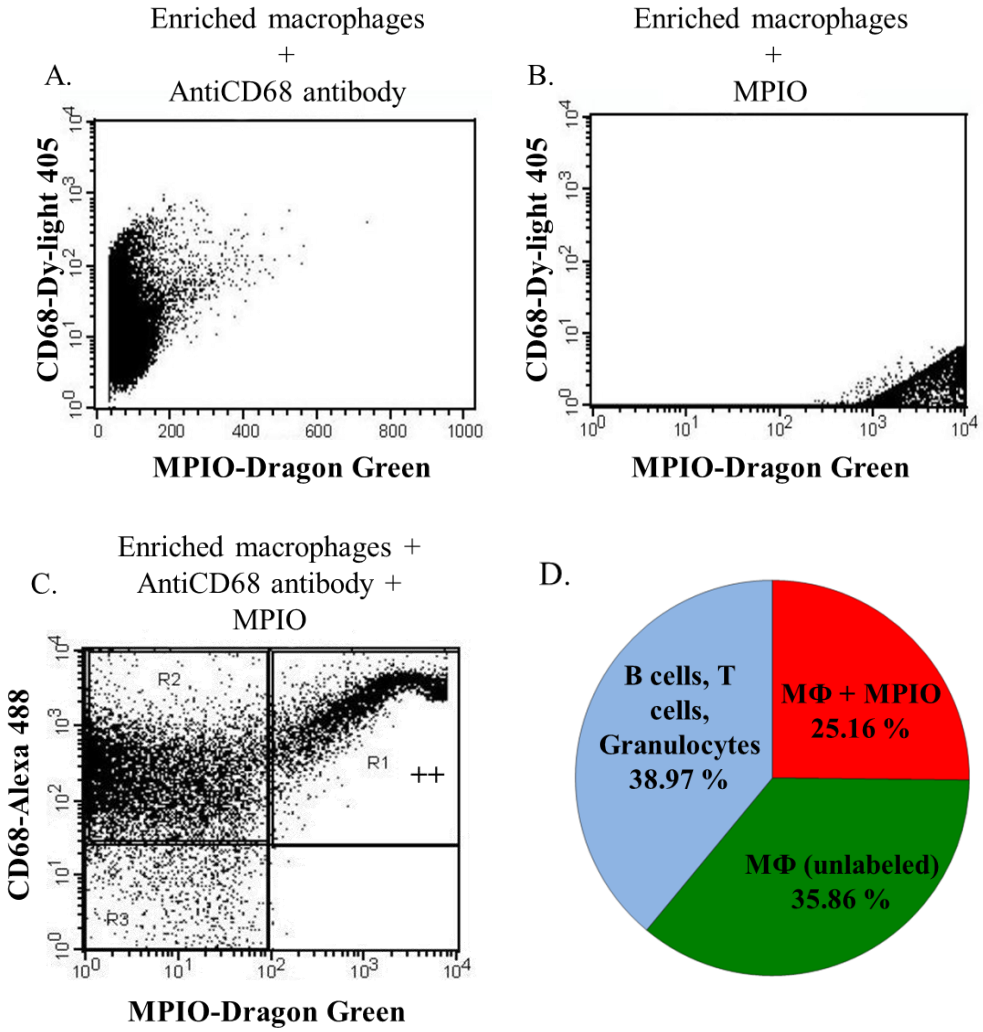

Figure 13: FACS analysis of enriched macrophages after exposure to MPIO particles. **(A)** Dot plot analysis of enriched macrophages stained with anti-CD68 antibody shows a cluster of cells located near the FL2-H (red) filter, indicating cells positive for red fluorescence (CD68 surface antigen) **(B)** Dot plot analysis of enriched macrophages supposed to contain iron particles shows a cluster of cells positive for green fluorescence (MPIO particle) located in the extreme end of the FL1-H (green) filter **(C)** Dot Plot analysis of green (FL1-H) vs. red (FL2-H) fluorescence revealed three distinct cell clusters represented as R1, R2, and R3. R1 represents the cell population positive for green (iron particles) and red (anti-CD68 antibodies) fluorescence. The R2 cluster represents the cell population positive only for red (anti-CD68 antibody) fluroscence. The R3 cluster represents the cell population negative for both red and green fluroscence. **D)** Further analysis of the FACS analysis revealed that the CD-68 positive macrophage population with iron (MPIO) uptake represents about 25% of the entire cell population of these enriched macrophages.

4.5. Visualization of cellular infiltration by nuclear tracers

4.5.1. ^{67}Ga-citrate and ^{99m}Tc-tetrofosmin

To further explore the imaging modalities for detection of myocardial inflammation, in the next step, we tested the suitability of ^{67}Ga-citrate (non-specifically binding to lactoferrin and transferrin) to detect inflammatory lesions in our animal model. To visualize myocardial perfusion, in-parallel we injected ^{99m}Tc-tetrofosmin intravenously. Immunized rats exhibited clear myocardial perfusion defects (**Fig. 14A**, arrows) along with a high focal uptake of ^{67}Ga-citrate in same regions (**Fig. 14B**, arrows). HE-stains (**Figs. 14C and D** [insert]) and anti-CD68-staining of corresponding heart-sections (**Figs. 14E** [Hoechst] **and F**) confirmed the presence of inflammatory cells (mostly macrophages) in these areas, while no infiltrates were visible in ^{67}Ga-citrate-negative control-rats (**Figs. 14G-L**).

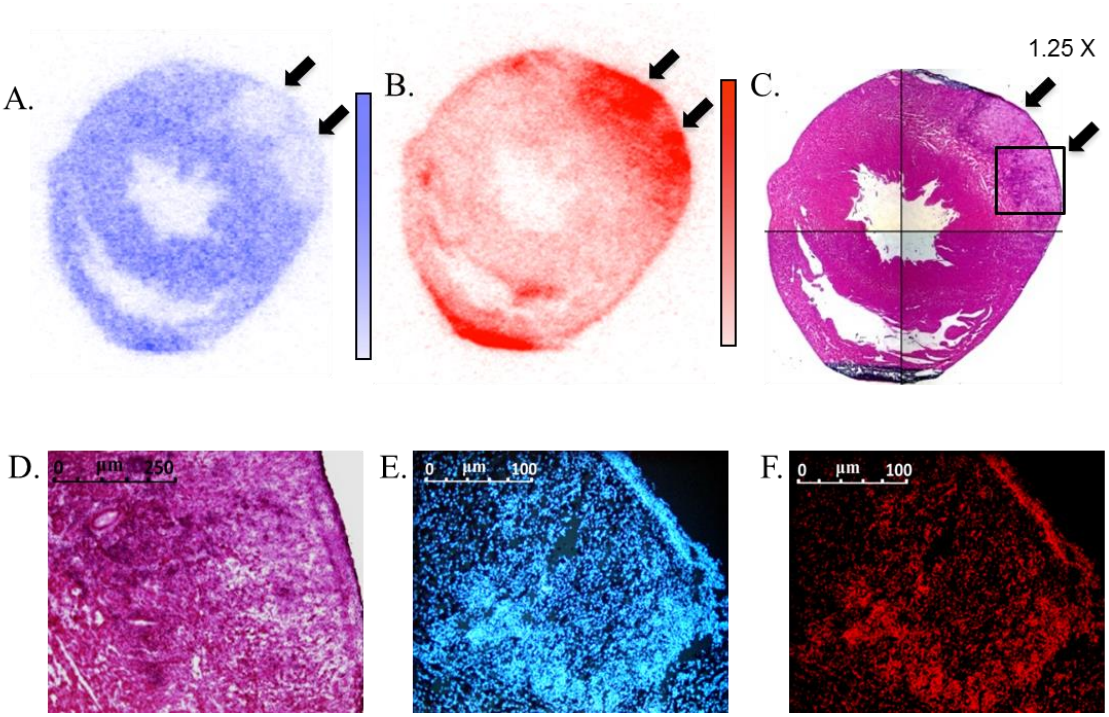

Figure 14: Scintigraphic detection of myocardial inflammation and correlation with histology.
(**A**) Representative autoradiograms from an immunized rat 21d after EAM-induction using ^{99m}Tc-tetrofosmin as a tracer for myocardial perfusion, and (**B**) ^{67}Ga-citrate as a tracer for inflammation. Arrows in A and B indicate cardiac areas with a perfusion defect caused by cell-infiltrates. (**C**) HE-stain of the same heart-section, and (**D**) magnification of an area with cell-infiltrates. (**E**) Corresponding nuclear staining (Hoechst). (**F**) Anti-CD68-staining confirming the presence of macrophages in the infiltrates.

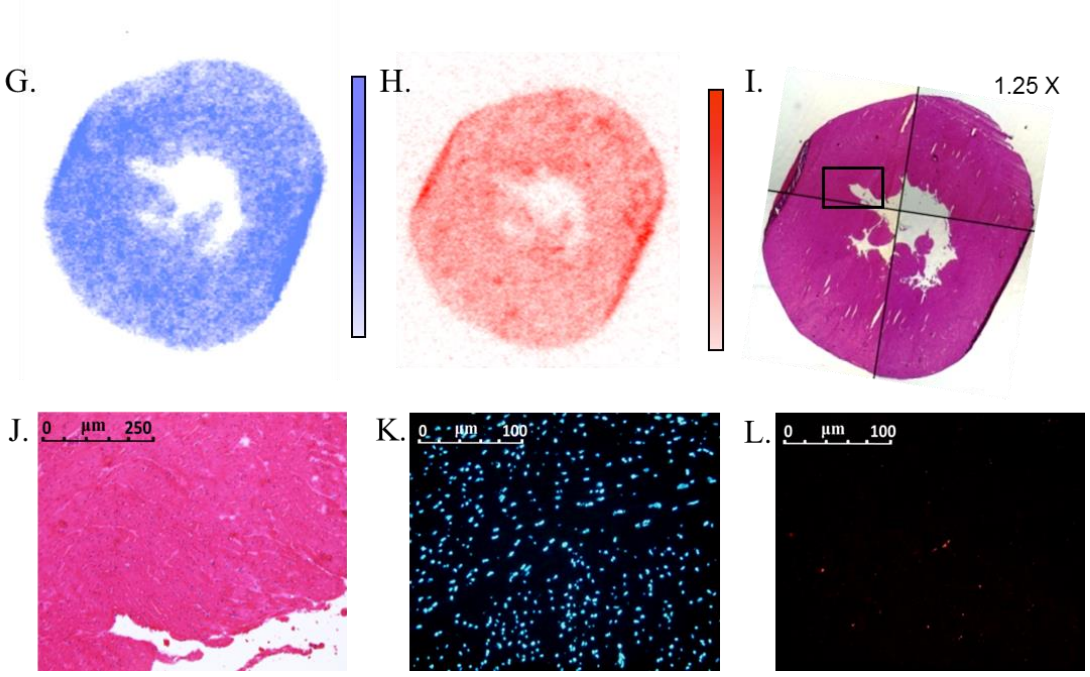

(**G**) Autoradiograms from a control rat (d21) with ^{99m}Tc-tetrofosmin and (**H**) ^{67}Ga-citrate. (**I** and **J** (magnification)) HE-staining of the same heart-section. (**K**) Corresponding nuclear staining (Hoechst). (**L**) Anti-CD68-staining showing only some single (physiologic) macrophages.

4.5.2. ^{68}Gallium (^{68}Ga DOTA-TATE)

Since ^{67}Ga-citrate is considered a non-specific tracer for inflammation, to more specifically detect myocardial cell-infiltrates we assayed ^{68}Ga DOTA-TATE, having a high affinity for SSTR-2A, a somatostatin-receptor subtype known to be up-regulated in the membranes of activated macrophages. Indeed, immunized animals revealed a high uptake of ^{68}Ga-DOTATATE in cardiac areas exhibiting massive cell-infiltrates (i.e., in the right ventricular wall and adjacent septum, **Fig.15A**, arrows), as demonstrated by HE-stains of corresponding heart-sections (**Figs. 15B and C [insert]**), whereas no relevant ^{68}Ga-DOTATATE-uptake was observed in control-rats (**Fig. 9H**) devoid of myocardial infiltrates, as confirmed by HE-staining (**Figs. 15I and J [insert]**). To characterize the type of cells present in DOTATATE-positive vs. -negative myocardial areas (**Figs. 15A vs. H**), after staining of the cell-nuclei (**Hoechst; Figs. 15D and K**) we performed parallel immuno-histo-chemical staining with anti-CD68-abs (**Figs. 15E and L**), and with anti-SSTR2A-abs (**Figs. 15F and M**). Co-localization of the signals underscored that the large majority of cells in DOTATATE-positive infiltrates were, indeed, macrophages (**Figs. 15G vs. N [control]**).

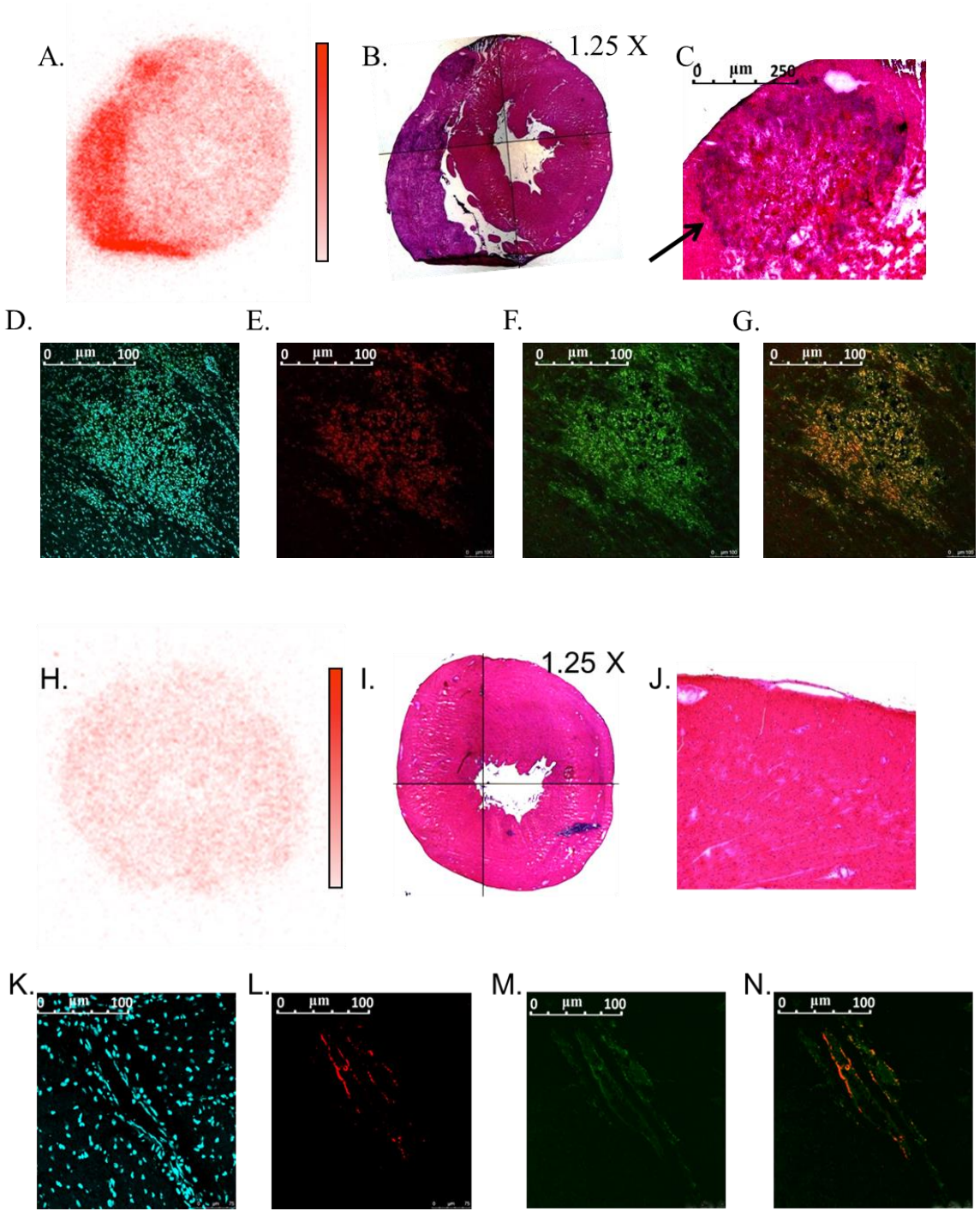

Figure 15: Detection of the somatostatin receptor type 2 (sstr-2) by ^{68}Ga DOTA-TATE as a surrogate for myocardial inflammation and comparison with histology.
A to **G**: (A) Representative autoradiogram from a myosin-immunized rat (d21) using ^{68}Ga DOTA-TATE as a tracer for inflammation. (B) HE-staining of the same heart section, (C) and magnification (arrow) of a myocardial area either stained with Hoechst (D, nuclear stain) or (E) analyzed by immunofluorescence using anti-CD68 to detect macrophages or anti-rat sstr-2 to detect somatostatin receptors expressed on infiltrating macrophages (F; co-localization G).
H to **N**: (H) Representative autoradiogram from a 0.9% NaCl-injected control animal using ^{68}Ga DOTA-TATE and the corresponding HE-staining (I; magnification J) , the nuclear staining (K, Hoechst), and the corresponding anti-CD68 (L) or anti-rat sstr-2 (M; co-localization N) immunofluorescent stainings revealed considerably fewer signs of inflammation compared to the immunized rat.

4.5.3. ^{68}Gallium (^{68}Ga NOTA-RGD)

The nuclear tracer ^{68}Gallium linked to the tri-peptide RGD (^{68}Ga NOTA-RGD) has a high affinity for alpha v beta integrin receptors. Alpha v beta integrin receptors are considered as a marker which binds to the beta 3 integrins expressed on the surface of endothelial cells. Autoradiograms from EAM-rats revealed focal accumulation of ^{68}Ga NOTA-RGD within the left ventricle (**Fig. 16A**). MGT-staining of the same heart section revealed myocyte-necrosis in the same region (**Fig. 16B and C[insert]**). This region has only few cellular infiltrates and shows no collagen deposition which would correspond to the late inflammatory state. However, around the same (necrotic) region, a strong staining for β3 integrin receptor s (**Fig. 16E , D-Hoechst**) was obtained together with a strong signals for PECAM-1 (Platelet endothelial cell adhesion molecule) indicating the presence of endothelial progenitor cells (**Fig. 16F**); both are thought to be involved in neo-vascularization (**merge, Fig. 16G**).

Since neovascularization might represent a pre-requisite for fibrosis development and scar formation, ^{68}Ga NOTA- RGD appears to accumulate preferentially in areas with post-inflammatory repair. Control hearts did not show any cellular infiltrates where relevant tracer-signals were detected (**Fig. 16H**). Control heart sections were also negative for anti-CD 61and anti-CD31 stainings (**Fig. 16L and 16M**).

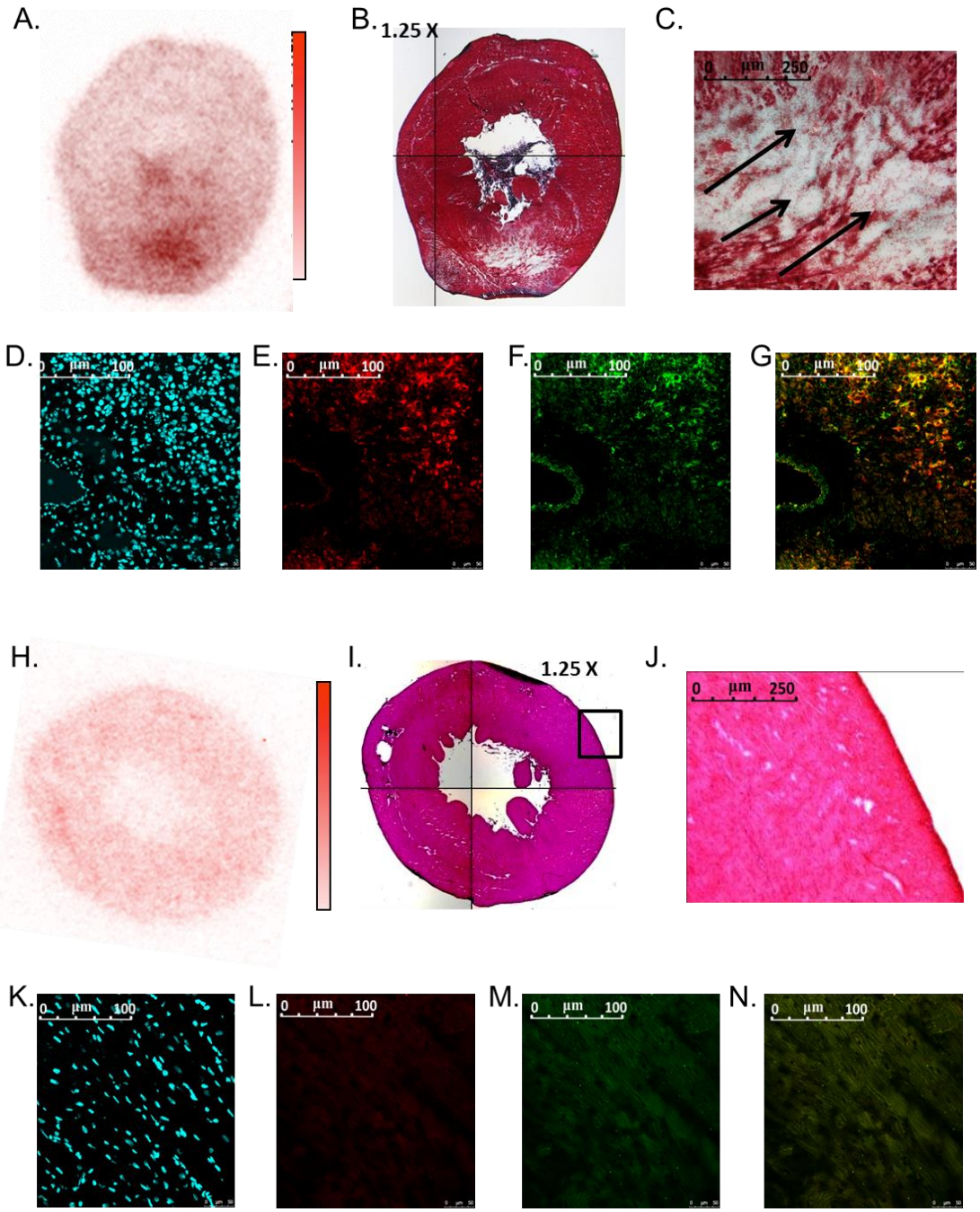

Figure 16: Detection of the αvβ3 integrin receptor by ^{68}Ga NOTA-RGD as a surrogate for neoangiogenesis and comparison with histology.

A to **F**: (A) Representative autoradiogram from a myosin-immunized rat (d21) using ^{68}Ga NOTA-RGD as a tracer for angiogenesis. (B) MGT-stain of the same heart section and (C) magnification of altered (necrotic) myocardium with surrounding cellular infiltrates (arrows D); nuclear staining (Hoechst, E). Immuno-fluorescent staining of β3 integrin receptors in the same myocardial area using anti-rat integrin β_3 (= anti-CD61). (F) Increased vascular density in the same area revealed by anti-rat CD31/PECAM I. (G) Co-localization of CD31 and CD61.

(H) Representative autoradiogram from a 0.9% NaCl-injected control animal using ^{68}Ga NOTA-RGD, as well as the corresponding HE-stains (I, detail J). (K) Nuclear staining/ (Hoechst) (L) anti-rat integrin β_3 (= anti-CD61) and (M) anti-rat PECAM-1 Immunofluorescence (anti-rat CD31), and (N) co-localization of CD31 and CD61.

"Science is not about making predictions or performing experiments. Science is about explaining."

-Bill Gaede

Discussion

5.1 Myocarditis phenotypes in humans and in animal models

Acute myocarditis is one of the main causes of sudden cardiac death in younger adults, and in about 30% of the cases may result in adverse post-inflammation remodeling and severe HF; however, reliable non-invasive tools for the detection of myocardial inflammation are still lacking (16). There is a high clinical need for such tools because both the symptoms and the underlying cause of acute myocarditis may vary widely (36). Various animal models for myocarditis have been established in past but, compared to the human situation, many of them suffer from inconsistent or inappropriate features, particularly regarding the progression from acute to chronic myocarditis (141). However, in Lewis rats (as in human patients) there seems to be an initial "asymptomatic" phase when myocardial inflammation develops but symptoms of cardiac involvement are not yet evident. Second, in human myocarditis cellular infiltrates predominantly expand from the lateral wall towards the septum (142); a similar pattern of infiltration was observed in the large majority of our Lewis rats. Third, not all immunized rats that developed anti-myosin-abs also developed fulminant myocarditis; instead, many of our EAM-rats suffered from a kind of "smoldering inflammation" with a rather long healing period accompanied by replacement fibrosis, similar to the assumed pathogenesis of post-inflammatory DCM in humans (143). During this late (chronic) post-inflammatory phase none of our EAM-rats died, whereas in case of a fulminant reaction-pattern we lost ~23% (n=17/74) of our rats because of rapidly progressing HF and/or sudden cardiac death. Thus, the here presented Lewis rat-model seems to adequately mimic many features of human myocarditis (144).

5.2 Induction EAM in the Lewis rat to detect cellular infiltrates

In our experiments, significant anti-cardiac myosin antibody titers were obtained and target specificity was confirmed by immunoblotting. We believe that in our case antibody production significantly contributed to the desired inflammatory phenotype (145). Some recent reports suggest that anti-myosin antibodies are associated with left ventricular systolic dysfunction and diastolic stiffness in patients with chronic myocarditis (18). In our experiments we followed cardiac function by echocardiography and MRI to assess secondary signs of inflammation without sacrificing the animal. We did not find any relevant decrease of LV systolic function but consistently found myocardial thickening with regional wall motion abnormalities and pericardial effusion in immunized animals, starting from day 19 onwards after the initial immunization. Kodama *et.al* have reported the presence of pericardial effusion in immunized rats on the 21st and 28th day of immunization along with enlarged hearts (146), which is in agreement with our findings.

To determine the optimal time-point for testing our non-invasive imaging strategies, the kinetics of the disease was investigated on a histomorphological basis. Apparent macrophage infiltration started only after 14 days of immunization. From day 14 to day 40 cellular infiltrates were constantly present peaking around day 28, fibrosis started from day 14 on and increased constantly. From day 45 onwards no further increases in fibrosis development were seen. Consistent with previous reports on an EAM models, about 70 % of

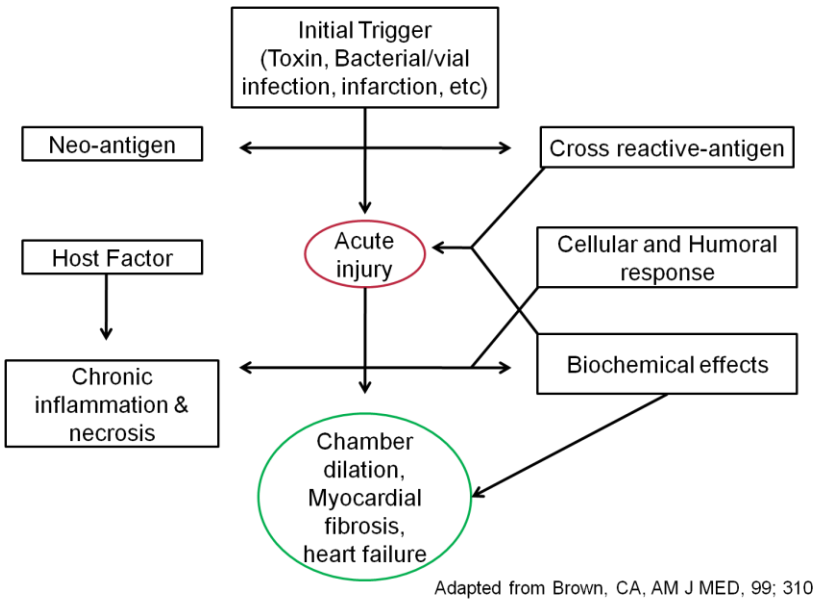

Scheme 9: Schematic representation of the assumed pathomechanisms in inflammatory heart disease.

the cells infiltrating the myocardium were macrophages. Some focal lesions had even reported macrophage-numbers higher than 70 % (147,148), which fully fits to our findings. In the present model, macrophages accomplish diverse functions, such as non-specific scavenging of cell debris/necrotic/apoptotic myocytes, cellular matrix or acting as antigen presenting cells (**see scheme 8**) (149). In previous reports, the time course of inflammation and fibrosis development has been derived theoretically and extensively speculated (150). In our study, we histomorphologically assessed and clearly demonstrate the kinetics of macrophage infiltration and collagen deposition in the acute phase and in the chronic phase of myocarditis (**see scheme 9**).

5.3 Molecular findings in the Lewis EAM model

As a pre-condition for testing novel (non-invasive) detection strategies for myocarditis, in our rat-hearts we closely monitored the development of cellular infiltrates and fibrosis both on a histological and on a molecular basis. Our results indicate that upon EAM-induction Lewis rats develop two different modes of reaction: One reaction-pattern is characterized by a short fulminant inflammatory phase, rapid clearance of cellular infiltrates, and an early development of replacement-fibrosis; such animals appear more prone to rapid post-inflammation remodeling and, depending on the amount of damaged myocardium (**!**), either (small damage) early recovery or (large damage) rapidly progressive cardiac dysfunction and severe HF. The other reaction-pattern is characterized by a less fulminant but prolonged acute inflammatory phase, resembling chronic "smoldering myocarditis" with a higher risk for chronic HF and/or severe cardiac arrhythmias in later stages of the disease.

A recent clinical study following patients with or without a fulminant course of acute myocarditis (5.6 years of follow-up) revealed that more than 90% of the patients with a fulminant course of the disease were still alive compared to only 45% of those with a less fulminant but more prolonged phase of "smoldering inflammation" (151) . It should be noted, however, that patients with a fulminant course who did not rapidly recover had a higher risk of developing acute HF and sudden cardiac death, which is in line with our rat-model. The here unraveled differential cardiac expression of selected pro-inflammatory/pro-fibrotic *versus* fibrosis markers/cytokines in the acute *vs.* chronic phase of myocarditis (**Figs. 3M and L**) might provide a key for the understanding of this bivalent behavior. With the assessment of such markers, future clinical studies might contribute a (bench-) basis for the (bedside-) timing and

indication of, e.g., cytokine-inhibitors or -modifiers as novel therapeutic approaches in acute myocarditis.

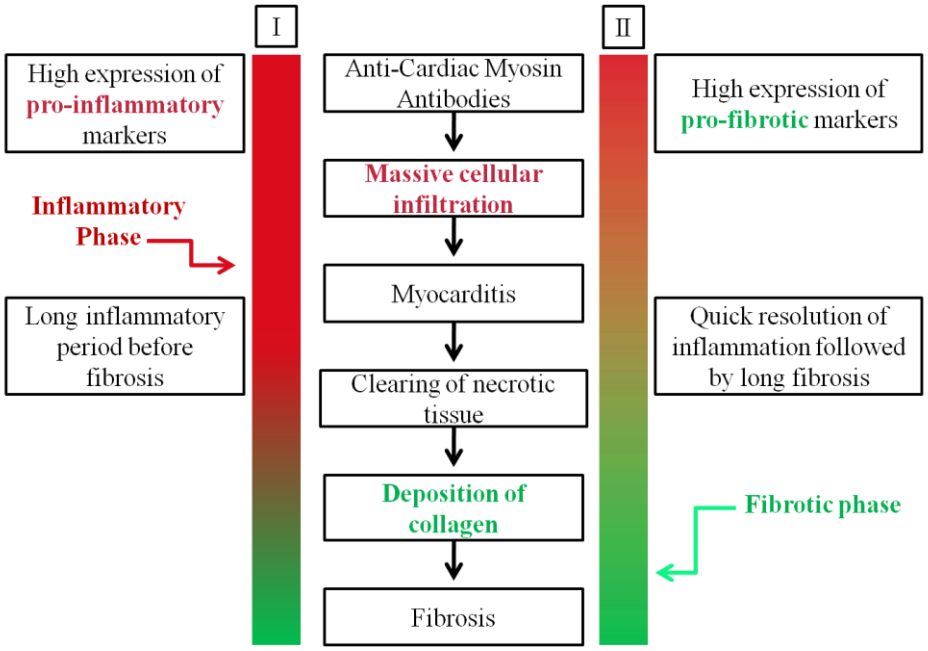

Scheme10: Schematic representation of molecular and histological findings in our EAM animal model.

In our Lewis model, the acute phase of myocarditis closely resembles that of the giant cell myocarditis, which is a rare but potentially fatal condition in humans. The chronic phenotype exhibits extensive myocardial fibrosis, as well as hypertrophic and atrophic changes of myocardial fibers resembling human dilated cardiomyopathy.

5.4 Non-invasive detection of cardiac inflammation

Reliable tools for the imaging of acute myocarditis along with tools facilitating imaging-guided biopsies (to histologically confirm and/or to identify the causative microbial agent) remain an unmet clinical need (152). With current diagnostic methods it appears almost impossible to capture the onset of myocarditis; even with clinically suspected myocarditis in the large majority of patients the diagnosis was confirmed only post-mortem or after development of severe congestive HF (17). An early and reliable diagnosis (and monitoring) of myocarditis would significantly change in hospital patient-management; in addition, it might facilitate clinical decisions on therapeutic interventions reducing inflammatory burden and/or preventing progression to CHF.

5.4.1. *In vivo* detection of myocardial inflammation by using USPIOs (Feraheme®)

MRI is an excellent imaging modality for clinical applications. When appropriate contrast agents are used, cellular infiltration, migration, and other biological processes can be monitored (153). The ability to non-invasively track cells *in vivo* can lead to a better understanding of the complex immune-mechanisms involved in acute and chronic myocarditis (154). In our study, we employed two iron-oxide based contrast agents; 1) USPIO (Feraheme®) and 2) MPIO to label and track cells *in vivo* by MRI.

The *in vivo* cell labeling efficiency by direct intravenous injection of iron-oxide based contrast agents is low because of particle dilution and accessibility (155). In the case of ultra-small particles, such as USPIO's, cells must ingest thousands of particles to create a local magnetic field gradient that is detectable by T2*-weighted MRI, especially at the level of a single cell (156). As per our data immunized rats injected with Feraheme® were measured after application of different doses as well as after different time intervals post injection. Unfortunately the respective MRI-Scans did not show a good correlation with our histological and immuno-histochemical findings. To confirm our negative MRI-findings, cardiac sections of the respective hearts were subjected to Pearl's Prussian blue staining and analyzed for the presence of iron deposits. Pearl's prussian blue staining is highly sensitive and can detect a rather small amount of iron (0.2 picogram) (157). Myocardium analyzed 24 to 48 hours after injection of 15 mg and 20 mg/kg body weight Feraheme® did not show any deposits of iron in the tissue. In fact, the ratio of iron containing cells as compared to the number of infiltrating cells seems to be very low. Blood smears from the animals after sacrifice were also checked for the presence of iron containing monocytes. The graph shown in **Figure 9G** depicts the percentage of monocytes positive for Feraheme® from the whole population of circulating monocytes (which in our immunized animals comprised only 4-6% of the immune-cells), which endorses our findings.

In a recent report by Yilmaz. A *et al*., Feraheme® was shown to be capable of detecting cellular infiltrates post myocardial infarction and was found to be safer and superior to gadolinium-based contrast agents (158,159). Our present histologically validated findings do not support the data reported for human patients. This could be due to different reasons; first, the time course of cellular infiltration between myocarditis and myocardial infarction differs to some extent. Second, the recruitment of inflammatory cells and initiation of the inflammatory process largely differs between humans and rats. Thus, a direct comparison of

Feraheme®-uptake between patients and Lewis rats at the present stage appears to not be meaningful; nevertheless, the usefulness of Feraheme® as a contrast agent for myocarditis should be critically revised.

5.4.2. *In vivo* & *In vitro* detection of myocardial inflammation by using MPIOs

The size of an MPIO particle is approximately 0.93 microns. Thus, each MPIO can contain picogram quantities of iron, and therefore cells containing one or only a few MPIO particles are sufficient for MRI detection (160). Electron microscopy studies have demonstrated that macrophages concentrate MPIOs in membrane-bound vesicles (108). Because of its superparamagnetic iron center a labelled macrophage can propagate a magnetic field gradient as much as 50 times its radius, allowing for a detection of individual cells. It has also been reported that single iron oxide–labeled cells can be detected at 1.5 T, and thus a clinical translation of cellular tracking studies with appropriate conditions should be possible (161).

In the present study, cells were tracked in a rat model of EAM by *in vitro* (MR microscopy) and *in vivo* MRI (7T) after a single intravenous injection of MPIOs to the recipient rat 24 hours before measurements. As per many previous reports in rats, the blood half-life of 0.93 micron MPIOs is short (<2 minutes), suggesting that MPIOs are rapidly taken up by the reticulo-endothelial system, including macrophages (162). Thus, no free MPIOs should have been present in the blood at the time of the scans and/or excision of hearts. This hypothesis is consistent with previous studies of MPIO-labeled cells in an acute rejection model (155). *Ex vivo* cellular labeling studies and our FACS data indicate that macrophages phagocytose or endocytose the MPIO particles better than other cell types (such as B cells and T cells) and, thus, our *in vivo* labeling strategy appears likely selective for macrophages. Although we cannot rule out ‘non-macrophage’ labeling, our histological findings from Prussian blue (iron) staining of both cardiac tissues and CD68 (rat-ED1)-positive cells (macrophages) further support our assumption. In addition, previous data indicate that the 0.93 micron MPIO particles neither affect cell function nor cell proliferation, and that there is no evidence for any long-term toxic effects on the organism. Thus our present data clearly indicate that MPIOs are suitable for *in vivo* macrophage labeling and cell-tracking studies by MRI.

5.4.3. *In vitro* detection of myocardial inflammation by using radioactive nuclear tracers.

After testing iron-oxide based contrast agents in the EAM model, we employed radioactive nuclear tracers (suitable for PET imaging) in order to detect myocardial inflammation. In our first nuclear tracer-based approach, we used ^{67}Ga-citrate and ^{99m}Technetium TF to image inflammatory exudates and, in parallel, myocardial perfusion. ^{67}Ga is considered an excellent imaging agent for chronic inflammation and has been routinely used to diagnose such conditions (118,119). O'Connell *et al*. compared ^{67}Ga scintigraphy with EMB in 68 DCM patients. Only 8 % of the study population had histologic evidence of myocarditis; 87 % of these patients had a positive for ^{67}Ga-scan (163). Only 1.8 % ^{67}Ga of negative patients had histological evidence for acute myocarditis. Matsura *et al.* diagnosed myocarditis in 46 consecutive children in the acute phase of Kawasaki disease by ^{67}Ga imaging (164). Our findings imply that ^{67}Ga seems to accumulate in inflammatory lesions where cardiomyocyte function is hampered. The loss of fully functional myocytes was confirmed by ^{99m}TechnetiumTF scans in same areas. The comparison of autoradiograms with histology confirmed that regions with high cellular infiltrates also accumulated ^{67}Ga. No uptake of ^{67}Ga or regular perfusion was found in remote areas or in healthy myocardium. The half-life of ^{67}Ga is rather long (ca. 12 hours), thus the clinical limitations of ^{67}Ga are non-specificity and a prolonged exposure pf the patients to radiation.

In our second approach, we used ^{68}Ga DOTA-TATE to image macrophages, which represent a major subset of cells invading the myocardium during inflammation. ^{68}Ga DOTA-TATE is routinely used in clinics for the detection of neuro-endocrine tumors (NET) (165). In a recent study, Li *et al.* compared n=16 consecutive patients with NET or thyroid cancer, who underwent both ^{68}Ga-DOTA-TATE and ^{18}F-FDG PET/CT for staging or restaging purposes. They reported a high uptake of ^{68}Ga DOTA-TATE in inflammatory lesions in large arteries of the examined cancer patients, which appeared to be associated with plaque burden, hypertension and history of cardiovascular disease in the respective patients (166,167). Our experiments' suggest that macrophages infiltrating the myocardium of immunized animals express high levels of sstr2, which would explain the accumulation of ^{68}Ga DOTA-TATE in the inflamed myocardial areas. ^{68}Ga DOTA-TATE was cleared from the healthy myocardium within 1 hour, whereas inflamed myocardium showed prolonged retention.

In our third approach, we employed ^{68}Ga NOTA-RGD to image the late inflammatory phase. RGD linked nuclear tracers have been tested in many pre-clinical models for their

specificity and sensitivity in the detection of angiogenesis after myocardial infarction (130). To some extent, the healing processes of acute myocarditis can be compared with the healing processes occurring after myocardial infarction (131). Higuchi et al. studied RGD-uptake after myocardial ischemia in 21 rats at different time points after coronary occlusion. In the latter study an accumulation of this tracer was noted up to 6 months after coronary occlusion, suggesting a prolonged response to post-infarction inflammation and a delay in repair processes. Our experiments indicate that the observed increased uptake of ^{68}Ga NOTA-RGD is due to its binding to extracellular matrix components in the boarder-region of inflammatory lesions. Histological analysis of corresponding tissue sections revealed a substantial loss of cardiomyocytes (apoptosis/necrosis) in the same regions. Most notable, cells expressing β3 integrin co-localized with endothelial progenitor cells in the boarder-regions of inflammatory lesions. ^{68}Ga has a relatively short half-life of ~1 hour as compared to ^{67}Ga, which prevents unnecessary radioactive exposure in a clinical context, and due to its specificity in the future might allow for a detection of acute myocarditis also in human patients.

5.5 Outlook and future perspective

Molecular imaging with radioactive nuclear tracers suffers from the major drawback of radiation exposure, which limits the usage and establishment of this technique in many clinical organizations. Thus, MRI cell-tracking using targeted contrast agents holds promise to offer solutions for various problems regarding the optimum timing of administration as well as cell location and cell viability over time. MRI is well suited as an imaging modality for non-invasive cell-tracking because of its good tissue characterization, excellent image quality, and high spatial resolution, although presently nuclear imaging appears to be more sensitive (98). In addition to the existing base equipment, MRI benefits from the lack of ionizing radiation, high spatial resolution, a flexible image contrast and the ability to assess regional function, perfusion, and necrosis. The translation of this technique is favorable for clinical practice in as far as the availability and use of high field (3 T) clinical scanners has increased, which might increase sensitivity for labeled cell detection. New ways of modifying existing agents, the use of MPIOs, and new contrast agents for MRI might help to overcome the limitations of MRI. With further research and development, using these novel agents to track cells in the frame of clinical trials will probably be realized.

5.6 Limitations

There are a few limitations to our study. First, the preclinical model which we employed in this study resembles fulminant myocarditis rather than viral myocarditis. Thus, the clinical translatability of the utilized nuclear tracers needs further investigation in a model of viral myocarditis. However, pericardial effusion and CD68-positive cells have been reported to be present in human myocarditis as shown in our EAM model. Second, autoradiograms gave best results in the setting of EAM rats with a moderate to high inflammatory response whereas it failed to detect mild inflammation both visually and quantitively; however, focal inflammatory spots could be convincingly detected. In contrast, our MRI experiments with MPIO's offered satisfactory results, but more studies and customization is required to perform human studies in the future.

5.7 Conclusion and perspectives

In conclusion, imaging of acute myocarditis with nuclear methods and, in particular, the use of a SSTR-2A-specific nuclear tracer ^{68}Ga DOTA-TATE and the further development of MRI cell tracking with targeted contrast agents (particularly MPIO's) might allow for either robust non-invasive PET/or MRI-imaging of moderate-to-high myocardial inflammation including a spatial mapping and follow-up of cell-infiltrates thereby opening the doors for a non-invasive assessment of the efficacy of novel anti-inflammatory therapeutic strategies.

A. List of Chemicals

Chemical	Catalogue ID	Supplier
2-Propanol (Isopropanol)	6752.4	Roth
Acetic aci d (glacial)	7332.2	Roth
Acetonitrile	AE70.2	Roth
Ammonia CP	A17.1	Roth
Ammonium carbonate	9832	Fluka
Ammonium peroxodisulfate	9913	Fluka
Ammonium sulfate	9318.1	Roth
Ampicillin ((sodium salt)	K029.2	Roth
Barium Chloride	11760	Fluka
Cardiomyosin (whole protein-porcine)	M0531	Sigma
Chloramphenicol	3886.3	Roth
Chymotrypsin	C4129	Sigma-Aldrich
Coomassie Brilliant Blue R25	3862.2	Roth
Dithiothreitol	6908.4	Roth
Ethanol (absolute)	9065.2	Roth
Ethanol (denatured)	K928.4	Roth
Formic acid	399388	Sigma-Aldrich
Glycerol	A3552	AppliChem
Guanidinium chloride	0037.1	Roth
Hydrochloric acid	4623.2	Roth
Hydrogen peroxide	8070.4	Roth
Imidazole	3899.4	Roth
Iodo acetic acid	I6806	Sigma-Aldrich
L-Glutathione (oxidized)	G4376	Sigma-Aldrich
L-Glutathione (reduced)	A2084	AppliChem
Magnesium chloride	HN03.3	Roth
MES	69892	Sigma-Aldrich
Methanol	4627.5	Roth
Nickel sulfate	T111.1	Roth
Nuclear-fast red	G13190	Sigma
Papain	8933.1	Roth
Phenylmethylsulfonyl fluoride	6367.2	Roth
Poly ethylene glycol 10	81280	Fluka
Poly ethylene glycol 3	81227	Fluka
Poly ethylene glycol 400	81350	Fluka
Poly ethylene glycol 5 monomethyl ether	81323	Sigma-Aldrich
Potassium chloride	HN02.3	Roth
Potassium hexacynoferrate (III)	60300	Fluka
Potassium hydroxide	6751	Roth
Potassium phosphate dibasic	P749.3	Roth
Potassium phosphate monobasic	P9791	Sigma-Aldrich
Potassium phosphate tribasic	60494	Fluka
Riboflavin	R7649	Sigma-Aldrich

Sodium acetate	3580.1	Roth
Sodium azide	K305.1	Roth
Sodium chloride	3957.2	Roth
Sodium dodecylsulfate	2326.2	Roth
Sodium hydroxide	6771.1	Roth
Trichloroacetic acid	91228	Fluka
Trifluoroacetic acid	302031	Sigma-Aldrich
TRIS (2-Amino-2-hydroxymethyl-propane-1,3-diol)	4855.3	Roth
Tris(2-carboxyethyl)phosphine	HN95.2	Roth
Trypsin	T1426	Sigma-ALdrich
Urea	2317.2	Roth

B. List of Buffers

Buffer	Composition
Phosphate buffered saline (10x)	1.3689 M NaCl + 26.8 mM KCl + 101.4 mM Na2HPO4 + 17.6 mM KH2PO4, pH 7.2
Coating buffers (ELISA)	a.) 0.2 M Sodium phosphate, pH 6.5 b.) 0.1 M Sodium carbonate, pH 9.5
Lysis buffer	0.1% Triton-X-100 in PBS
Blocking solution (ELISA)	3% w/v milk powder 1x PBS 0.1% v/v tween in 1x PBS
Blocking solution (Western Blot)	3% w/v milk powder + 2% Normal Goat Serum 1x PBS 0.1% v/v tween in 1x PBS
Blocking Solution (Immunostaining)	2% BSA + 2% NGS 1x PBS 0.1% v/v tween in 1x PBS
Antibody Diluent (Immunostaining)	2% BSA + 1% NGS 1x PBS 0.1% v/v tween in 1x PBS
Bovine Serum Albumine (BSA)	4% in 1x PBS (w/v)

C. List of Instruments

Type	Model	Supplier
Ice machine	MF-300	Scotsman
Vortex machine	VTX3000L	LMS systems
Incubator	ME66400	LMS systems
Laminar Hood	98KLP	BDK
Magnetic stirrer	ST-441, 442, 443, 444, 445	SPI Supplies
Microscope	4000D	Leica
Microscope: Camera	Olympus	Olympus
Microscope: Computer interface	Division	Leica
PCR Cycler	IQ-223	Biorad
pH-electrode BlueLine	A7-8897	Beckman Coulter
Pipettes	R-1000, R-500, R-200, R-20	Rannin
Pippetboy	LK-100	Accujet
Water Bath	WB-2000K	DFL
Elisa Reader	SpectraMax 350	Molecular Devices
Spectrophotometer	Spec Plus	Biorad
Tissue Lyser	1000-Q	Qiagen
Mini-Centrifuge	ME6400	LMS systems
Centrifuge	Rotina 48R	Hettich
Microtome	CM3050 R	Lecia
Cryotome	MT4000 T	Lecia
Flowcytometer	FACSAria III	Becton Dikinson
Autoclave	Systec V-150	Systec
Balance	0.5-500 g XS 6002S Dual Range Mettler	Toledo
Balance	0-1g XS 105 Dual Range Mettler	Toledo
CD-Spectropolarimeter	J-810	Jasco
Cell Disruptor	M-110P E615	Microfluidics
Incubator	JO 1198	MNC-Heating System
Centrifuge	0-1000 ml Avanti J-26 XP	Beckmann Coulter
Centrifuge	0-2 ml 5417 R	Eppendorf
Centrifuge	0-5 ml 5810 R	Eppendorf
Spectrophotometer	Dynapro Titan	Wyatt Technology

D. List of Primers

#	Name	Sequence	Usage
1	IL6-RAT-FP	AAGCCAGAGTCATTCAGAGCA	Proinflammatory cytokine
2	IL6-RAT-RP	AGGAGAGCATTGGAAGTTGG	Proinflammatory cytokine
3	IL17-RAT-FP	ACTTTCCGGGTGGAGAAGAT	Proinflammatory cytokine
4	IL17-RAT-RP	TGGCGGACAATAGAGGAAAC	Proinflammatory cytokine
5	OPN-RAT-FP	AAGGCGCATTACAGCAAACAG	Proinflammatory cytokine
6	OPN-RAT-RP	CTCATCGGACTCCTGGCTCTT	Proinflammatory cytokine
7	IL1beta-RAT-FP	AAATGCCTCGTGCTGTCTGC	Proinflammatory cytokine
8	IL1beta-RAT-RP	TCGTTGCTTGTCTCTCCTTG	Proinflammatory cytokine
9	TNFa-RAT-FP	GCTCCCTCTCATCAGTTCCA	Proinflammatory cytokine
10	TNFa-RAT-RP	CTCCTCCGCTTGGTGGTTAA	Proinflammatory cytokine
11	INFg-RAT-FP	CACGCCGCGTCTTGGTCCTG	Proinflammatory cytokine
12	INFg-RAT-RP	TCTAGGCTTTCAATGAGTGT	Proinflammatory cytokine
13	IL23A-RAT-FP	ACACACACCAGTGGGACAAA	Proinflammatory cytokine
14	IL23A-RAT-RP	ACAACCATCACCACACTGGA	Proinflammatory cytokine
15	TGFb1-RAT-FP	GAGAGCCCTGGATACCAACT	Proinflammatory cytokine
16	TGFb1-RAT-RP	CAACCCAGGTCCTTCCTAAA	Proinflammatory cytokine
17	COL 1-RAT-FP	ATCCTGCCGATGTCGCTAT	Profibrotic cytokine
18	COL 1-RAT-RP	CCACAAGCGTGCTGTAGGT	Profibrotic cytokine
19	COL 3-RAT-FP	CTGGTCCTGTTGGTCCATCT	Profibrotic cytokine
20	COL 3-RAT-RP	ACCTTTGTCACCTCGTGGAC	Profibrotic cytokine
21	LOX2-RAT-FP	GCTGATCCAGTGGGAGAACAA	Profibrotic cytokine
22	LOX2-RAT-RP	AGCACCCGGGAGCTACTCT	Profibrotic cytokine
23	MMP1-RAT-FP	CCCCTATCTACACCTACACCAA	Profibrotic cytokine
24	MMP1-RAT-RP	CATTCCAGGAGTCTGCGATGAA	Profibrotic cytokine
25	MMP9-RAT-FP	TCGAAGGCG ACCTCAAGTG	Profibrotic cytokine
26	MMP9-RAT-RP	TTCGGTGTAGCTT TGGATCCA	Profibrotic cytokine
27	MMP14-RAT-FP	TAGGCATAGGGCACTTCTCG	Profibrotic cytokine
28	MMP14-RAT-RP	GCAGGGAAGGGGCTAATGAA	Profibrotic cytokine
29	TIMP1-RAT-FP	TCTGGCATCCTCTTGTTGCT	Profibrotic cytokine
30	TIMP1-RAT-RP	CACAGCCAGCACTATAGGTC	Profibrotic cytokine
31	TIMP3-RAT-FP	GCCTCAATTACCGCTACCAC	Profibrotic cytokine
32	TIMP3-RAT-RP	TGTCGGTCCAGAGACATTCA	Profibrotic cytokine
33	GAPDH-RAT-FP	CTCCCTCAAGATTGTCAGC	Hoose-keeping gene
34	GAPDH-RAT-RP	TGATGGCATGGACTGTGG	Hoose-keeping gene
35	Nppa-RAT-FP	GGGTAGGATTGACAGGATTGG	Hoose-keeping gene
36	Nppa-RAT-RP	TCGAGCAGATTTGGCTGTTAA	Hoose-keeping gene

References

1. Ambrosy AP, Fonarow GC, Butler J, et al. The Global Health and Economic Burden of Hospitalizations for Heart FailureLessons Learned From Hospitalized Heart Failure Registries. J Am Coll Cardiol. 2014;63:1123-33.
2. Caforio AL, Bauce B, Boffa GM, et al. Autoimmunity in myocarditis and dilated cardiomyopathy: cardiac autoantibody frequency and clinical correlates in a patient series from Italy. G Ital Cardiol. 1997;27:106-12.
3. Jahns, Roland, et al. "Pathogenic relevance of autoantibodies in dilated cardiomyopathy." Inflammatory Cardiomyopathy (DCMi). Birkhäuser Basel, 2010,18:157-170.
4. Jahns R, Boivin V, Schwarzbach V, Ertl G, Lohse MJ. Pathological autoantibodies in cardiomyopathy. Autoimmunity. 2008;41:454-61.
5. Jahns R, Deubner N, Boivin V, Caforio ALP, Felix SB, Fu M, Lohse MJ, Ertl G (2011): Acute myocarditis – a trigger of cardiac autoimmunity? Expected insights from the Etiology, Titre-Course, and (effect on) Survival of cardiac autoantibodies (ETiCS) Study. In: Myocarditis. Cihakova D. Ed., InTech open access publisher, Rijeka (Croatia); pp 100-17
6. Gaaloul I, Riabi S, Harrath R, et al. Sudden unexpected death related to enterovirus myocarditis: histopathology, immunohistochemistry and molecular pathology diagnosis at post-mortem. BMC Infect Dis. 2012;12:212-18.
7. Mason JW. Myocarditis and dilated cardiomyopathy: an inflammatory link. Cardiovasc Res. 2003;60:5-10.
8. Boivin-Jahns V, Schlipp A, Hartmann S, et al. Antibodies to cardiac receptors. Herz 2012;37:843-48.
9. Schultheiss, H. P. "[Acute viral myocarditis. 1: Pathogenesis, clinical manifestations, diagnosis]." Fortschritte der Medizin. 1991;109.3: 45-48..
10. Jahns R, Boivin V, Hein L, et al. Direct evidence for a beta1-adrenergic receptor directed autoimmune attack as a cause of idiopathic dilated cardiomyopathy. J. Clin. Invest. 2004;113:1419-29.
11. Störk, Stefan, et al. "Stimulating autoantibodies directed against the cardiac β 1-adrenergic receptor predict increased mortality in idiopathic cardiomyopathy." Am Heart J. 2006;152.4: 697-04
12. Limas CJ, Limas C. HLA-DR antigen linkage of anti-beta-receptor antibodies in idiopathic dilated and ischaemic cardiomyopathy. Br. Heart J. 1992;67:402-5.
13. Jahns, Roland, Valérie Boivin, and Martin J. Lohse. "Beta 1-adrenergic receptor-directed autoimmunity as a cause of dilated cardiomyopathy in rats." Int J of cardiol. 2006;112.1: 7-14.
14. Schwimmbeck PL, Bigalke B, Schulze K, Pauschinger M, Kühl U, Schultheiss HP. The humoral response in viral heart disease: characterization and pathophysiological significance of antibodies. Med. Microbiol. Immunol. 2004;193:115-19.
15. Maze S, Adolph R. Myocarditis: unresolved issues in diagnosis and treatment. Clinl Cardiol. 1990;13:69-79.
16. Caforio AL, Marcolongo R, Jahns R, Fu M, Felix SB, Iliceto S. Immune-mediated and autoimmune myocarditis: clinical presentation, diagnosis and management. Heart fail Rev. 2013;18:715-32.
17. Kindermann I, Barth C, Mahfoud F, et al. Update on myocarditis. J Am Coll Cardiol. 2012;59:779-92.
18. Elamm C, Fairweather D, Cooper LT. Pathogenesis and diagnosis of myocarditis. Heart 2012;98:835-40.
19. Olinde M, Kurt D, O'Connell M, John B. Inflammatory heart disease: pathogenesis, clinical manifestations, and treatment of myocarditis. Annu Rev Med 1994;45:481-90.
20. Skouri HN, Dec GW, Friedrich MG, Cooper LT. Noninvasive imaging in myocarditis. J Am Coll of Cardiol. 2006;48:2085-93.

21. Vaideeswar P, Cooper LT. Giant cell myocarditis: clinical and pathological features in an Indian population. Cardiovasc Pathol. 2013;22:70-4.
22. Cooper Jr L, ElAmm C. Giant cell myocarditis. Herz. 2012;37:632-36.
23. Huston B, Froloff V, Mills K, McGee M. Death Due to Eosinophilic Necrotizing Myocarditis Despite Steroid Treatment. Am J of Forens Med and Patho. 2013;34:95-7.
24. Hufnagel G, Pankuweit S, Richter A, Schönian U, Maisch B. The European Study of Epidemiology and Treatment of Cardiac Inflammatory Diseases (ESETCID) First Epidemiological Results. Herz.2000;25:279-85.
25. Maisch B. Spontaneous resolution of Myocarditis - Data from the placebo cohort of ESETCID. J Am Coll of Cardiol. 2012;59:E1551.
26. Shauer A, Gotsman I, Keren A, et al. acute viral myocarditis: current concepts in diagnosis and treatment. Isr Med Assoc J. 2013;15:180-5.
27. Mason JW. Techniques for right and left ventricular endomyocardial biopsy. Am J of Cardiol 1978;41:887-92.
28. Mason J, O'Connell J. Clinical merit of endomyocardial biopsy. Circulation. 1989;79:971-79.
29. Mason JW. Endomyocardial biopsy: the balance of success and failure. Circulation 1985;71:185-8.
30. Cooper LT, Baughman KL, Feldman AM, et al. The Role of Endomyocardial Biopsy in the Management of Cardiovascular DiseaseA Scientific Statement From the American Heart Association, the American College of Cardiology, and the European Society of Cardiology Endorsed by the Heart Failure Society of America and the Heart Failure Association of the European Society of Cardiology. J AmColl of Cardiolo2007;50:1914-31.
31. Pophal SG, Sigfusson G, Booth KL, et al. Complications of endomyocardial biopsy in children. J Am Coll Cardiol 1999;34:2105-10.
32. Przybojewski JZ. Endomyocardial Biopsy - a Review of the Literature. Catheterization and Cardiovas Diag. 1985;11:287-30.
33. Edwards, W. D., D. R. Holmes Jr, and G. S. Reeder. "Diagnosis of active lymphocytic myocarditis by endomyocardial biopsy: quantitative criteria for light microscopy." Mayo Clinic Proceedings. 1982;57:7-10.
34. American Heart Association. Heart Disease and Stroke Statistics 2005 Update. Dallas, TX: American Heart Association; 2005:167-79
35. Baughman KL. Diagnosis of myocarditis: death of Dallas criteria. Circulation 2006;113:593-5.
36. Chow LH, Radio SJ, Sears TD, Mcmanus BM. Insensitivity of right ventricular endomyocardial biopsy in the diagnosis of myocarditis. J Am Coll Cardiol 1989;14:915-20.
37. Yajima T, Knowlton KU. Viral Myocarditis From the Perspective of the Virus. Circulation 2009;119:2615-24.
38. Mahrholdt H, Goedecke C, Wagner A, et al. Cardiovascular magnetic resonance assessment of human myocarditis a comparison to histology and molecular pathology. Circulation 2004;109:1250-58.
39. Caforio AL, Calabrese F, Angelini A, et al. A prospective study of biopsy-proven myocarditis: prognostic relevance of clinical and aetiopathogenetic features at diagnosis. Eur Heart J 2007;28:1326-33.
40. de Leeuw N, Melchers WJ, Ruiter DJ, et al. Autoimmune markers are undetectable in end stage idiopathic dilated cardiomyopathy. J Clin Pathol 1999;52:739-43.
41. Smith SC. Autoimmune myocarditis. Curr Protoc Immunol. 2001; 15:14-15.
42. Li Y, Heuser JS, Kosanke SD, Hemric M, Cunningham MW. Cryptic epitope identified in rat and human cardiac myosin S2 region induces myocarditis in the Lewis rat. J Immunol 2004;172:3225-34.
43. Pummerer CL, Luze K, Grässl G, et al. Identification of cardiac myosin peptides capable of inducing autoimmune myocarditis in BALB/c mice. J Clin Inves. 1996;97:2057-59.
44. Nahrendorf M, Hiller K-H, Hu K, Ertl G, Haase A, Bauer W. Cardiac magnetic resonance imaging in small animal models of human heart failure. Med Image anal 2003;7:369-75.

45. Li Y, Agarwal P. A pathway-based view of human diseases and disease relationships. PLoS ONE 2009;4:43-46.
46. Kodama M, Zhang S, Hanawa H, Shibata A. Immunohistochemical characterization of infiltrating mononuclear cells in the rat heart with experimental autoimmune giant cell myocarditis. Clin Exp Immunol 1992;90:330-5.
47. Shioji K, Kishimoto C, Nakayama Y, Sasayama S. Strain difference in rats with experimental giant cell myocarditis. Jpn Circ J 2000;64:283-6.
48. Mascaro-Blanco A, Alvarez K, Yu X, et al. Consequences of unlocking the cardiac myosin molecule in human myocarditis and cardiomyopathies. Autoimmun 2008;41:442-53.
49. Matsumori A. Cytokines in myocarditis and cardiomyopathies. Curr Opin Cardiol 1996;11:302-9.
50. Caforio AL, Daliento L, Angelini A, et al. Autoimmune myocarditis and dilated cardiomyopathy: focus on cardiac autoantibodies. Lupus 2005;14:652-5.
51. Fairweather D, Kaya Z, Shellam GR, Lawson CM, Rose NR. From infection to autoimmunity. J Autoimmun 2001;16:175-86.
52. Fonseca J, Santos M, Canhao H, Choy E. Interleukin-6 as a key player in systemic inflammation and joint destruction. Autoimmun rev 2009;8:538-45.
53. Kanda T, McManus JEW, Nagai R, et al. Modification of viral myocarditis in mice by interleukin-6. Circ res 1996;78:848-56.
54. Choy E, Isenberg D, Garrood T, et al. Therapeutic benefit of blocking interleukin-6 activity with an anti–interleukin-6 receptor monoclonal antibody in rheumatoid arthritis: A randomized, double-blind, placebo-controlled, dose-escalation trial. Arthritis & Rheumatism 2002;46:3143-50.
55. Kanda T, Takahashi T. Interleukin-6 and cardiovascular diseases. Jpn Heart J 2004;45:183-93.
56. Poffenberger MC, Horwitz MS. IL-6 during viral-induced chronic autoimmune myocarditis. Ann N Y Acad Sci 2009;1173:318-25.
57. Matsumori A, Yamada T, Suzuki H, Matoba Y, Sasayama S. Increased circulating cytokines in patients with myocarditis and cardiomyopathy. Br Heart J 1994;72:561-6.
58. Huber SA, Polgar J, Schultheiss P, Schwimmbeck P. Augmentation of pathogenesis of coxsackievirus B3 infections in mice by exogenous administration of interleukin-1 and interleukin-2. J of virolo 1994;68:195-06.
59. Beyaert R, Kidd VJ, Cornelis S, et al. Cleavage of PITSLRE kinases by ICE/CASP-1 and CPP32/CASP-3 during apoptosis induced by tumor necrosis factor. Jof Biolo Chem 1997;272:11694-97.
60. Eriksson U, Kurrer MO, Sonderegger I, et al. Activation of dendritic cells through the interleukin 1 receptor 1 is critical for the induction of autoimmune myocarditis. J Exp Med 2003;197:323-31.
61. Dinarello CA. Interleukin-18. Methods 1999;19:121-32.
62. McInnes IB, Gracie JA, Leung BP, Wei X-Q, Liew FY. Interleukin 18: a pleiotropic participant in chronic inflammation. Immunolo rev 2000;21:312-15.
63. Dinarello CA, Novick D, Puren AJ, et al. Overview of interleukin-18: more than an interferon-gamma inducing factor. Jof leu biolo 1998;63:658-64.
64. Gluck B, Schmidtke M, Merkle I, Stelzner A, Gemsa D. Persistent expression of cytokines in the chronic stage of CVB3-induced myocarditis in NMRI mice. J Mol Cell Cardiol 2001;33:1615-26.
65. Levine MC, Klugman D, Teach SJ. Update on myocarditis in children. Curr Opin Pediatr 2010;22:278-83.
66. Veldhoen M, Hocking RJ, Flavell RA, Stockinger B. Signals mediated by transforming growth factor-β initiate autoimmune encephalomyelitis, but chronic inflammation is needed to sustain disease. Nat immunol 2006;7:1151-56.
67. Kumar A, Thota V, Dee L, Olson J, Uretz E, Parrillo JE. Tumor necrosis factor alpha and interleukin 1beta are responsible for in vitro myocardial cell depression induced by human septic shock serum. J of exp med 1996;183:949-58.

68. Coussens LM, Werb Z. Inflammation and cancer. Nat 2002;420:860-67.
69. Hotamisligil GS. Inflammation and metabolic disorders. Nat 2006;444:860-67.
70. Koss K, Satsangi J, Fanning G, Welsh K, Jewell D. Cytokine (TNF alpha, LT alpha and IL-10) polymorphisms in inflammatory bowel diseases and normal controls: differential effects on production and allele frequencies. Genes and immunity 2000;1:185-89.
71. Zhang J. Yin and yang interplay of IFN-γ in inflammation and autoimmune disease. J Clin Inves 2007;117:871-73.
72. Kasahara T, Hooks J, Dougherty S, Oppenheim J. Interleukin 2-mediated immune interferon (IFN-gamma) production by human T cells and T cell subsets. J of Immunol 1983;130:1784-89.
73. Szabo SJ, Sullivan BM, Stemmann C, Satoskar AR, Sleckman BP, Glimcher LH. Distinct effects of T-bet in TH1 lineage commitment and IFN-gamma production in CD4 and CD8 T cells. Sci Signal 2002;295:338-45.
74. Metcalf D, Di Rago L, Mifsud S, Hartley L, Alexander WS. The development of fatal myocarditis and polymyositis in mice heterozygous for IFN-gamma and lacking the SOCS-1 gene. Proc Natl Acad Sci 2000;97:9174-9.
75. Farrar MA, Schreiber RD. The molecular cell biology of interferon-gamma and its receptor. A rev of immunol 1993;11:571-611.
76. Afanasyeva M, Wang Y, Kaya Z, et al. Experimental autoimmune myocarditis in A/J mice is an interleukin-4-dependent disease with a Th2 phenotype. Am J of Pathol 2001;159:193-03.
77. Kramer JM, Gaffen SL. Interleukin-17: a new paradigm in inflammation, autoimmunity, and therapy. J Periodontol 2007;78:1083-93.
78. Andersson A, Isaksson M, Wefer J, et al. Impaired autoimmune T helper 17 cell responses following DNA vaccination against rat experimental autoimmune encephalomyelitis. PLoS ONE 2008;3:e3682.
79. Röhn TA, Jennings GT, Hernandez M, et al. Vaccination against IL-17 suppresses autoimmune arthritis and encephalomyelitis. Eur J Immunol 2006;36:2857-67.
80. Trinchieri G. Interleukin-12 and the regulation of innate resistance and adaptive immunity. Nat Rev Immunol 2003;3:133-46.
81. Abraham C, Cho J. Interleukin-23/Th17 pathways and inflammatory bowel disease. Inflamm bowel dis 2009;15:1090-1100.
82. Lawrence DA. Transforming growth factor-beta: a general review. Eur cytokine net 1996;7:363-68.
83. Schuster N, Krieglstein K. Mechanisms of TGF-β-mediated apoptosis. Cell tissue res 2002;307:1-14.
84. Santibanez JF, Quintanilla M, Bernabeu C. TGF-beta/TGF-beta receptor system and its role in physiological and pathological conditions. Clin sci 2011;121:233-51.
85. Denhardt DT, Noda M, O'Regan AW, Pavlin D, Berman JS. Osteopontin as a means to cope with environmental insults: regulation of inflammation, tissue remodeling, and cell survival. J Clin Inves 2001;107:1055-61.
86. O'Regan A, Berman JS. Osteopontin: a key cytokine in cell-mediated and granulomatous inflammation. Inter J Exper Pathol 2000;81:373-90.
87. Cho H-J, Cho H-J, Kim H-S. Osteopontin: a multifunctional protein at the crossroads of inflammation, atherosclerosis, and vascular calcification. Curr athero rep 2009;11:206-13.
88. Kühl U, Pauschinger M, Noutsias M, et al. High prevalence of viral genomes and multiple viral infections in the myocardium of adults with idiopathic left ventricular dysfunction. Circulation 2005;111:887-93.
89. Weber KT, Sun Y, Bhattacharya SK, Ahokas RA, Gerling IC. Myofibroblast-mediated mechanisms of pathological remodelling of the heart. Nat Rev Cardiol 2012;10:15-26.
90. Querejeta R, Lopez B, Gonzalez A, et al. Increased collagen type I synthesis in patients with heart failure of hypertensive origin - Relation to myocardial fibrosis. Circulation 2004;110:1263-68.

91. Swynghedauw B. Molecular mechanisms of myocardial remodeling. Physiolo rev 1999;79:215-62.
92. Manabe I, Shindo T, Nagai R. Gene expression in fibroblasts and fibrosis involvement in cardiac hypertrophy. Circ res 2002;91:1103-13.
93. Soufen HN, Salemi VM, Aneas IM, et al. Collagen content, but not the ratios of collagen type III/I mRNAs, differs among hypertensive, alcoholic, and idiopathic dilated cardiomyopathy. Braz J Med Biol Res 2008;41:1098-04.
94. Thomas DP, Zimmerman SD, Hansen TR, Martin DT, McCormick RJ. Collagen gene expression in rat left ventricle: interactive effect of age and exercise training. J of App Physiol 2000;89:1462-68.
95. Boluyt MO, Bing OH. Matrix gene expression and decompensated heart failure The aged SHR model. Cardiovas res 2000;46:239-49.
96. Lorell BH, Carabello BA. Left ventricular hypertrophy pathogenesis, detection, and prognosis. Circulation 2000;102:470-79.
97. Watsky MA, Weber KT, Sun Y, Postlethwaite A. New insights into the mechanism of fibroblast to myofibroblast transformation and associated pathologies. Int Rev Cell Mol Biol 2010;282:165-92.
98. Rooney W. MRI: From picture to proton. Health Phys 2003;85:504-05.
99. Collins D, Evans A, Holmes C, Peters T. Automatic 3D segmentation of neuro-anatomical structures from MRI. Med imag 1995;67:139-52.
100. Edelman RR, Hesselink JR, Zlatkin MB. Clinical magnetic resonance imaging. WB Saunders.ed., Philadelphia university press, Philadelphia 1996 :pp 123-35.
101. Seeldrayers PA, Syha J, Morrissey SP, et al. Magnetic resonance imaging investigation of blood-brain barrier damage in adoptive transfer experimental autoimmune encephalomyelitis. J neuroimmunol 1993;46:199-06.
102. Bulte JW, Kraitchman DL. Iron oxide MR contrast agents for molecular and cellular imaging. NMR Biomed 2004;17:484-99.
103. Pouliquen D, Le Jeune J, Perdrisot R, Ermias A, Jallet P. Iron oxide nanoparticles for use as an MRI contrast agent: pharmacokinetics and metabolism. Mag res imag 1991;9:275-83.
104. Landry R, Jacobs PM, Davis R, Shenouda M, Bolton WK. Pharmacokinetic study of ferumoxytol: a new iron replacement therapy in normal subjects and hemodialysis patients. Am J Nephrol 2005;25:400-10.
105. Snyder SR, Heinen U. Characterization of Magnetic Nanoparticles for Therapy and Diagnostics. Bruker BioSpin Application note. Voigt Rt, ed., Ettlingen 2006; pp-16-36
106. McCullough, Brendan J., et al. "Ferumoxytol in clinical practice: implications for MRI. J Mag Res Imag 2013:37;1476-79.
107. Wang Y-XJ. Superparamagnetic iron oxide based MRI contrast agents: current status of clinical application. Quant imag med sur 2011;1:35-39.
108. Shapiro EM, Skrtic S, Koretsky AP. Sizing it up: Cellular MRI using micron-sized iron oxide particles. Mag Res Med 2005;53:329-38.
109. Thorek DL, Tsourkas A. Size, charge and concentration dependent uptake of iron oxide particles by non-phagocytic cells. Biomaterials 2008;29:3583-90.
110. Van der Vaart M, Meerwaldt R, Slart R, van Dam G, Tio R, Zeebregts C. Application of PET/SPECT imaging in vascular disease. Eur J Vas Endovasc Sur 2008;35:507-13.
111. Thakur M. Radiolabelled peptides: now and the future. Nuc med comm 1995;16:724-32.
112. Forrer F, Valkema R, Kwekkeboom DJ, de Jong M, Krenning EP. Peptide receptor radionuclide therapy. Res Clin Endocrinol Metabol 2007;21:111-29.
113. Boerman OC, Rennen H, Oyen WJ, Corstens FH. Radiopharmaceuticals to image infection and inflammation. Nuc med 2001;59:286-95.
114. Rennen HJ, Boerman OC, Oyen WJ, Corstens FH. Imaging infection/inflammation in the new millennium. Eur J Nuc Med 2001;28:241-52.

115. Michalska M, Machtoub L, Manthey HD, et al. Visualization of Vascular Inflammation in the Atherosclerotic Mouse by Ultrasmall Superparamagnetic Iron Oxide Vascular Cell Adhesion Molecule-1–Specific Nanoparticles. Arterio Thromb Vas Biolo 2012;32:2350-57.
116. Palestro CJ. The current role of gallium imaging in infection. Nuc med 1994;58:128-41.
117. Ebright JR, Soin JS, Manoli RS. The Gallium Scan - Problems and Misuse in Examination of Patients with Suspected Infection. Ar Inter Med 1982;142:246-54.
118. Bekerman C, Hoffer P, Bitran J. The role of gallium-67 in the clinical evaluation of cancer. Nuc med 1985;29:72-03.
119. Lavender J, Lowe J, Barker J, Burn J, Chaudhri M. Gallium 67 citrate scanning in neoplastic and inflammatory lesions. Brit J Radiol 1971;44:361-66.
120. Ando A, Nitta K, Ando I, et al. Mechanism of gallium 67 accumulation in inflammatory tissue. Eur J Nuc Med 1990;17:21-27.
121. Ross TL, Ametamey ST. PET imaging: Radiopharmaceuticals. Basic Sciences of Nuclear Medicine, Khalil MM, ed., Springer 2011; pp 69-82.
122. Zaret BL, Rigo P, Wackers FJT, et al. Myocardial Perfusion Imaging with Tc-99m Tetrofosmin - Comparison to (Tl)-T-201 Imaging and Coronary Angiography in a Phase-Iii Multicenter. Circulation 1995;91:313-19.
123. Wackers FJT, Zaret BL. Radionuclide Stress Myocardial Perfusion Imaging - the Future Gatekeeper for Coronary Angiography. J Nuc Cardiol 1995;2:358-59.
124. Breeman WA, de Blois E, Sze Chan H, Konijnenberg M, Kwekkeboom DJ, Krenning EP. ^{68}Ga-labeled DOTA-Peptides and ^{68} Ga-labeled Radiopharmaceuticals for Positron Emission Tomography: Current Status of Research, Clinical Applications, and Future Perspectives. Sem in nuc med 2011:314-21.
125. Maecke HR, Reubi JC. Somatostatin receptors as targets for nuclear medicine imaging and radionuclide treatment. J Nuc Med 2011;52:841-44.
126. Bell GI, Reisine T. Molecular biology of somatostatin receptors. Trends neuro1993;16:34-38.
127. Metwali, Ahmed, et al. "Cutting edge: hemokinin has substance P-like function and expression in inflammation." J Immuno 2004;172: 6528-32..
128. Dalm VA, Van Hagen PM, van Koetsveld PM, et al. Expression of somatostatin, cortistatin, and somatostatin receptors in human monocytes, macrophages, and dendritic cells. Am J Physio-Endocrinol Metabol 2003;285:344-53.
129. Rominger A, Saam T, Vogl E, et al. In vivo imaging of macrophage activity in the coronary arteries using 68Ga-DOTATATE PET/CT: correlation with coronary calcium burden and risk factors. J Nuc Med 2010;51:193-97.
130. Higuchi T, Bengel FM, Seidl S, et al. Assessment of alpha(v)beta(3) integrin expression after myocardial infarction by positron emission tomography. Cardiovas Res 2008;78:395-03.
131. Asano Y, Ihn H, Yamane K, Jinnin M, Tamaki K. Increased expression of integrin alphavbeta5 induces the myofibroblastic differentiation of dermal fibroblasts. Am J Pathol 2006;168:499-10.
132. Liu Z, Niu G, Wang F, Chen X. (68)Ga-labeled NOTA-RGD-BBN peptide for dual integrin and GRPR-targeted tumor imaging. Eur J Nucl Med Mol Imaging 2009;36:1483-94.
133. Koch FP, Wunsch A, Merkel C, et al. The influence of bisphosphonates on human osteoblast migration and integrin aVb3/tenascin C gene expression in vitro. Nat Med 2011;7:46-54
134. Ley K, Laudanna C, Cybulsky MI, Nourshargh S. Getting to the site of inflammation: the leukocyte adhesion cascade updated. Nat Rev Immunol 2007;7:678-89.
135. Haubner R, Weber WA, Beer AJ, et al. Noninvasive visualization of the activated αvβ3 integrin in cancer patients by positron emission tomography and [18F] Galacto-RGD. PLoS medicine 2005;2:70-75.
136. Winter PM, Morawski AM, Caruthers SD, et al. Molecular imaging of angiogenesis in early-stage atherosclerosis with αvβ3-integrin–targeted nanoparticles. Circulation 2003;108:2270-74.

137. Jahns R, Borgese F, Lindenthal S, Straub A, Motais R, Fievet B. Trout red blood cell arrestin (TRCarr), a novel member of the arrestin family: cloning, immunoprecipitation and expression of recombinant TRCarr. Biochem. J. 1996;316:497-06.
138. Boivin V, Beyersdorf N, Palm D, et al. Novel Receptor-Derived Cyclopeptides to Treat Heart Failure Caused by Anti-β1-Adrenoceptor Antibodies in a Human-Analogous Rat Model. PLoS ONE 2015;10:e0117589.
139. Litwin SE, Katz SE, Weinberg EO, Lorell BH, Aurigemma GP, Douglas PS. Serial echocardiographic Doppler assessment of left ventricular geometry and function in rats with pressure-overload hypertrophy. Circulation 1995;91:2642-54.
140. Winter P, Kampf T, Helluy X, et al. Fast retrospectively triggered local pulse-wave velocity measurements in mice with CMR-microscopy using a radial trajectory. J Cardiovasc Magn Reson 2013;15:88-98.
141. Mackay IR, Rose NR. The Autoimmune Diseases II: Elsevier, 2012.
142. Mahrholdt H, Goedecke C, Wagner A, al. e. Cardiovascular magnetic resonance assessment of human myocarditis: a comparison to histology and molecular pathology. Circulation 2004;109:1250-58.
143. Caforio AL, Mahon NJ, Tona F, McKenna WJ. Circulating cardiac autoantibodies in dilated cardiomyopathy and myocarditis: pathogenetic and clinical significance. Eur J Heart Fail 2002;4:411-7.
144. Bader M. Rat models of cardiovascular diseases. Rat Genomics: Springer, 2010:403-414.
145. Izumi T, Kohno K, Inomata T, Takagaki Y. Myocarditogenic epitopes and autoimmune myocarditis. Intern Med 2003;42:3-6.
146. Kodama M, Matsumoto Y, Fujiwara M, Masani F, Izumi T, Shibata A. A novel experimental model of giant cell myocarditis induced in rats by immunization with cardiac myosin fraction. Clin immunol immunopathol 1990;57:250-62.
147. Litovsky SH, Burke AP, Virmani R. Giant cell myocarditis: an entity distinct from sarcoidosis characterized by multiphasic myocyte destruction by cytotoxic T cells and histiocytic giant cells. Diag Patho 1996;9:1126.
148. Afanasyeva M, Georgakopoulos D, Rose NR. Autoimmune myocarditis: cellular mediators of cardiac dysfunction. Autoimmun rev 2004;3:476-86.
149. Medzhitov R. Origin and physiological roles of inflammation. Nature 2008;454:428-35.
150. Nicoletti A, Michel J-B. Cardiac fibrosis and inflammation interaction with hemodynamic and hormonal factors. Cardiovas res 1999;41:532-43.
151. Saji T, Matsuura H, Hasegawa K, et al. Comparison of the clinical presentation, treatment, and outcome of fulminant and acute myocarditis in children. Circ J 2012;76:1222-28.
152. Basso C, Calabrese F, Angelini A, Carturan E, Thiene G. Classification and histological, immunohistochemical, and molecular diagnosis of inflammatory myocardial disease. Heart fail rev 2013;18:673-81.
153. Himmelreich U, Dresselaers T. Cell labeling and tracking for experimental models using Magnetic Resonance Imaging. Nat Met 2009;48:112-24.
154. Wu YL, Ye Q, Foley LM, et al. In situ labeling of immune cells with iron oxide particles: An approach to detect organ rejection by cellular MRI. Pro Nat Acad Sci 2006;103:1852-57.
155. Ye Q, Wu YL, Foley LM, et al. Longitudinal tracking of recipient macrophages in a rat chronic cardiac allograft rejection model with noninvasive magnetic resonance imaging using micrometer-sized paramagnetic iron oxide particles. Circulation 2008;118:149-56.
156. Bonnemain B. Superparamagnetic agents in magnetic resonance imaging: physicochemical characteristics and clinical applications a review. J drug target 1998;6:167-74.
157. Perl DP, Good PF. Comparative techniques for determining cellular iron distribution in brain tissues. Annals neurol 1992;32:76-81.
158. Yilmaz A, Dengler MA, van der Kuip H, et al. Imaging of myocardial infarction using ultrasmall superparamagnetic iron oxide nanoparticles: a human study using a multi-parametric cardiovascular magnetic resonance imaging approach. Eur heart J 2013;34:462-75.

159. Yilmaz A, Rösch S, Yildiz H, Klumpp S, Sechtem U. First Multiparametric Cardiovascular Magnetic Resonance Study Using Ultrasmall Superparamagnetic Iron Oxide Nanoparticles in a Patient With Acute Myocardial Infarction New Vistas for the Clinical Application of Ultrasmall Superparamagnetic Iron Oxide. Circulation 2012;126:1932-34.
160. Apblett AW, Kuriyavar SI, Kiran B. Preparation of micron-sized spherical porous iron oxide particles. J of Mat Chem 2003;13:983-85.
161. McAteer MA, Sibson NR, von zur Muhlen C, et al. In vivo magnetic resonance imaging of acute brain inflammation using microparticles of iron oxide. Nat Med 2007;13:1253-58.
162. Hsiao J-K, Tai M-F, Yang C-Y, et al. Comparison of micrometer and nanometer sized magnetic particles for cell labeling. Mag Res Imag 2007;43:2421-23.
163. O'Connell JB, Henkin RE, Robinson JA, Subramanian R, Scanlon P, Gunnar R. Gallium-67 imaging in patients with dilated cardiomyopathy and biopsy-proven myocarditis. Circulation 1984;70:58-62.
164. Matsuura H, Ishikita T, Yamamoto S, et al. Gallium-67 myocardial imaging for the detection of myocarditis in the acute phase of Kawasaki disease (mucocutaneous lymph node syndrome): the usefulness of single photon emission computed tomography. Brit heart J 1987;58:385-92.
165. Kayani I, Bomanji JB, Groves A, et al. Functional imaging of neuroendocrine tumors with combined PET/CT using 68Ga-DOTATATE (DOTA-DPhe1, Tyr3-octreotate) and 18F-FDG. Cancer 2008;112:2447-55.
166. Li X, Bauer W, Kreissl MC, et al. Specific somatostatin receptor II expression in arterial plaque: 68Ga-DOTATATE autoradiographic, immunohistochemical and flow cytometric studies in apoE-deficient mice. Atherosclerosis 2013;85:68-79.
167. Li X, Samnick S, Lapa C, et al. 68Ga-DOTATATE PET/CT for the detection of inflammation of large arteries: correlation with18F-FDG, calcium burden and risk factors. EJNMMI research 2012;2:1-10.